Growth Engineering and Characterization of Vanadium Dioxide Films for Ultraviolet Detection

Jason Andrew Creeden

Warrenton, Virginia

Master of Science, College of William & Mary, 2017
Bachelor of Science, Eastern Kentucky University, 2015

A Dissertation presented to the Graduate Faculty
of The College of William & Mary in Candidacy for the Degree of
Doctor of Philosophy

Department of Physics

College of William & Mary
January 2020

APPROVAL PAGE

This Dissertation is submitted in partial fulfillment of
the requirements for the degree of

Doctor of Philosophy

Jason Andrew Creeden

Approved by the Committee October 2019

Co-Chair
DARPA Program Manager/Professor Emerita Rosa Alejandra Lukaszew, Physics
DARPA/College of William & Mary

Co-Chair
Professor Irina Novikova, Physics
College of William & Mary

CSX Professor, Vice Provost for Research and Graduate/Professional Studies, William & Mary
Director for the Applied Research Center Dennis Manos, Physics
College of William & Mary

Associate Professor Mumtaz Qazilbash, Physics
College of William & Mary

Dr. Russell A. Wincheski, Aerospace Technologist (AST)
NASA Langley Research Center

ABSTRACT

There is a need for efficient ultraviolet (UV) detectors in many fields, such as aerospace, automotive manufacturing, biology, environmental science, and defense, due to photomultiplier tubes (the currently available technology) often not meeting application constraints in weight, robustness, and power consumption. In my thesis, I demonstrate that high quality vanadium dioxide (VO_2) thin films, epitaxially grown on niobium doped titanium dioxide substrates (TiO_2:Nb), display a strong photoconductive response in the UV spectral range, making them promising candidates for photomultiplier-free UV photodetection. By adjusting the characteristics of the substrate and VO_2 film, the samples achieve external quantum efficiency exceeding 100% (reaching beyond 1,000% for optimized samples) superior to that of current wide band gap UV detectors at room temperature. The mechanism for photocurrent production in VO_2/TiO_2:Nb heterostructure is a space-charge region, engineered in the heterojunction, yielding favorable conditions for hole tunneling from TiO_2:Nb into VO_2. Improving upon the heterostructure, I demonstrate up to an order of magnitude improvement in parameters such as responsivity, external quantum efficiency, detectivity, and dark current density by applying Au films to the VO_2/TiO_2:Nb heterostructure. Ultimately, my work proved that the VO_2/TiO_2:Nb heterostructure is a promising alternative technology for UV detection in high demand fields, with great potential for scalable device production.

TABLE OF CONTENTS

ACKNOWLEDGEMENTS

I would like to begin by thanking my advisors Ale Lukaszew and Irina Novikova, without your guidance, support, and mentorship this project wouldn't have been possible. I would also like to thank the past and present members of the research group - Doug Beringer, Melissa Beebe, Matt Burton, Savannah Cuozzo, Zhaozhu Li, Scott Madaras, Nikunjkumar Prajapati, and Kaida Yang. I would like to extend a great thank you to my friends and fellow graduate students through this process. The many long, arduous days have been enjoyable over the past few years because of you. I would like to express my gratitude to all the excellent professors that have helped get me this far. In particular, I would like to express a deep thanks to my undergraduate advisor Jessica Lair. Finally, I would like to thank my family, your love and constant support over the course of this project has been nothing short of incredible and I am humbled and grateful for it. I would like to particularly thank Emily Rolen, without your steadfast and unwavering support this would have been impossible.

This research was made possible by financial support from the Defense Threat Reduction Agency (DTRA) (HDTRA 1-16-1-0056).

For my Mother, Father, Sisters, and Emily

LIST OF TABLES

LIST OF FIGURES

CHAPTER 1

Motivation to Develop the Next Generation of UV Detectors

Ultraviolet detectors are a necessary instrument for several in demand fields such as aerospace, automotive manufacturing, biology, environmental science, and defense with applications ranging from astronomy to radioactive material detection. These detectors require highly efficient and sensitive broadband UV detection while ideally operating under low voltage bias at convenient temperatures. Here, I present an introduction to the application of UV detectors for the purpose of neutron detection with radioactive sources. I begin with an overview of Helium-3 neutron detectors and proceed to discuss how the shortage of He-3 has necessitated the development of alternative technologies. Finally, I conclude with how the vanadium dioxide detector developed in this study serves to address many of the needs for current UV and neutron detection.

1.1. Helium-3 Detector

Helium-3 neutron detectors are the primary radiation detectors at more than 1400 domestic portals.[1] There are over 2000 additional US-deployed radiation detectors overseas. [1] Helium-3 neutron detectors require a neutron collision with a helium 3 nucleus resulting in the formation of a proton, tritium, and 764keV of energy, shown in Figure 1.1. The energy from this collision ionizes a surrounding gas (normally carbon tetrafluoride (CF_4)) liberating electrons which are attracted to an anode wire. The resulting interaction between the free electrons and the anode wire produces event counts proportional to the number of neutrons.

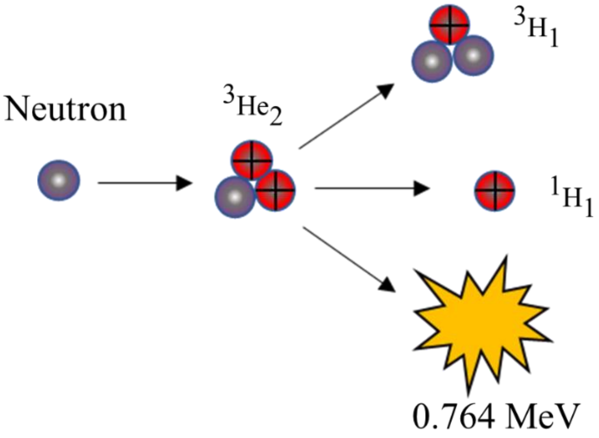

Figure 1.1: Neutron and Helium-3 collision used for neutron detection.

In 2011, the Department of Energy reported weaknesses in the management of helium-3, restricting its usage to applications with no alternatives. [1] In response to this shortage, multiple detection technologies were created to replace helium-3 neutron detectors. The alternative detectors primarily use plastic or organic scintillators emitting in ultraviolet wavelength ranging between 450nm-300nm.

1.2. Alternative Detector Landscape

The photomultiplier tube is the widest available alternative to the helium-3 detector. It uses a combination of scintillation material, photocathode, and photomultiplication device to detect neutron events. A photomultiplication device, shown in Figure 1.2, is needed to adequately detect the low counts of UV photons produced from the scintillated neutrons. These photomultiplication devices are efficient in increasing the detection sensitivity, however, photomultipliers come with a number of drawbacks. These drawbacks are primarily attributed to two key components: (i) the dynodes (electrodes that serve as electron multipliers through secondary electron emission) and (ii) the high voltage power supply. The (i) dynodes require a vacuum to operate, so the entire device is encased in a glass vacuum tube which adds fragility and bulk to the system. Additionally, the (ii) high voltage power supply requires a current source and further increases the size of the system. These components create serious problems for detection applications where robust, lightweight, high sensitivity detectors are necessary.

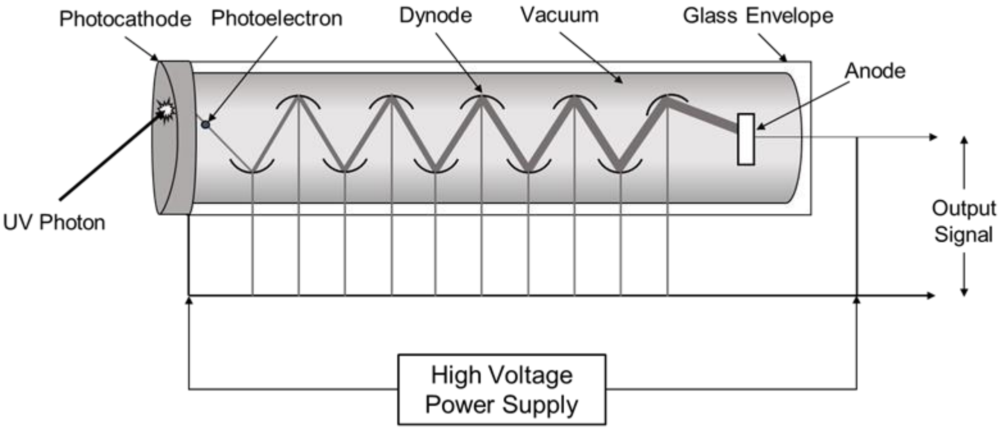

Figure 1.2: Photomultiplier tube example diagram.

Due to these application constraints, there is a need for high sensitivity photomultiplier-free UV detectors in aerospace, automotive manufacturing, biology, environmental science, and military applications. The lack of broadband UV detecting materials compounds this need, given current solutions are expensive and difficult to produce. Thus, this problem requires a cost-effective, easy to produce material capable of maintaining high detection efficiencies and sensitivities for UV photons emitted by scintillated neutrons in the broadband UV (2.75 eV (450nm) - 4.13 eV (300nm)) range.

The current standard photomultiplier-free UV detectors are silicon-based. However, current silicon detectors are not capable of meeting the required efficiency and sensitivity demands.[2–6] One could alternatively use wide band gap semiconductors such as AlGaN[4,7–9], β-Ga_2O_3[10,11], GaN[7,12], TiO_2[13],

Zn_2GeO_4[14], ZnMgO[15], and ZnO[16,17] due to their high responsivity, room temperature operation, and fast response speed.[3,6,18] However, these materials tend to have other properties that are detrimental for practical commercial implementations such as narrow detection bandwidths [7–10,12,14], voltage bias requirements [3,7,19,8,10,12–17], and/or complicated fabrication methods hindering production scalability[4,10,11,16].

Here, I report the development of a highly efficient and sensitive UV detector using a vanadium dioxide (VO_2) thin film on niobium doped titanium dioxide (TiO_2:Nb) substrate heterostructure in the scheme shown in Figure 1.3. This detector detects UV light generated from scintillated neutrons by producing a photocurrent in the VO_2/TiO_2:Nb heterostructure. The VO_2/TiO_2:Nb detector is connected to a sensing amp allowing us to monitor the neutrons present via the photocurrent. To create this detector, I have developed the procedures for growth and characterization of VO_2 on TiO_2 and TiO_2:Nb substrate heterostructures. I demonstrated that VO_2 on TiO_2:Nb is a high efficiency broadband UV detector under zero voltage bias at convenient operation temperatures.[20,21] Additionally, with the benefit of magnetron sputtering deposition, the VO_2 films are a cost efficient, scalable production technique suitable for practical device development.

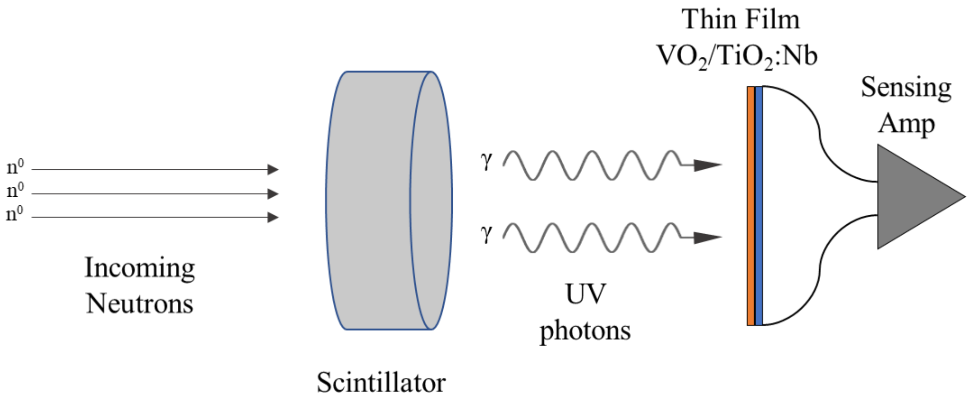

Figure 1.3: Vanadium dioxide neutron detector concept.

1.3. Scope of Dissertation

In this thesis, I will focus on the growth and characterization of VO_2 thin films on various substrates, with the overall goal of developing a photomultiplier free UV photodetector, as discussed above. I begin by discussing thin film growth and maturation in Chapter 2, stressing the importance of processes that occur at the growth surface during a film's development. I proceed to introduce strongly correlated materials in Chapter 3, beginning with metals and semiconductors eventually describing how both material properties manifest in strongly correlated materials such as VO_2. Building upon the previous discussions of thin film growth and strongly correlated materials, I examine how the properties of VO_2 and TiO_2 can detect UV light when grown together. In Chapter 5, I introduce the methods used to grow and characterize properties of all samples in the project.

With Chapters 6-9, I demonstrate the results of this project describing how VO_2 films are a novel and promising approach to photomultiplier-free UV detection. In Chapter 6, I analyze the crystal structure of high quality epitaxial VO_2 films on c-Al_2O_3 and TiO_2 using Reflection High Energy Electron Diffraction (RHEED). In Chapter 7, I examine the evolution of the epitaxial growth for VO_2 thin films on TiO_2(002) substrates by evaluating the dynamic scaling relationships at several film thicknesses. Chapter 8 is a study of the VO_2 on TiO_2:Nb heterostructure evaluating the figures of merit for the samples when exposed to either NUV (405 nm) or UV-C (254 nm) light. Finally, in Chapter 9, I present enhancements to the detective characteristics of the VO_2/TiO_2:Nb heterostructure by applying Au contacts. These results culminate in the VO_2 on TiO_2:Nb heterostructure being a promising approach for highly efficient and sensitive UV detection, particularly, in neutron detection schemes.

CHAPTER 2

Thin Films and Surfaces

This chapter focuses on the behavior of thin film and substrate surfaces. Due to the critical importance of thin film growth on the properties of VO_2 films, it is necessary to discuss how surfaces affect the growth of a film. I begin with an atomistic view of the substrate/film interface and the associated surface-born effects. I proceed to examine the formation of a film during nucleation, growth, and coalescence to understand the dynamic at play in the development of VO_2 films.

2.1 Free Surfaces

The properties of thin films are dominated by the underlying material's (substrate's) surface properties. The substrate surface provides the initial template for the deposition and growth of a film. Thus, an understanding of how the underlying structure affects the growth mechanisms and film properties is critical to a well-tailored, high quality thin film.[22,23]

The substrate surface serves as a vehicle for imparting the structural, mechanical, and physical interfacial properties of the film distinct from bulk materials. [22,23] To visualize this, one can examine the neighboring species in the bulk of a material, where each neighbor compensates for its surrounding neighbor's charge. At a surface however, there is a lack of neighbors to properly compensate for the charge, resulting in a charge imbalance. This results in a nonzero surface electrical potential as well as significant changes to surface crystallography and electronic structure, compared to the interior bulk material, which can be used to alter technologically relevant properties of two materials at the interface, such as VO_2 on TiO_2:Nb.[23]

The substrate surface, as a growth front, imparts effects on a film's growth; two important examples being the surface morphology and surface chemistry.[22,23] Surface morphology determines geometrical shadowing of the surface from an influx of adatoms (mobile atoms adsorbed to a surface) resulting in changes to the porosity and overall development of a film.[22] The surface chemistry affects the adatom surface reaction and nucleation density, determining the stability of the interface formed between substrate and film.[22] One can see in just these two properties that surface characteristics of the growth front are critical determiners of the resulting film and as such must be accommodated for during the growth process.

2.2 Thin Film Growth

It is necessary to begin by defining the term "thin film". A working definition could be: a very thin layer of a substance on a supporting material, where "very thin" is less than 5 μm. This definition works for many typical applications, as many supporting materials have lateral lengths greater than a millimeter. However, "very thin" becomes an issue if the supporting material's lateral length scales are more constrained, such as in the case with silicon transistors. A more accurate definition would be a film is thin when its thickness is significantly constrained in relation to an intrinsically relevant length scale of the system (i.e. $d_z \ll d_{x,y}$) and the properties of the initial film layers are dominated by the underlying material's surface properties (i.e. energetic structure).[22–24] This definition of the constrained nature of thin films gives us a basis to discuss the development of a thin film.

A thin film grows in three stages: (i) adsorption, (ii) nucleation, and (iii) coalescence. The basic outline of thin film growth begins with exposing the substrate surface to impinging atoms in a vacuum environment. These atoms interact with the substrate surface by either reflecting off immediately, re-evaporating after adsorbing (sticking), or adsorbing and remaining on the substrate.[22,23] Adsorption occurs in two types determined by the strength of interaction with the surfaces: *chemisorption* (low adatom mobility) where the particle changes its identity by bonding with the substrate through either ionic or covalent bonds or *physisorption* (high adatom mobility) where the particle is stretched or bent but retains its original identity by being held to the surface by van de Waals forces. In either case, these particles will have mobility on the surface and seek to lose energy by: bonding with the surface or each other, finding preferential nucleation sites, or colliding with other diffusing surface atoms or adsorbed surface species. This rate of atoms sticking to the surface versus the total number of impinging atoms called the sticking parameter.

Once the adatoms bond to the surface, the nucleation process begins. As mentioned previously, each adatom will seek to bond to the target through adsorption. These adsorption locations are called nucleation sites.[22,23] The site location varies depending on the interaction strength between the surface and the adatom. In the strongest interactions (chemisorption), the adatoms themselves can act as nucleation sites, while in weaker interactions (physisorption), morphological discontinuities, separate chemistries, defects, etc. serve as nucleation sites.[22,23] Additionally, the interaction strength between substrate and adatom determines which of three initial methods, shown in Figure 2.1, the thin film growth will follow: (i) van der Merwe mechanism for layer by layer growth, (ii) Volmer Weber mechanism for three-dimensional nucleation or island growth, (iii) Stranski-

Krastanov (S-K) growth for a strained layer growth, followed by cluster migration called layer plus island growth.[23] As the number of stable nuclei increases, the individual nuclei from these growth methods begin to coalesce.

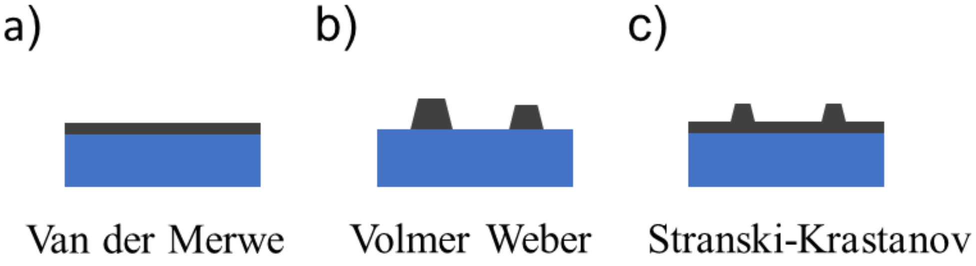

Figure 2.1: The three growth methods for film growth a) van der Merwe mechanism for layer by layer growth b) Volmer Weber mechanism for three-dimensional nucleation or island growth c) Stranski-Krastanov (S-K) growth for layer plus island growth.

Ostwald ripening occurs when larger adatom islands begin to grow or “ripen” via mass transport at the expense of the smaller islands, minimizing the surface chemical potential of the island structures.[23] Note, this mechanism does not require the islands to touch the for mass transfer to take place. Immediately after the Ostwald ripening process, coalescence begins with a combination of two mechanisms: (i) sintering and (ii) cluster migration.[23] In (i) sintering, two adjacent islands form a neck between them. This neck thickens from material in both islands combining to form a single island. The second mechanism (ii) cluster migration, occurs when mobile islands on the surface coalesce into one due to collisions between the islands. The ultimate result is the formation of larger islands formed from separate isolated, smaller island leading to a single coalescent film on the surface.

Due to the processes above, film growth occurs in a layer-by-layer nature resulting in the initial layers of the film experiencing strong energetic effects from the underlying substrate surface. These initial layers (epilayers) will either adjust to the underlying crystal structure or dislocate from it. If the film accommodates for the substrate this results in an epitaxial film.[23] Epitaxy is broken into two categories: homoepitaxy and heteroepitaxy. Homoepitaxy occurs when the substrate and the film are the same material, (i.e. the lattices parameters match exactly). Alternatively, heteroepitaxy occurs when there is a mismatch between film and substrate (i.e. the substrate and film lattice parameters differ). A mismatch will leads to lattice adjustments from the introduced strain on the epilayers. The growth of strained epilayers, called pseudomorphic growth, is only possible if the lattice mismatch is less than 9%. [23] Pseudomorphic growth, for a small lattice mismatch, results in the later epilayers of the film matching the initial layers resulting in a lattice structure similar to the substrate. However, with more substantial lattice parameter differences, the later epilayers of the film cannot accommodate for the large degree of strain in the initial epilayers, therefore, the film will relax or adjust back to its original unstrained lattice parameter after some critical thickness this return from the strained lattice to original bulk like lattice creates a relaxed structure. These processes are shown in Fig. 2.2.

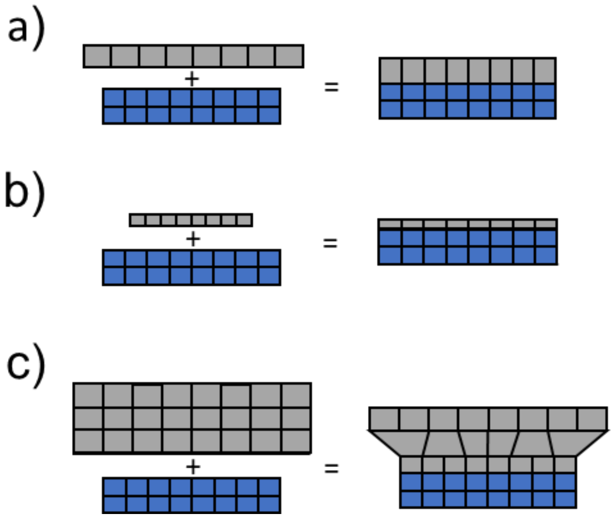

Figure 2.2: The three types strain in heteroepitaxy: a) compressive, b) tensile, and c) relaxed compressive.

Any adjustments to a film's lattice parameter and structure can cause the properties of a film to deviate significantly from the bulk properties. These changes can include the electronic, optical, thermal, and mechanical properties. Thus, understanding the epitaxy and strain of a film is one of the most important aspects to thin film growth. The deposition parameters strongly affect the overall film development and growth properties such as the sticking parameter, adatom movement, and epitaxy as shown by the structure zone diagram (SZD) in Fig 2.3. The SZD gives a good overall view of the film growth and resulting changes with growth environment.[22–24]

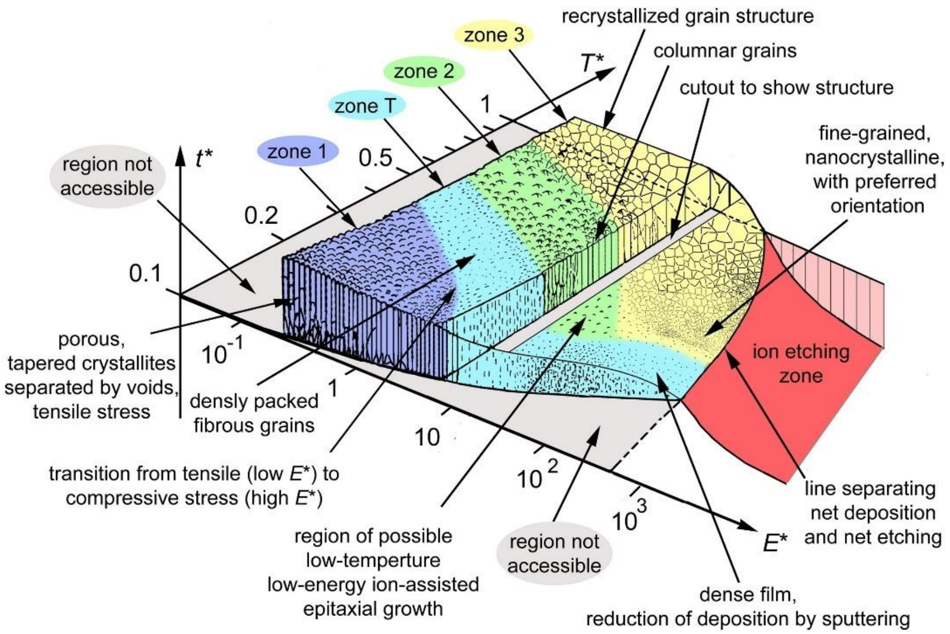

Figure 2.3: Structure zone diagram illustrating how thin-film structure varies with film thickness t, growth temperature T^*, and deposition energy E^*. (reproduced from [25] with permission from the author and Elsevier Publishers).

CHAPTER 3

Introduction to Strongly Correlated Materials

Vanadium dioxide is one of the most extensively studied materials in the strongly correlated electron family, where it is known to undergo a reversible first order transition from insulator/semiconductor to metal. To motivate the novel properties of strongly correlated materials, it is best to begin our discussion with the characterization of metals and semiconductors, as these materials make up the two phases of the VO_2 transition, before examining the behavior of strongly correlated materials.

3.1. Early Models of Metals

In 1897, J.J. Thompson discovered the electron, which revolutionized the study of matter, giving an obvious mechanism for introducing conduction in metals. Following this discovery, P. Drude, in 1900, developed the first viable theory on electrical and thermal conduction in metals. This model considered the metal as an electron gas with a compensating positive charge attached to much heavier metallic ions. In this model, the electron gas would follow the kinetic theory of gasses where the electrons are free to wander through the metal.[26] The kinetic theory of gasses for a metal makes four key assumptions: 1) aside from collisions, electrons have no long range interactions with other electrons or ions 2) collisions are instantaneous and abruptly alter the electron velocity, and ions are considered impenetrable thus scattering does not occur 3) electrons experience a collision at probability of $1/\tau$ where τ is the mean free time between collisions 4) electrons only achieve thermal equilibrium with the surrounding environment through collisions.[26] The Drude model of metals can achieve adequate approximations for some metallic properties, however, it falls short for several thermodynamic properties, particularly temperature gradients via the Seebeck effect and thermal conductivity, leading investigators to develop a more adequate theory to explain the behavior of metals. Noting that more sophisticated quantum mechanical and semi-classical treatments of electron transport in metals for AC and DC electric fields yield the Drude conductivity formula. The Drude conductivity formula continues to be useful for describing electron transport in metals in AC and DC electric fields.

The next major step in modelling metals occurred following the advent of quantum theory, recognizing that the Pauli exclusion principle applies for electrons. Therefore the electron velocity distribution is the Fermi Dirac distribution, instead of the Maxwell Boltzmann distribution, as in Drude's model of metals.[26] In 1927, A. Sommerfeld substituted the Fermi Dirac distribution for the Maxwell Boltzmann distribution, reconciling most of the major anomalies in Drude's model. This substitution affects only properties that require knowledge of the electronic velocity distributions resulting in adjustment to only the electron mean free path, thermal conductivity, and thermopower, bringing alignment with experimentation. Though the Sommerfeld model presented several improvements to the Drude model, there were still several properties that were unaccounted for, including temperature dependence in DC and AC conductivities, nonvanishing magnetoresistance, and temperature dependence in the Hall coefficient, all of which could not be rectified in Sommerfeld's model.

3.2. Bloch's Theory of Metals

Following the development of the Sommerfeld model, F. Bloch, in 1929, proposed a new approach to modelling electron interactions in a metal. This model begins with electrons interacting with a perfect crystal lattice of periodicity $\boldsymbol{R}$ such that for any position on the lattice $\boldsymbol{r}$ follows:

$$\boldsymbol{r} + \boldsymbol{R} = \boldsymbol{r} \tag{3.1}$$

and the metallic ions to have potential $U(\boldsymbol{r})$ such that the periodicity of the lattice potential becomes:

$$U(\boldsymbol{r}+\boldsymbol{R}) = U(\boldsymbol{r}) \tag{3.2}$$

Therefore, the electron interaction with any ion's potential is similar to the atomic potential if the electron and ion are close and falls off as the electron move further away.[26–28] Bloch modeled the behavior of this interaction with the single electron Schrodinger equation, resulting in the theorem: the eigenstates of the one electron Hamiltonian for the periodic crystal lattice have the periodicity of said lattice such that:

$$\psi_{n\boldsymbol{k}}(\boldsymbol{r}) = e^{i\boldsymbol{k}\cdot\boldsymbol{r}} u_{n\boldsymbol{k}}(\boldsymbol{r}) \tag{3.3}$$

and,

$$\psi_{n\boldsymbol{k}}(\boldsymbol{r}+\boldsymbol{R}) = e^{i\boldsymbol{k}\cdot\boldsymbol{R}} \psi_{n\boldsymbol{k}}(\boldsymbol{r}) \tag{3.4}$$

thus,

$$u_{n\boldsymbol{k}}(\boldsymbol{r}+\boldsymbol{R}) = u_{n\boldsymbol{k}}(\boldsymbol{r}) \tag{3.5}$$

where $\boldsymbol{k}$ is the wave vector of the electron and $\boldsymbol{n}$ is the band index of the discretely spaced eigenvalues. [26–28] The periodicity of this wave vector $\boldsymbol{k}$ for a given $\boldsymbol{n}$ results in a wavefunction, when inserted into the Schrodinger Equation, returns a family of continuous functions $\varepsilon_{n\boldsymbol{k}}$ called the band structure of a solid. The set of electronic levels described by $\varepsilon_{n\boldsymbol{k}}$ for a given $\boldsymbol{n}$ is called an energy band.

The Bloch approach to electrons in a periodic lattice accounts for most of the inconsistencies that persisted in the Sommerfeld model such as nonvanishing magnetoresistance as well as field and temperature dependence in the Hall coefficient. Additionally, this approach set the path to the solution for temperature dependence in DC and AC conductivities by introducing thermal lattice vibrations, however, this problem wouldn't be solved until later.

The most important discovery from the Bloch approach, related to metals, is the development of a band structure. Discovered by A. Wilson in 1931, the band structure allows electrons to "fill" or occupy the energy levels of a band where the last filled energy level and the first unfilled energy level is separated by a surface of constant energy, called a Fermi surface.[26,29] Electron band filling follows two key principles: (i) a certain number of bands may be completely filled and all other bands above the last occupied band remain empty (ii) the highest occupied band may either be partially or completely filled. The filling of the electronic bands, at last, defined a metal vs non-metal. In a metal, the highest occupied band is partially filled, and, in a non-metal, the highest occupied band is completely filled. This band filling also defines the location of the Fermi surface. In a metal, the Fermi surface is inside the partially filled band, and in a non-metal, the Fermi surface is between the highest filled band and the lowest unfilled band as described in Fig. 3.1.

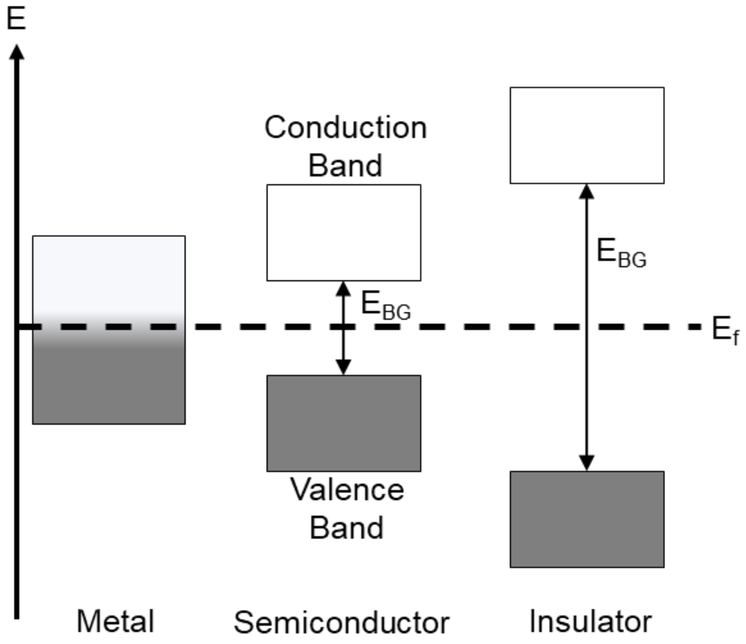

Figure 3.1: The band structure for a metal, semiconductor, and insulator. E_{BG} is the band gap energy and E_f is the Fermi level (Fermi surface).

The definition of a metal immediately allowed the definition of a second material type called insulators which possessed a large band gap and were far less conductive than metals. In metals, the partial filling of the metallic band makes metals excellent conductors because the filled and unfilled energy levels overlap inside the same band (i.e. partial filling). Thus, an electron can readily jump to an unfilled energy level allowing the electron to move freely. Conversely, insulators are non-conducting due to the prohibitively large energy separation (band gap) between the filled and unfilled energy levels preventing electrons from moving freely.

This nomenclature quickly proved to be insufficient, to describe all materials, as a separate class of materials displayed increased conductivity with temperature (exceeding that of some metals) making it distinct from both insulators and metals. This new material possessed a small band gap and large conductivity at high temperatures making it non-insulating, but the Fermi surface still falls inside the band gap making the material distinctly non-metallic. Thus, the differences in conductivity at separate temperatures led to these materials being named semiconductors.

3.3. Band Structure Approach to Semiconductors

The first document of any semiconducting behavior was presented in 1782, by A. Volta, discovering that certain materials discharge at a short but non-immediate rate. The next major discovery occurred in 1833, as M. Faraday observed that the resistivity of AgS_2 decreased rapidly with temperature, in opposition to the usual increase in resistivity with temperature in metals.[30] These discoveries remained unexplainable, until Wilson's introduction of a band structure found that a sufficiently small band gap allows electrons to be thermally excited from a filled band into an unfilled band.[29] These excitations result in partial filling of the previously unoccupied band leading to a rapid decrease in resistivity. This approach to semiconductors gave a mechanism for the observations of M. Faraday almost a century earlier.

The definition of a semiconductor then follows: a semiconductor is an insulator at T=0K, whose energy gap is of such a size that thermal excitations can lead to observable conductivity at temperatures below the melting point.[26,28] This thermal excitation is critically dependent on the size of the separation or "band gap" between the unoccupied upper band called the conduction band and the occupied lower band called the valence band, as shown in Fig. 3.1. Therefore, the semiconductor has a small enough band gap that a meaningful number of electrons can be excited from the conduction band to the valence band given a certain energy defined by the band gap. However, due to both insulating and semiconducting materials possessing a band gap, the designation between insulators and semiconductors is not as sharp as between metals and non-metals, with many important semiconductors having band gaps less than 2 eV though some semiconductors may have band gaps greater than 4 eV. [26,28] A rough estimation for the fraction of electrons excited across the band gap at a given temperature (T) is given by $e^{-E_g/2k_BT}$ where $\left(E_g\right)$ is the band gap energy and (k_B) is Boltzmann's constant and at room temperature $k_BT \approx 0.025\text{eV}$. Thus for a 2 eV band gap the fraction of electrons excited would be $\sim 10^{-18}$ and for the 4 eV band gap an electron fraction of $\sim 10^{-35}$. [26,28]

3.3.1. Semiconductors as Detectors

The small band gap in semiconductors permits several novel properties such as large thermopowers, rectifying effects, and photoconductivity. We will focus on photoconductivity for this study. Photoconductivity is the increase of conductivity by illuminating a material.[26] This increase in conductivity is due to the incident light possessing enough energy to excite carriers, in the valence band, across the band gap into the conduction band. This increases the density of free carriers (electrons) in the conduction band leading to a metallic partially filled band with increased conductivity. The carrier excitation can occur with two transitions, either directly or indirectly as shown in Fig. 3.2.

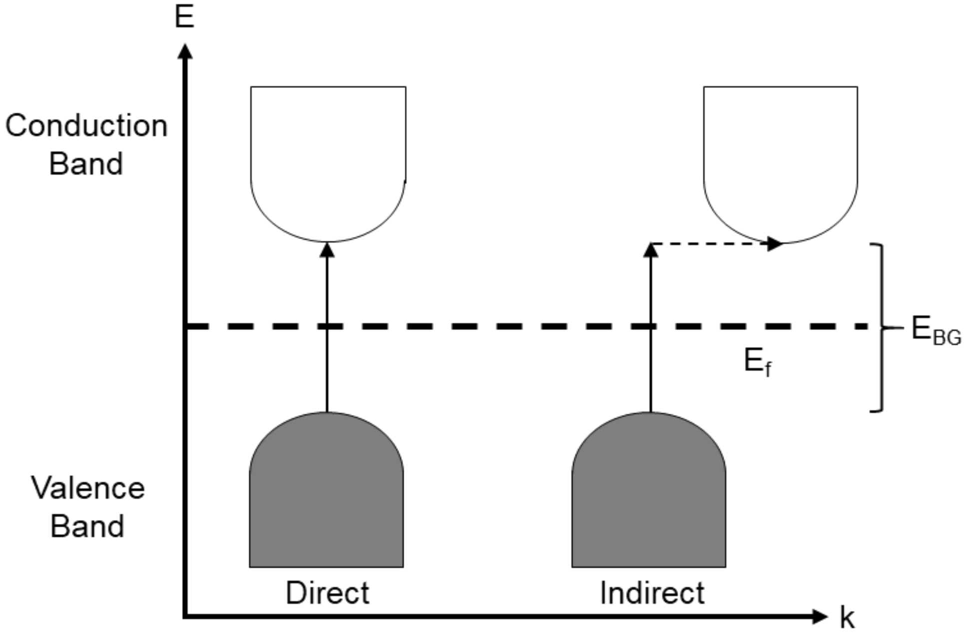

Figure 3.2: The direct and indirect band gap excitation. The solid line is the photon energy and the dotted line is the added phonon momentum. E_{BG} is the band gap energy and E_f is the Fermi level (Fermi surface).

The direct transition occurs when the incident photons energy is large enough to match or exceed the band gap energy resulting in carrier excitation across the band gap. Thus, the condition for excitation is:

$$E_{\gamma} \geq E_{BG} \tag{3.6}$$

where E_{γ} is the energy of the photon and E_{BG} is the band gap energy. For the indirect transition, the conduction and valence bands are separated in k-space (momentum-space) as shown in Fig 3.2. In this case, a phonon momentum contribution (lattice vibration) must be involved to conserve crystal momentum.[26] This results in a transition where the phonon energy will assist the photon energy to overcome the band gap:

$$E_{\gamma} \geq E_{BG} - \hbar\omega_{p} \tag{3.7}$$

where ω_{p} is the phonon frequency. This phonon energy is typically very small, normally a few hundredths of an electron volt, thus it is only of note in very small band gaps.[26] Photoconductivity makes semiconductors good materials for photodetection applications in the UV to IR spectrum.

3.4. Strongly Correlated Materials

The classification of materials as metals, insulators, or semiconductors is an appropriate approach for many materials.[31] However, some materials, in particular Transition Metal Oxides, present a greater challenge to explain due to a partially filled electron band (for VO_2 the d-band) like a metal, but poor conductivity at low temperatures like an insulator/semiconductor.[32] These materials, called strongly correlated materials, display anomalous behavior due to strong electron interactions along the lattice leading to dramatic changes in material properties (i.e. dramatic changes in resistivity) if a critical threshold (such as temperature) is met. The most famous and studied of these is the change from an insulating/semiconducting state to a metallic state through an insulator/semiconductor to metal transition (IMT) making the state of the material a controllable parameter. Understanding this phenomenon has been a focal point of much research for the past 80 years.[32,33] The focus of the research presented in this study is in the insulating state of VO_2. Thus, I will give a more detailed explanation of the insulating state and limit the discussions on the IMT and metallic state which are examined extensively by references [32,33].

3.4.1. Anomalous Insulating Phase

In 1937, R. Peierls proposed a model to address the anomalous insulating behavior for strongly correlated materials. In this model, a string of evenly spaced one-electron atoms are arranged in a 1-D lattice such that the orbitals of each atom results in a single half-filled band.[32,34] However, a one dimensional, equally-spaced, chain of ions with one electron per site is unstable. This instability results in every other ion moving closer to one neighbor and further from the other by a distance δ as shown in Fig 3.3. [32,34] This spacing adjustment results in a doubling of the lattice period, often called dimerization, splitting the partially filled band into filled and unfilled bands. This splitting is energetically favorable when the energy savings from the new band gap outweighs the energy required to rearrange the ions, thus, the band splitting is only favorable at lower energies (temperatures). Therefore, the insulating state is seen only at lower temperatures as higher temperatures would be metallic due to the collapsed band splitting, shown in Fig 3.3.

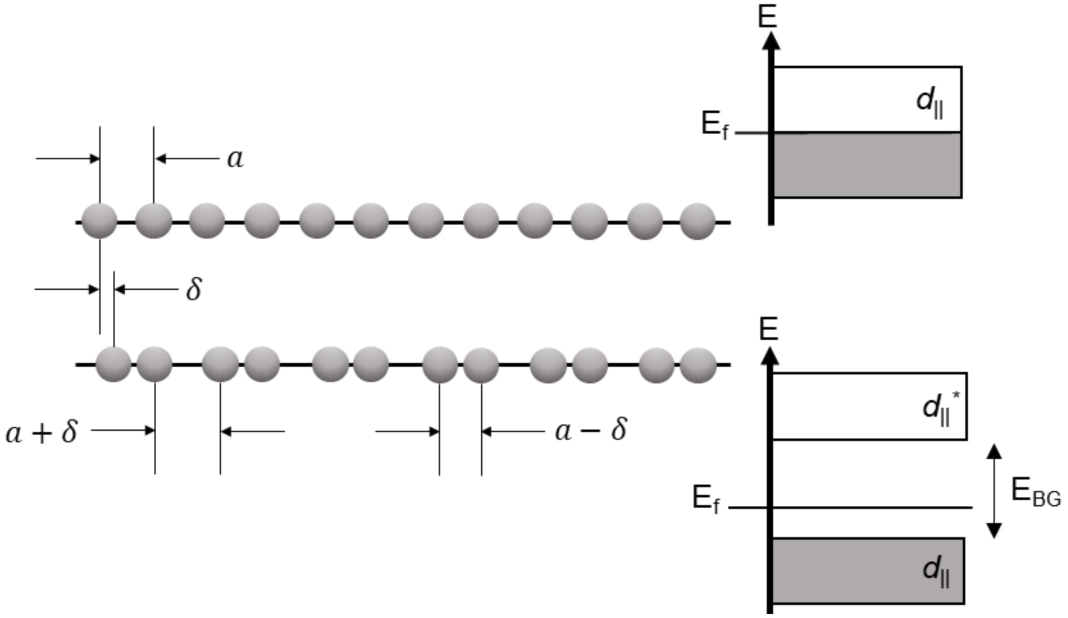

Figure 3.3: The Peierls model lattice distortion. The top lattice is the metallic phase lattice with lattice spacing a (left) and associated metallic band structure (right). The bottom lattice is the insulating phase lattice with lattice distortion δ demonstrating the dimerization of the lattice(left) and associated insulating band structure (right).

In 1949, N. Mott proposed an alternative model to explain the anomalous insulating behavior using the strong coulomb repulsion between electrons in sites along the lattice. [32,33,35] This interaction uses a lattice where each site has a single electron orbital and the overlap of adjacent orbitals forms a band that can accommodate a maximum of two electrons, one spin up and one spin down. In the no coulomb repulsion model, the sites fill with one electron per orbital resulting in a single partially filled band; this filling continues until two electrons occupy each site resulting in a single fully filled band. However, if two electrons occupy the same site the electrons will feel a strong coulomb repulsion between each other causing the d-band to split into two separate bands. The lower band forms from electrons that occupy a previously empty site and the upper band results from electrons that occupy an already occupied site shown in Fig 3.4. In the case of one electron per site, the lower band is completely filled with an empty upper band, resulting in the insulating properties despite the partially filled d-band. One important aspect of the split band is the Fermi level now exists between the two split d-bands in the band gap. The filled lower d-band exists below the Fermi level with the second filled band, the p-band, occupying what would be the first fully filled band in a metal, as shown in Fig. 3.4.

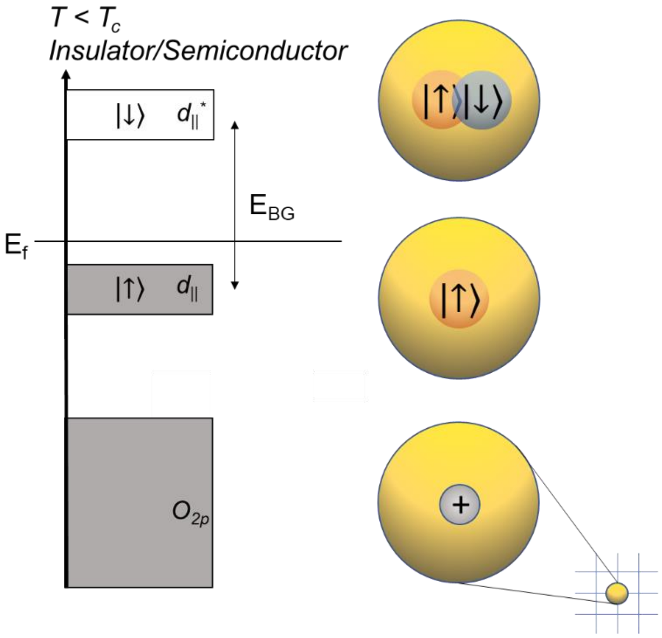

Figure 3.4: The Mott model of strongly correlated electrons. The band structure of the insulating phase (left) with the filling notated by |↑⟩or |↓⟩. The lattice site orbital filling (right).

3.4.2. Returning the Metallic State

The method of returning to the metallic state for a strongly correlated material, is dependent upon which model is used for the insulating state (i.e. the Peierls model or the Mott model). Returning to the metallic phase, for the Peierls model, requires supplying enough energy to make the rearrangement of the atoms energetically unfavorable (i.e. high temperature) resulting in the lattice returning to its metallic periodicity collapsing the band gap.[32,34] However, the approach from the Mott model involves supplying the electrons in the lattice with enough energy (i.e. high temperature) to move freely, reducing the strong coulomb repulsion effect seen with stationary electrons, collapsing the band gap.[32,35]

It is important to state that although these models for strongly correlated materials are presented as distinct approaches; the experimental evaluation of strongly correlated materials, such as VO_2, seem to show both structural and electronic transitions in what appears to be a concurrent fashion. This has led to significant investigation into the nature of the IMT and the dominant cause continues to remain unclear.

CHAPTER 4

Transition Metal Oxides

In 1937, de Boer and Verwey reported that many Transition Metal Oxides (TMOs) possessing partially filled d-electron bands were poor conductors.[32,34,36] This behavior would spur investigations into strongly correlated materials and their insulator to metal transition (IMT) as discussed in the previous chapter. TMOs continue to be a technologically valuable material type due to attributes of strongly correlated materials. For the purposes of this study, we will focus on the properties of two TMOs: vanadium dioxide (VO_2) and titanium dioxide (TiO_2).

4.1. Introduction to Vanadium Dioxide

One of the most interesting groups of TMO materials is the vanadium oxides. Most compounds in this group display partial filling of the 3d-band while retaining insulating behavior with a characteristic IMT. Of the vanadium oxides, vanadium dioxide (VO_2) is one of the most studied compounds.[i] The level of interest arises from the reversible IMT near room temperature, at 68°C, accompanied by a reversible structural transition from the insulating, monoclinic structure to the metallic, rutile structure.[37,38,47,48,39–46] This IMT and structural change in VO_2 complicates separating the main mechanism that causes the d-band splitting by possessing features reminiscent of both the Mott model and the Peierls model. This problem has proven to be non-trivial, and the origin of the insulating state is not completely known. However, the origin of this insulating phase is not essential for understanding the mechanisms at work in this study. Therefore, I will provide a short introduction on the origins of the VO_2 insulating phase and focus on the relevant crystal and electronic structure.

In 1959, F. Morin discovered that the IMT of VO_2 was accompanied by a structural transition leading to two distinct theoretical descriptions. The first description in 1971 by J. Goodenough examines the IMT framed in the Peierls

---

[i] Approximately 16,000 articles published on VO_2 since 2018 via search on Google Scholar

model.[32,49] Goodenough argues that the distortions in the vanadium-vanadium (V-V) chains in the VO_2 monoclinic structure, shown in Fig 4.1, solely drives the separation of the d-band in the insulating state, (shown in Fig 4.2) thus the structural transition from monoclinic to rutile alone drives the band gap collapse.

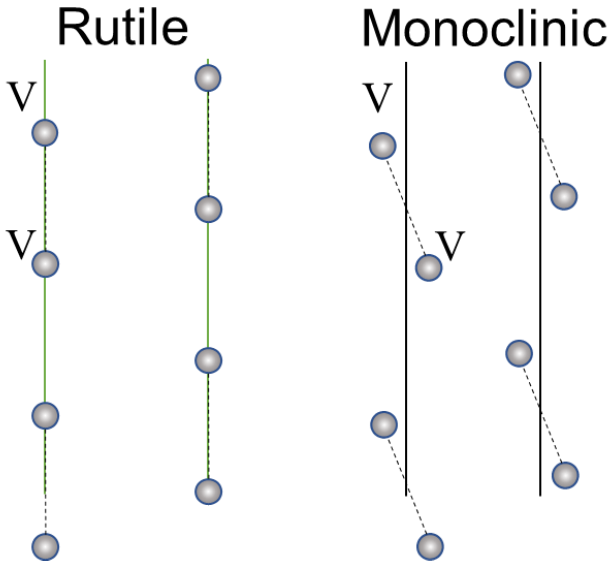

Figure 4.1: The vanadium dimer adjustments between the rutile and monoclinic structures.

Shortly following the work by J. Goodenough, A. Zylbersztejn and N. Mott argued in 1975 that the V-V chains are insufficient to match the experimentally determined d-band gap separation in VO_2 . Thus, the band gap separation requires electron correlations to be the dominant mechanism to accurately match the experimental band separation.[50] It is important to note that the effects predicted by Goodenough likely contribute to the band gap separation, though it is not the dominant mechanism. In the following 40 years, investigations into the origin of the insulating state yielded results supporting a purely Peierls approach is insufficient to properly separate the band gap. [33,50–55] The extent to which it fully contributes is still unknown, lending ambiguity to understanding the dominant mechanism for the insulating state.

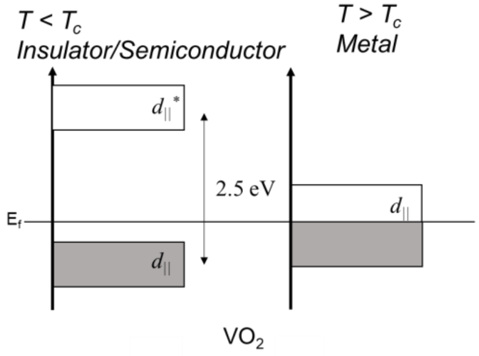

Figure 4.2: Band gap collapse of the VO_2 $d_{||}$ band between the insulating and metallic state.

Though the dominant mechanism for the VO_2 insulating state remains debated, one only needs the electronic and crystal structure of the insulating state to understand how VO_2 is used for detection applications. Thus, I present the experimentally determined structures of the VO_2 insulating state focusing on the M_1 insulating phase and the rutile metallic phase.

For the VO_2 crystal structure, the lattice positions of the vanadium and oxygen atoms are well known both experimentally and theoretically for both the rutile (metallic) and M_1 monoclinic (insulating) phases.[32,47,56–60] The space groups for these two phases of VO_2 are $P4_2/mmm$ (space group 136) for rutile and

$P2_1/c$ (space group 14) for monoclinic.[56] Both crystal structures are shown in Fig 4.3. The rutile structure of VO_2 is considered to be the most stable with stability between 68°C to 1540°C, making this phase an ideal structure for stable film growth and, indeed, most film growth of VO_2 occurs in the rutile phase temperature range.[20,56,61–64] The lattice parameters of the rutile phase are $a_R = b_R = 4.55$ Å and $c_R = 2.88$ Å, shown in Fig 4.3a. [56] The monoclinic structure is a distortion of the rutile lattice in the insulating phase appearing below 68°C. This distortion of the lattice reduces symmetry, in comparison to the rutile phase, and results in a change of lattice parameters making $a_M = 5.77$ Å, $b_M = 5.42$ Å, and $c_M = 5.38$ Å with an angular shift of $\beta_M = 122.6^o$ where $\beta_R = 90^o$. [56] The a_M lattice parameter in the monoclinic phase results from the lattice doubling of the rutile c_R parameter with the V-V connections now at two separate lengths a_{1M}=2.61 Å and a_{2M}=3.16 Å displayed in Fig 4.3b). The adjustments between these two phases shows the degree of lattice distortion between the rutile and monoclinic phases.

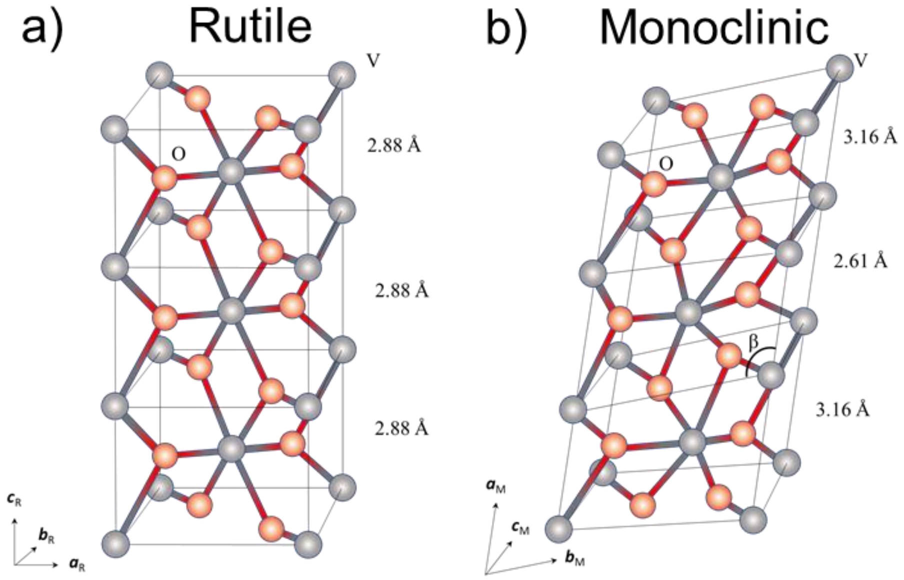

Figure 4.3: The rutile and monoclinic structures of VO_2 for three unit cells with the lattice distortions demonstrated by the lattice spacing of the c_R and a_M axis.

The band structure, like the lattice structure, displays a distinct difference between the insulating and metallic phases. Experimental studies on the electronic structure of VO_2 confirm: the band structure of the insulating and metallic phases are like the band structure suggested by Mott, and later Goodenough and Zylbersztejn.[33,35,49,50] Fig 4.4 shows that the insulating phase is characterized by d-band splitting into $d_{||}$ and $d_{||}^*$ bands, separated by a band gap of approximately 2.5 eV.[52,65] Additionally, the location of the π^* band, due to a strong 3d-2p hybridization between the π^* and O_{2p} bands, shifts the π^* band ~0.5 eV above the Fermi level. The O_{2p} band is located ~2.5 eV below the Fermi level. [66–68] In the metallic phase, the band structure is analogous to a typical metal, where the highest filled band (the $d_{||}$ band) is partially filled. The metallic state, from the collapse of the split insulating d-bands, results in a single partially filled band, shown in Fig. 4.4, which increases the conductivity in the metallic state of VO_2. The metallic phase π^* band, additionally, collapses to the Fermi level leading to a large degree of overlap between the π^* and $d_{||}$ band. These structures have been confirmed with experimental studies, though, there is a degree of discrepancy between the band spacing potentially due to choices of growth method, sample preparation, and substrate choice for the materials.[32,33,50,58,69]

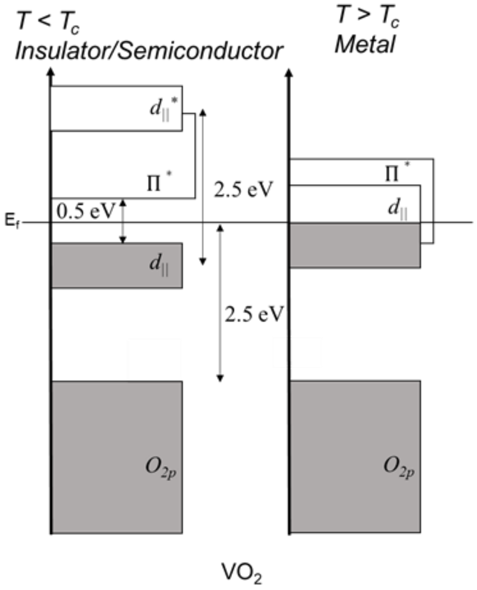

Figure 4.4: The band structure for VO_2 for the insulation and metallic phases where the band spacing is noted for the insulating phase.

4.2. Introduction to Titanium Dioxide

Titanium Dioxide (TiO_2) is another TMO that has experienced a great deal of interest in the areas of optical detection and photocatalysis.[13,70–73] It is important to note that TiO_2 is substantially different from VO_2. TiO_2 is not a strongly correlated material and does not display an IMT; instead, TiO_2 is classified as a wide band gap semiconductor with a band gap of 3.0 eV, as shown in Fig. 4.5. Despite TiO_2 not displaying the exotic behavior of VO_2, it is highly studied due to its own set of technologically valuable properties originating from its crystal and electronic structures. [13,70–77]

TiO_2 exists in three possible structures: the anatase, brookite, and rutile structures, among which rutile has the greatest applicability to VO_2 growth and optimization. The rutile space group of TiO_2 is $P4_2/mmm(136)$ matching the rutile phase space group of VO_2. The rutile phase, additionally, has a lattice structure similar to rutile VO_2 with lattice parameters of $a=b=4.59$ Å and $c=2.96$ Å, giving an ideal substrate growth surface for the VO_2 thin film. In addition to the optimal growth surface, the rutile phase is highly stable under high temperature, making it an ideal substrate on which to optimize VO_2 growth.[74–79]

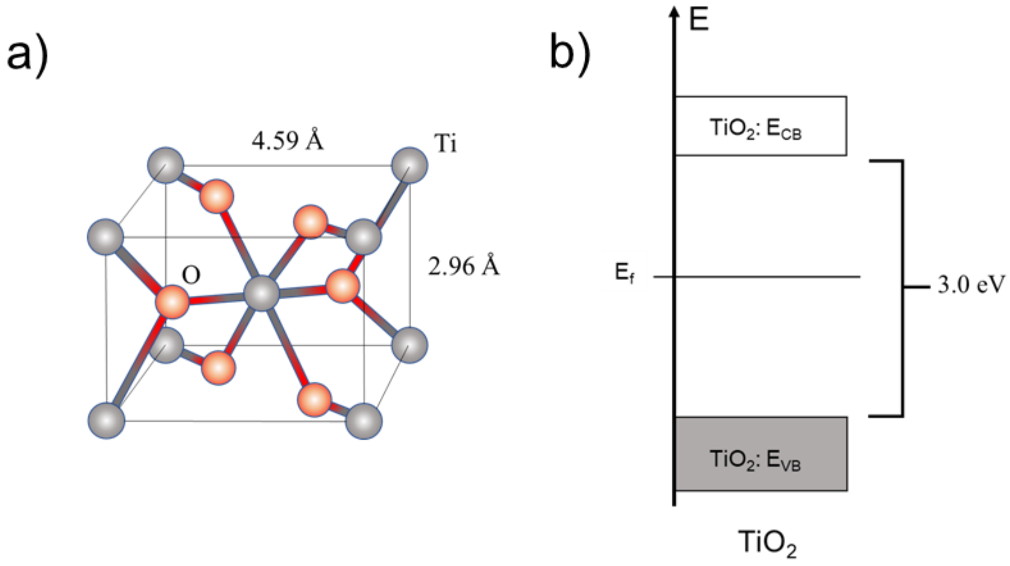

Figure 4.5: a) TiO_2 rutile structure unit cell with lattice spacing noted b) the semiconductor band structure of TiO_2 where E_{VB} is the valence band and E_{CB} is the conduction band.

The electronic structure of the TiO_2 presents an ideal semiconductor band gap of 3.0 eV to optimize a broadband UV (≥3.0 eV) photodetector, with the 3.0 eV band gap matching deep blue NUV light (410 nm). The large band gap makes the TiO_2 sensitive to carrier excitation in the UV, and insensitive to carrier excitations for wavelengths greater than 410 nm. It is important to note that though the TiO_2 shows carrier excitations in the UV, these carrier excitations in TiO_2 recombine too fast for practical detection electronics.[70,71,80] Noting, this photosensitivity in the TiO_2 is adjustable by ion doping, which will be investigated in Chapter 8.[76,81–84] Ultimately, these properties made using TiO_2 in engineering a UV detector a natural choice to pair with VO_2.

4.3. The TMO Heterojunction

The heterojunction of one TMO onto another elicits a number of interesting phenomena originating from adjustments of the two material's d-electrons at the interface.[85] This phenomena adjusts charge, orbital, and spin configurations of the lattice sites in the heterojunction region, altering the electronic structure of each TMO at the interface by methods such as band bending, discussed in Chap 8.[71,80] The adjustments to the electronic structure in the heterojunction leads to the manifestation of emergent phenomena not found in either TMO independently.[85]

In the case of VO_2 grown on TiO_2 substrates (namely niobium doped TiO_2 (TiO_2:Nb)), the heterostructure can undergo a process called photohole injection when illuminated with ≥3.0 eV (≤410 nm) light. This process begins with efficient separation of the photogenerated electron-hole pairs in the heterojunction region. The photogenerated free electrons are driven from the heterojunction interface toward the bulk, while the remaining holes tunnel from the TiO_2:Nb valence band to the VO_2 O_{2p} band, increasing the population of holes in the VO_2 O_{2p} band. In the end, the free carriers in the VO_2 move to the photoinjected holes. Such a phenomenon is not possible in either the VO_2 or the TiO_2 individually and requires the formation of the TMO heterojunction. This process is shown for TiO_2 in Fig. 4.6 and is explored in depth throughout the remainder of this study.

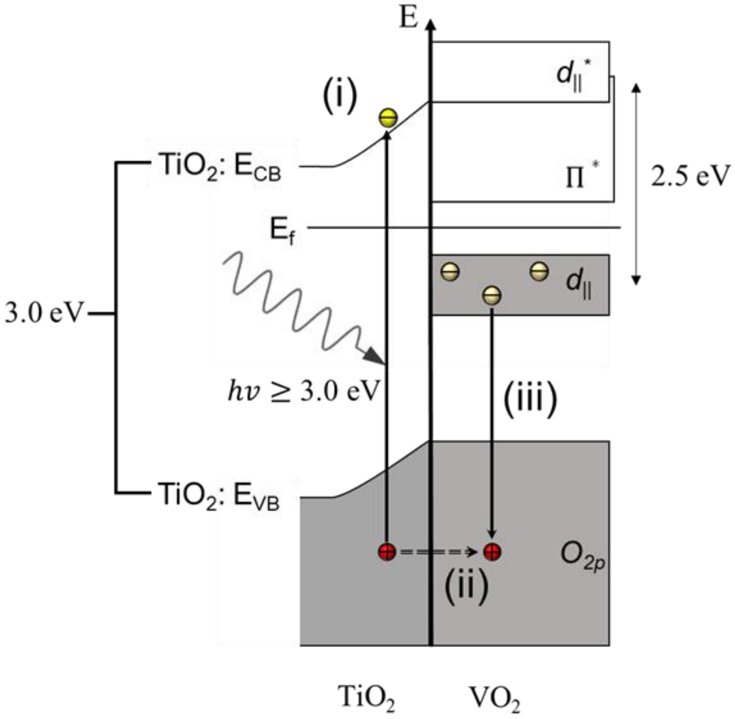

Figure 4.6: The photohole injection mechanism for the VO_2 on TiO_2 heterostructure where (i) is the electron photoexcitation across the band gap, (ii) is the photogenerated hole tunneling from the TiO_2 to the VO_2, and (iii) is the recombination of free electrons in the VO_2 $d_{||}$ band to the photoinjected hole.

CHAPTER 5

Experimental Methodology

In this section, I discuss the experimental methods used to prepare and characterize the VO_2 thin films grown for this study. This section begins with an overview of thin film deposition techniques. It then proceeds by describing the characterization techniques used for determining the relevant morphological, microstructural, and photoconductive properties of the samples.

5.1. Deposition Techniques

As discussed in the Chapter 2, thin films grow in three initial steps: adsorption, nucleation, and coalescence. Thin film growth is possible with a number of deposition techniques depending upon: the desired film properties, substrate dimensions and shape, material type, and/or availability. These methods are classified in to one of two categories: Chemical Vapor Deposition (CVD) or Physical Vapor Deposition (PVD). For this study, the primary deposition method is a PVD technique. However, I will provide a short description of both general methods before discussing, with greater depth, the deposition method used for all VO_2 films in this study.

5.1.1. CVD and PVD Introduction

The CVD method uses a gas phase diffusion process along the substrate surface. Therefore, these processes requires a gas to be transported across the substrate using either a compressed gas or a vaporized solid/liquid.[22,23] This supplied gas/vapor reacts with the substrate surface in a combination of adsorption, surface diffusion, heterogeneous reaction of the adsorbates, and desorption of gaseous by products.[24] The greatest benefits of CVD techniques is the high degree of control over stoichiometry and conformity of reaction, this allowing very thin (down to one atomic layer) homogeneous film growth over the entire surface.[23,24] However, these techniques are generally difficult to scale up to larger substrates and some precursors used in the CVD process are toxic or otherwise dangerous, requiring expensive chambers and safety equipment.[23]

Alternatively, PVD techniques use the vaporization of a solid (or liquid) material transported to the substrate in a line of sight orientation.[22,23] The vaporization of a material is possible through either vacuum evaporation or sputter deposition processes. The vacuum evaporation process (shown in Fig 5.1a) uses thermal vaporization of a source material, in which the vaporized material travels in a line of sight trajectory toward the substrate. This process requires minimal interaction with the environment, thus a low-pressure vacuum is necessary. [22,23] Advantages and disadvantages of vacuum evaporation can be found in Table 5.1.

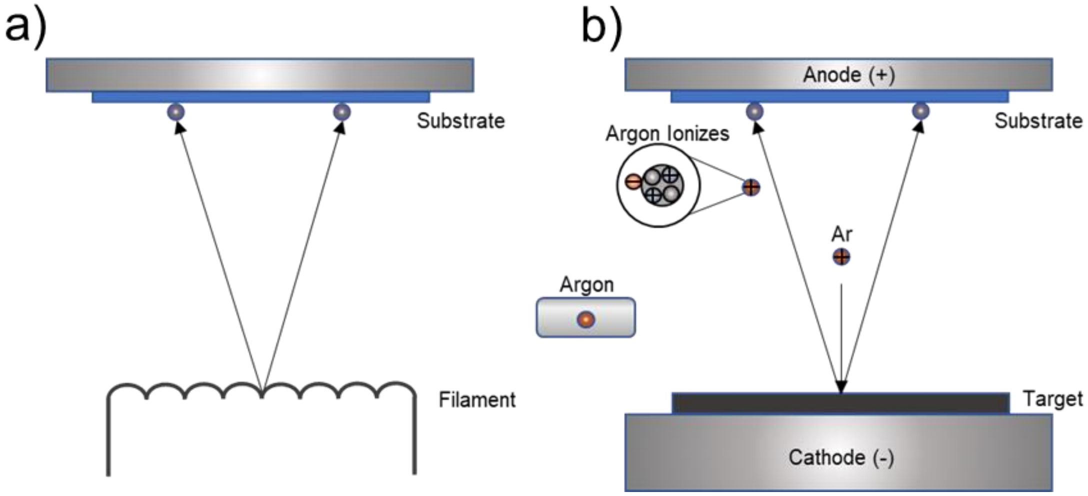

Figure 5.1: a) Vacuum evaporation of a filament b) DC sputtering of a target in an argon environment.

Contrasting vacuum evaporation, sputter deposition, shown in Fig 5.1b, uses the non-thermal vaporization of a source material by impinging ionized gas particles on a target material. Collisions between the ionized particles and the target material result in a momentum transfer between the gas ions and the target material. These collisions eject the vaporized target material in a line of sight trajectory toward the substrate. [22,23] Sputter deposition is divided further into two categories depending on the ion source being either an ion gun or a plasma.[22,23] I will focus on plasma-assisted sputtering as it is the most relevant to the deposition technique for VO_2. In the plasma-assisted sputtering, otherwise known as *DC sputtering*, a chamber is filled with a low-pressure of inert gas (typically argon), and an electric potential is applied to the target material by making the target a cathode and the substrate an anode. This potential difference creates an electric field perpendicular to the target's surface ejecting and accelerating free electrons toward the substrate. These free electrons interact with the argon environment, ionizing it and forming a plasma.[22,23] The argon ions then accelerate toward the negatively charged target material, impacting and ejecting (sputtering) particles of the target material. Potential advantages and disadvantages of (Plasma Assisted) Sputtering can be found in Table 5.1. In this study, all films were deposited with *pulsed DC magnetron sputter deposition* in a reactive (oxygen) environment discussed on the next section.

Table 5.1: PVD Processes Advantages and Disadvantages[22]

PVD Processes	
Vacuum Evaporation	(Plasma Assisted) Sputtering
Advantages • Fast and cost efficient for depositing films • Potential for large source areas providing deposition for large substrates • High purity films are easily deposited from high purity source materials with a low vacuum pressure (10^{-5}-10^{-9} Torr)	Advantages • Any material can be sputtered and deposited in a stable and long-lived vaporization • Sputtering of a solid can be oriented up or down and can be configured for a multitude of substrate sizes and geometries • Yields highly reproducible films • Allows for a greater degree of control over the film quality due to additional *in-situ* variables
Disadvantages • Highly susceptible to contamination if the vacuum pressure is not low enough (10^{-5}-10^{-9} Torr) • High susceptibility to substrate surface defects • Inability to deposit many alloy and compounds • Few *in-situ* variables to control film quality	Disadvantages • Sputtering ejection patterns tend to be non-uniform • Sputtering targets are often expensive and must be cooled • Vaporization rates are low in comparison to Vacuum Evaporation • Target material usage may be low • Contaminants can be activated from a plasma increasing contamination rates

5.1.2. DC Magnetron Sputtering

The *DC magnetron sputtering* process uses a target material placed on a set of permanent magnets. An electric field is then introduced by making the target cathodic and the heater/substrate anodic. This electric field accelerates the free electrons in the system toward the substrate, as in typical DC sputtering. However, with *DC magnetron sputtering*, the electric and magnetic fields interact with the free electrons close to the target surface by deflecting the electrons in the $-\vec{E} \times \vec{B}$ direction. The interaction of the electric field and the magnetic field on the electron results in a helical motion, with changing pitch, around the magnetic field lines and an overall drift in the $-\vec{E} \times \vec{B}$ direction, where the electron is reflected when it comes close to the negatively charged target.[86,87] Thus if the gyro radius (r_g) of the helical electron motion is small enough, i.e. the electron is not scattered by another particle, it becomes confined or trapped in a closed path near the target surface.[86,87] Here the gyro radius r_g is:

$$r_g = \frac{mv_\perp}{qB} \tag{5.1}$$

where $v_\perp$ is the electron velocity perpendicular to the flux lines, q is the electron charge, B is the magnetic field strength, m is the mass of the electron.[86] In practical sputtering cases, the necessary gyro radius for confinement is typically a few millimeters or less.[86] This electron trapping makes the confined region more cathodic than the rest of the target effectively increasing the intensity of the plasma near the target surface. This more cathodic region accelerates the ionized argon at a greater rate toward the confined electron region (shown in Fig. 5.2) yielding a high sputtering rate, at lower applied potential than in traditional DC sputtering. [22,23,86] However, the sputtering becomes focused in the confined electron region reducing the overall target material usage.

5.1.3. Reactive and Pulsed Magnetron Sputtering

Reactive magnetron sputtering pairs the above DC magnetron sputtering with a partial pressure of reactive gas added to the argon environment. The reactive species vary depending upon the desired film, though the two most common gasses are nitrogen and oxygen. The gas used for the VO_2 growth was oxygen. [22,23] In general, reactive gasses have a low atomic mass making the reactive species inefficient at sputtering material making argon necessary to maintain stable sputtering rates. [22,23] Instead, with elemental (vanadium) sputtering, the reactive gas is used to react with the sputtered material, shown in Fig. 5.2. During sputtering, this reactive gas exists in its molecular state or in a “plasma activated state”. The plasma activated gas is a more chemically reactive, due to the electron and ion collisions separating the gas molecules, for example when O_2 gas is activated it forms the more reactive O and O_3. These reactive gasses allow oxide film growth such as VO_2. Noting, VO_2 thin film growth is achievable with several deposition techniques. However, reactive sputter deposition gives excellent control over the partial pressure and temperature ranges where VO_2 growth is notoriously sensitive.[20,88–90]

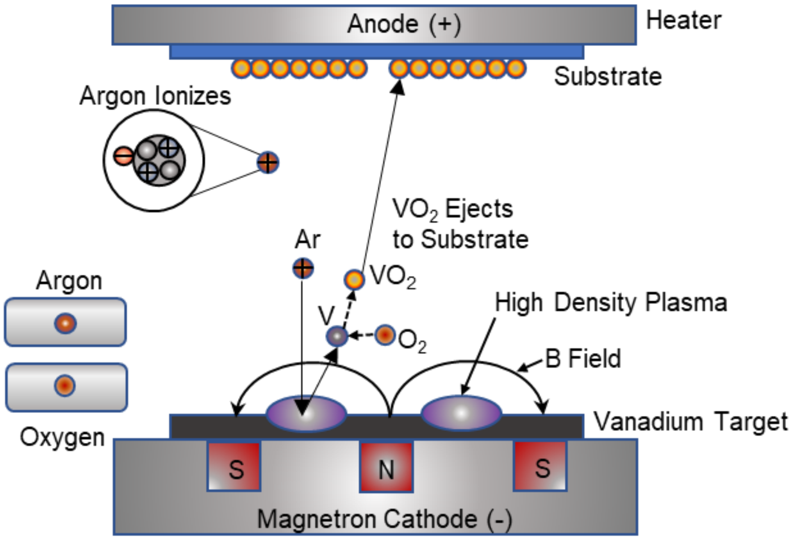

Figure 5.2: Reactive DC Magnetron Sputter Deposition. Where the B field is the magnetic field. The vanadium and oxygen reaction is shown with arrows as reactions to form VO_2.

Sputtering in a reactive (oxygen) environment inevitably develops oxide compounds on the target. These oxide compounds are of particular issue in sputtering because an oxide layer behaves differently than the original target metal species. Namely, the oxide compounds have increased secondary electron emission resulting in positive charge buildup, with positive ions remaining on the target surface. This build up of positive charge reduces sputtering yield by decreasing the acceleration of the argon ions leading to a complete cease of sputtering. To remedy this build up, the cathode must be periodically pulsed and held at a positive charge to dispel the charge from the target surface. For our VO_2 growth, the target was held positive for 3µs in a cycle frequency of 100 kHz giving a 30% duty cycle for holding the target positive. Failing to remove the positive charge can lead to dielectric breakdown causing arcing in the chamber potentially damaging the target and/or the system. Using this growth method, the VO_2 growth was calibrated to be ~5 Å/min. At this point, I have introduced the aspects of *pulsed DC magnetron sputter deposition* required for VO_2 film growth. For further information on the growth calibration of the VO_2 thin films, Section A.1 is an overview of the steps to calibrate the VO_2 growth.

5.2 Structural Characterization Methods

Following film deposition, various techniques were used to assess the structural properties of the films: Atomic Force Microscopy (AFM), X-ray Diffraction (XRD), X-ray reflection (XRR), and Reflection High Energy Electron Diffraction (RHEED).

5.2.1 Atomic Force Microscopy

Atomic force microscopy is a surface analysis technique which directly measures the intermolecular or “atomic” forces between a sharp probe tip and the sample surface. This technique gives atomic (angstrom) resolution imaging of the sample surface with advantages, such as superior resolution, 3D surface measurements, little or no sample/substrate preparation, and operation in ambient air. Thus, AFM is a valuable tool to extract topographical information from sample's surface. [91] The topographical information gives insights into the surface properties of a sample and how these properties develop with sample changes (i.e. thickness).

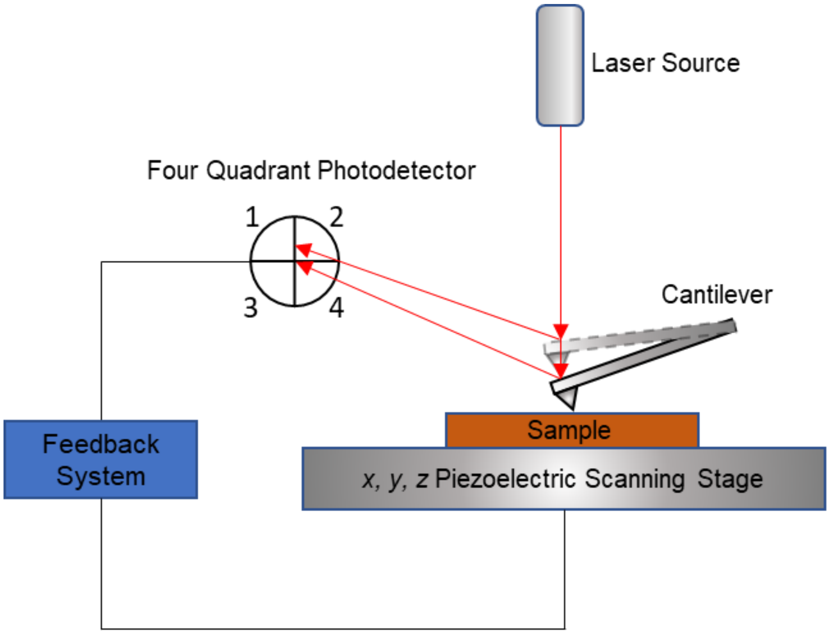

Figure 5.3: Diagram of the AFM system where deviations of the cantilever correspond to movement of the reflected light in the photodetector.

The AFM system, shown in Fig. 5.3, consists of: (i) a piezoelectric scanning stage capable of moving with picometer precision along x, y, and z directions (ii) a silicon cantilever with probing tip of ~10 nm diameter (iii) a 632 nm laser reflected off the back of the cantilever into a four quadrant photodetector to measure cantilever displacements and (iiii) an electronic control and feedback system that couples the response of the cantilever to the piezoelectric positioning.

This system runs in three modes, shown in Fig 5.4: (i) contact mode: the probe tip is in constant direct contact with the surface, (ii) tapping mode: the probe tip is oscillated up and down periodically tapping the surface, (iii) non-contact mode: the tip is oscillated above the sample (typically 50 – 150Å) but makes no contact with the surface. [91] For this study, non-contact mode was used to evaluate all surfaces.

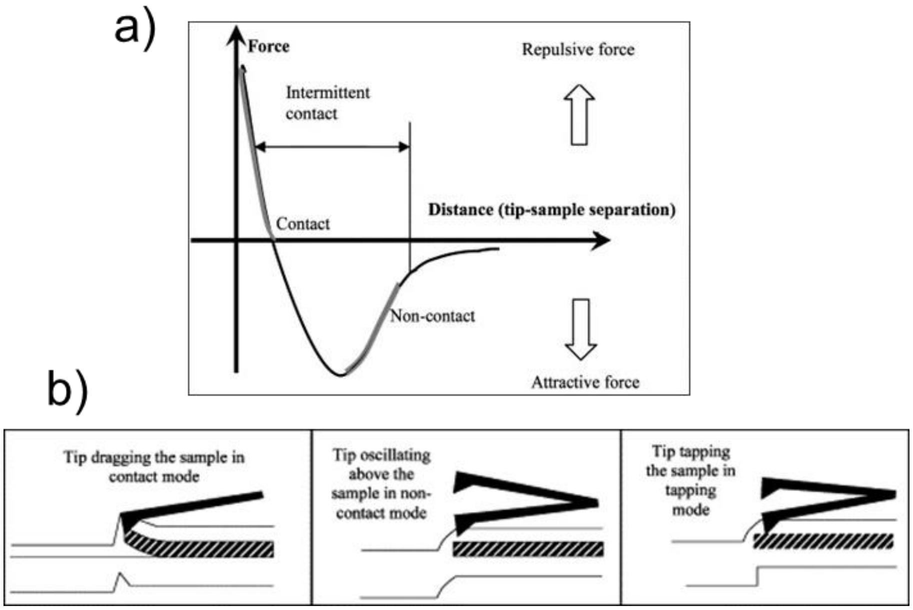

Figure 5.4: a) The AFM scanning regions where interatomic force variation versus distance between AFM tip and sample is shown. The separate contact regions are highlighted on the curve b) a representation of the contact types for the AFM tip interacting with a surface with contact mode (left), noncontact mode (middle), and tapping mode (right) and the lines represent an example of the tip reaction (top) and produced line scan (below) when moving over an object (striped box)(reproduced from [91] with permission from the author and Elsevier Publishers)

In non-contact mode, the tip to surface interaction is from weakly attractive van der Waals forces. The weakness of attraction requires the tip to be oscillated near its characteristic resonant frequency (typically between 100 and 400 kHz) with changes to the amplitude, frequency, or phase of the oscillation monitored by the laser and photodiode. The changes are converted into an electrical signal which is recorded by the WSxM software to reconstruct the surface. [92] These signals are also sent to the electronic control feedback system to ensure consistent cantilever height above the sample for the entirety of the scan (i.e. keeping the van der Waals force constant). Using the sensitivity of this technique, we construct highly detailed images of the VO_2 surfaces.

5.2.2 X-Ray Diffraction

One of the most valuable tools for analyzing a film's crystallography is X-ray diffraction (XRD). Using the ionization of a target source (i.e. Copper), we generate intense X-ray radiation, at certain characteristic wavelengths, determined by the atomic structure of the source. For this study, the relevant characteristic wavelength is λ=1.5406Å called the Cu $K\alpha_1$ excitation wavelength. The X-rays are directed incident upon a crystalline sample producing a diffraction pattern giving quantitative and qualitative descriptions of the sample crystal structure. The condition for constructive interference from crystal diffraction is determined by the Bragg diffraction condition[26,93,94]:

$$2d\, sin\theta = n\lambda \tag{5.2}$$

where n is the integer order of diffraction, λ is the X-ray wavelength, d is the distance between diffraction planes, and θ is the angle between incident X-rays and the sample shown in Fig. 5.5. However, it is important to note that Eq. 5.2 is valid only when $\lambda \leq 2d$. When Eq. 5.2 is satisfied, the constructive interference appears as a peak in the diffraction pattern.

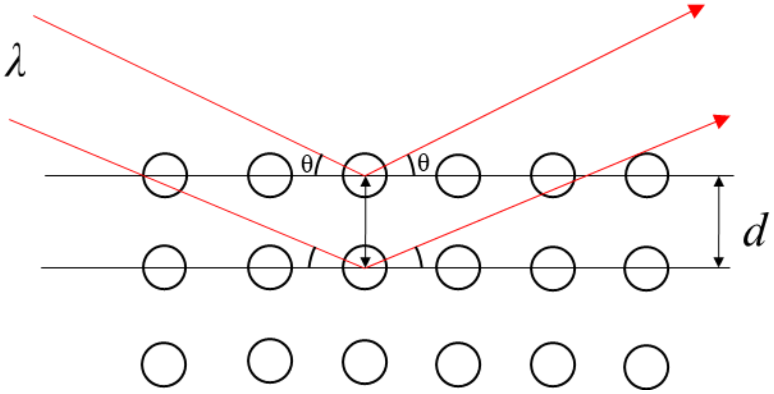

Figure 5.5: Diagram of X-Ray diffraction where λ is the incoming X-Ray wavelength, θ is the incoming angle for X-Rays, and d is the spacing between diffraction planes (lattice spacing).

Thin films tend to have weaker diffracted signal response than bulk materials (i.e. substrate) making alignment and signal optimization a challenge. The weak signal constraint makes slight misalignments detrimental to determining accurate diffraction patterns for a film. To address this difficulty, a four-circle goniometer, using multiple rotation axes, is used to achieve optimal film alignment. The typical four circle goniometer and relevant axes of rotation are shown in Fig 5.6.

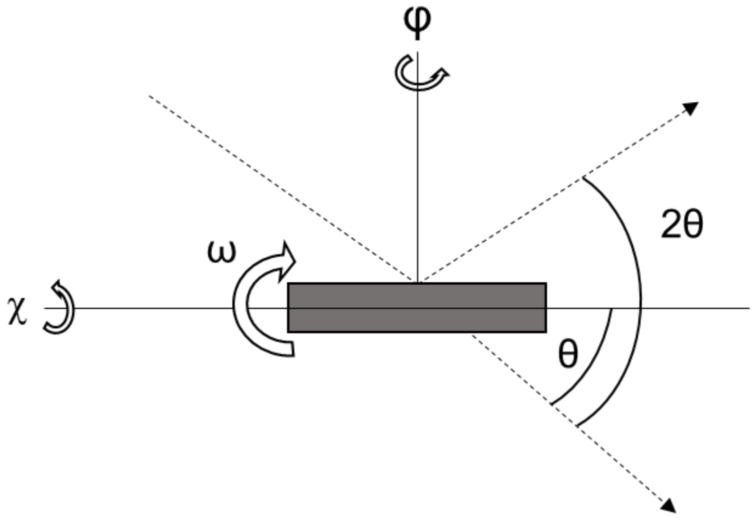

Figure 5.6: A typical four circle goniometer based on the "Eulerian cradle". The various rotation axes are noted.

The structural information assessed from XRD scans includes orientation of the crystal planes, lattice parameter, relative strain, crystallite grain size, and mosaic structure. To determine this information, I used a combination of high angle (θ-2θ) and rocking curve (ω) scans. The θ-2θ scan adjusts the detector (2θ) and X-ray source (θ) angles continuously maintaining $2\theta = 2 \cdot \theta + 2\theta_{offset}$. For θ-2θ scans, the diffraction peak location is compared to a standard powder diffraction reference sample giving information on the crystal planes, lattice parameter, and relative strain. The full width half maximum (FWHM) of the θ-2θ diffraction peak gives the crystallite grain size L by employing the Scherrer equation[93–95]:

$$L = \frac{K\lambda}{\beta\, sin\theta} \tag{5.3}$$

where K is the shape factor determined by the shape of the crystallites (for VO_2 K~0.9), λ is the X-ray wavelength, β is the FWHM of the diffraction peak, θ is the diffraction peak angle. In the ω scan, the angle of the X-ray source and detector are kept constant and the sample is tilted or "rocked" in the ω axis. This rocking gives a diffraction pattern where the FWHM determines the mosaicity or crystallite disorder. In practice, more disordered crystals return a broader diffraction peak due to the diffraction condition being satisfied by a greater number of misoriented crystallites along the ω rotation.

5.2.3 X-Ray Reflectivity

X-ray reflectivity (XRR) is a complimentary characterization technique to XRD. By using the X-ray beam at grazing incident angles, X-rays are reflected off the sample to determine further structural information of a film. Slight variations to the shallow angle of incidence varies the total reflected X-rays due to refraction into the sample. A second set of reflections from the refracted beam off the substrate additionally contribute to the total X-rays as shown in Fig. 5.7.

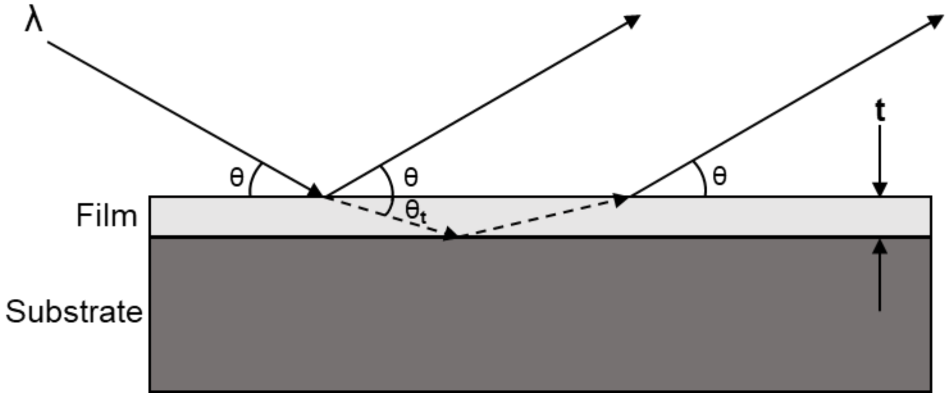

Figure 5.7: The reflected and refracted paths for X-ray reflectivity on the surface of a film. The paths shown in this diagram correspond to constructive interference from the reflected and refracted beams. Here t is the film thickness, θ is the incident X-ray angle, and θ_t is the refracted angle.

This combination of reflections between the film surface and the film/substrate interface interfere, resulting in oscillations of the total detected X-ray counts called Kiessig oscillations, shown in Fig 5.8. [93,96] The maximum of a given oscillation follows:

$$2t\ sin\theta_t = m\lambda \tag{5.4}$$

here,

$$\theta_t = \sqrt{\theta^2 - \theta_c^2} \tag{5.5}$$

where t is the film thickness, θ_t is the refracted angle, θ_c is the critical angle for the film, θ is the incident X-ray angle, m is an integer, and λ is the incident X-ray wavelength. Thus, thickness is found from the peak to peak differences between intensity oscillations. Additionally, this technique evaluates film density and roughness as shown in Fig 5.8. The density is determined from the location of the critical angle, which is associated with the electron density of the film. The amplitude of oscillation and the decay rate is related to the roughness, as roughness increases scattering and reduces the total X-ray intensity.[93]

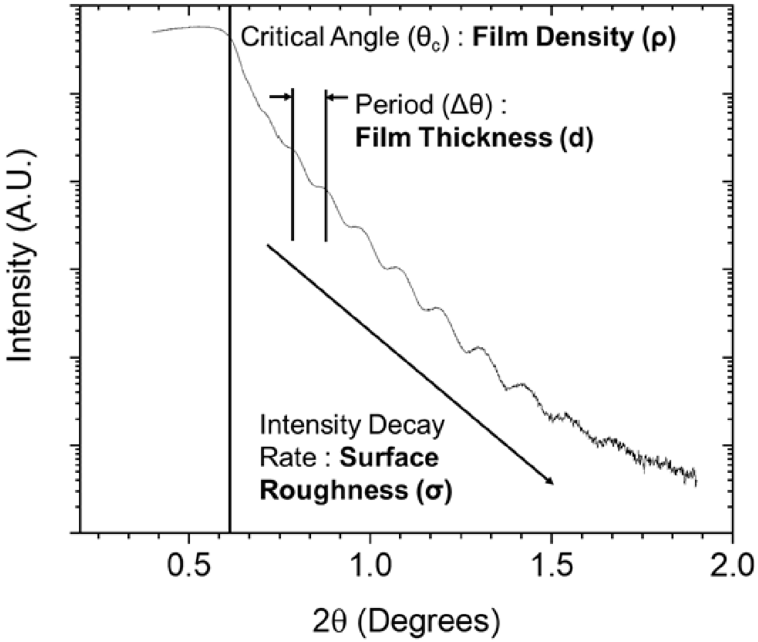

Figure 5.8: X-ray reflectivity example with the thin film information that can be determined from a scan including density, thickness, and roughness.

5.2.4 Reflection High Energy Electron Diffraction

Reflection High Energy Electron Diffraction (RHEED) is a separate diffraction based technique that is sensitive to the surface structure of the film. The surface sensitivity makes RHEED a powerful tool for extracting in-plane structural information, particularly lattice structure, of epitaxial films as well as assessing crystalline quality.[97,98] Thus, we used RHEED to assess the lattice structure and crystal quality of the epitaxial VO_2 films.

A RHEED system consists of an electron gun directed at the surface of a sample produces a diffraction pattern detected on a phosphor screen, shown in Fig 5.9. To ensure electron diffraction, the electric potential accelerating the electrons is adjusted to keep the probe wavelength smaller than the atomic spacing of the lattice. [97,98] This wavelength adjustment is possible due to the electron's de Broglie wavelength being related to its momentum. Considering the length scales of interest and system limitations, the electron energies were kept at 29 keV (λ=0.072 Å).

The electron beam directed at the film surface producing a diffraction pattern from the first few surface layers of atoms. This diffraction pattern is a direct measurement of the reciprocal lattice atomic positions for the surface. When compared to simulated diffraction patterns for a bulk lattice, shown in Fig 5.9b, the experimental diffraction patterns give information on the crystal quality, while allowing us to monitor the VO_2 lattice in real time.

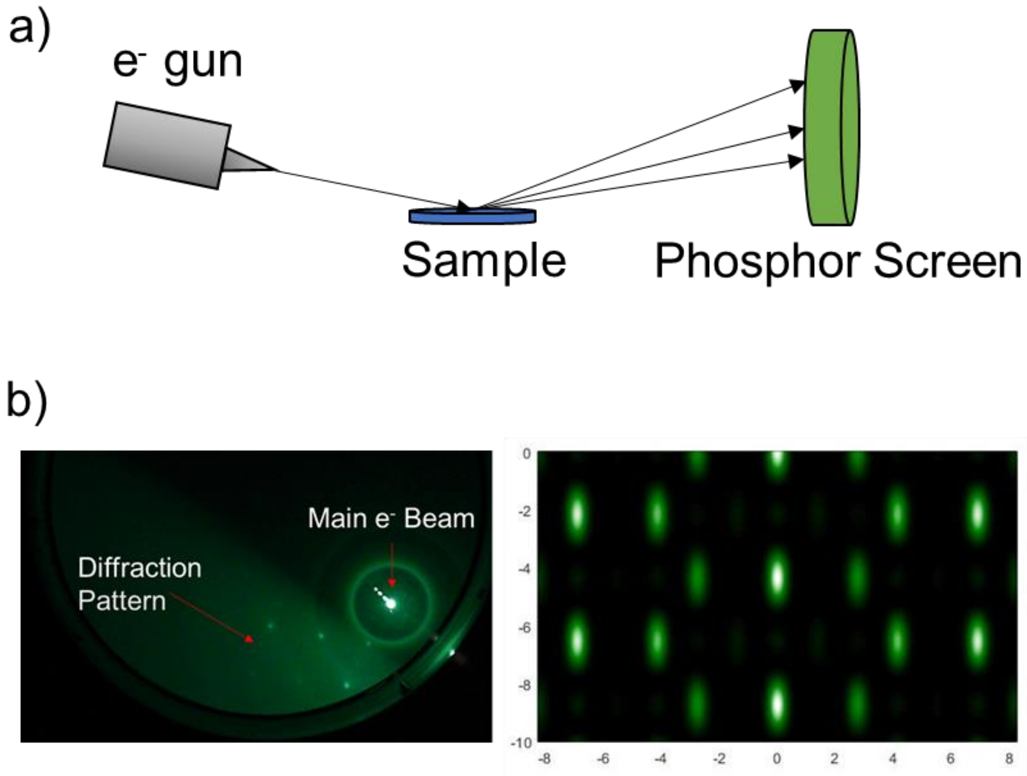

Figure 5.9: a) Diagram of a simple RHEED system. b) Examples of an experimentally produced RHEED diffraction pattern (left) and the simulated pattern (right)

5.2.5 RHEED Simulations

The simulations for this experiment were carried out using the RHEEDsim MATLAB program.[99] This software uses the atomic positions of the atoms determined from the space groups of the respective molecules. The program uses a kinematic approach for single scattering events, and then approximates the Ewald sphere to a planar surface to compute streak intensities. Additionally, intensity modulation extends to within the z direction.[99] This simulation yields realistic representations for comparison to experimentally determined RHEED diffraction patterns. Further information on this program is available at ref [99].

5.3 Photoelectric Characterization Methods

The photoconductive response of the films was assessed with a modified four-point probing station in a van der Pauw (probe tips at the edges of a sample) orientation. The van der Pauw method used determined the photoelectric and resistive properties of the samples by directly measuring the current, voltage, and resistivity of the VO_2 thin films via direct contact to the film surface.

5.3.1 Probing System

Four-point probing systems directly measure the electronic and conductive properties of a thin film. Probe systems are oriented in either an in-line or van der Pauw arrangement (probe tips at the edges of a sample). The van der Pauw method has advantages such as versatility in individual contact placement, non-destructive contact method, detection method customizability, and controllable material type allowing choice of work function and resistivity of the probes.

The probing system used in this study is a MMR technologies micro-probing station with beryllium copper probes. The micro-probing station gives micrometer precision to the probe tip placement for high precision probing of the thin film surface with minimal noise introduced into the system. The probe tips were connected to Keithley voltmeters, ammeters, and current sources (Keithley 2182a, 6220, and 2400) allowing high precision detection and testing of the electronic properties for each sample. A ceramic heater (Thorlabs HT24s) was used to probe changes to the electronic response with temperature. Finally, the probing system uses a set of light sources to illuminate the sample surface to directly probe the photoconductive response. The two light sources used were a 405 nm (blue) diode laser and a 254 nm (UV-C) Xe lamp. These wavelengths give information on two spectral regions of interest for UV detectors, especially neutron detectors as discussed in Section 1.1. The orientation of these sources in the probing station shown in Fig 5.10.

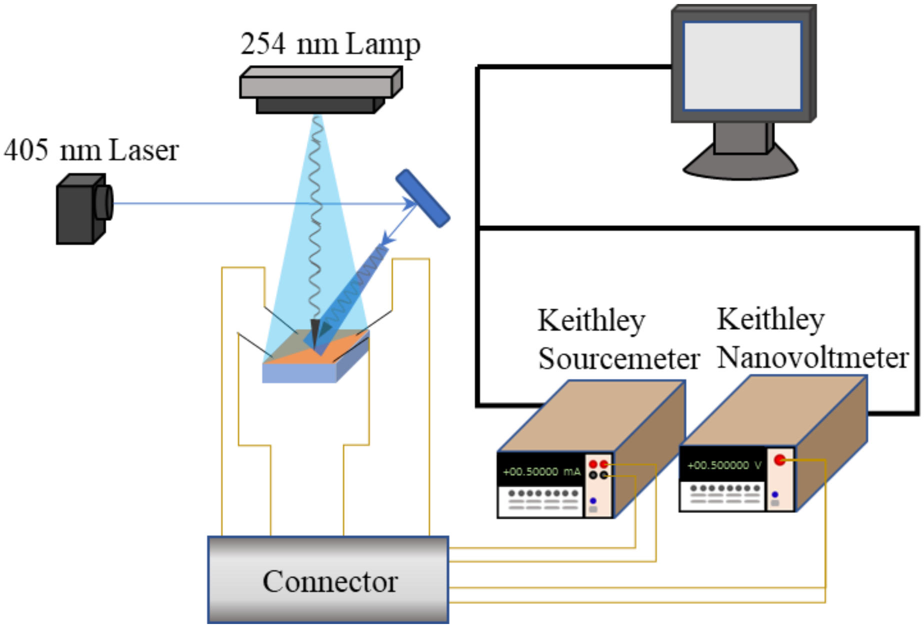

Figure 5.10: The van der Pauw probing system with the 405 nm diode laser and the 254 nm UV-C lamp orientations to probe the photoconductive response of each sample.

5.3.2 Resistivity Determination

The sample resistivity is a valuable piece of information in assessing the electronic properties of a thin film. The resistivity was determined from the van der Pauw method, coinciding with van der Pauw probe orientation.[100] This measurement method places the probe tips at the perimeter of the sample (ideally corners) where two probes are attached to a current source (Keithley 6220) and the other two are attached to a voltmeter (Keithley 2182a). The current source vs. voltmeter probe tip configuration is alternated as shown in Fig. 5.11.

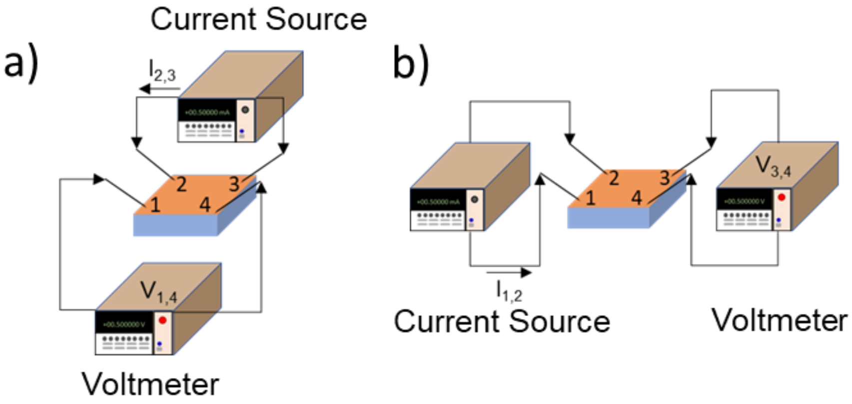

Figure 5.11: The probing configuration for samples with a) ”vertical” resistance calculation and b) “horizontal” resistance calculation.

All probe configurations, used in this study, are shown in Table 5.2. Here, the first two configurations in Table 5.2 are Fig 5.11a and Fig 5.11b respectively.

Table 5.2 Probe Configurations

Current Source Voltmeter
2,3→1,4
1,2→3,4
1,4→2,3
3,4→1,2

Using the supplied current and measured voltage, the resistance is determined for each orientation in Table 5.2. The multiple measurement orientations account for variability in resistance between two points along the perimeter improving the final resistivity calculation.[100]

Once the resistances for all configurations are determined, the following equation is used: [100]

$$e^{\left(-\frac{\pi d}{\rho}\right)\left(\frac{R_{1,4;2,3}+R_{2,3;1,4}}{2}\right)} + e^{\left(-\frac{\pi d}{\rho}\right)\left(\frac{R_{1,2;3,4}+R_{3,4;1,2}}{2}\right)} = 1 \tag{5.6}$$

where d is the film thickness, $R_{1,2;3,4}$ is the resistance for orientation 1,2→3,4 (the first two indices indicate the contacts connected to the current source and the last two indices are connected to the voltmeter), and ρ is the resistivity of the sample. Following the calculation in ref [100]:

$$\rho = \frac{\pi d}{\ln(2)} \frac{R_{horizontal} + R_{vertical}}{2} f \tag{5.7}$$

where,

$$R_{\ horizontal} = \frac{R_{1,2;3,4} + R_{3,4;1,2}}{2} \tag{5.8}$$

and,

$$R_{\ vertical} = \frac{R_{1,4;2,3} + R_{2,3;1,4}}{2} \tag{5.9}$$

here f is a form factor determined from:

$$Cosh[\frac{(R_{\ vertical}/R_{\ horizontal}) - 1}{(R_{\ vertical}/R_{\ horizontal}) + 1}\frac{ln[2]}{f}] = \frac{1}{2} \quad e^{ln[2]/f} \tag{5.10}$$

Then using the sheet resistance relationship $R_s = \frac{\rho}{d}$,

$$R_s = \frac{\pi}{\ln(2)}\frac{R_{\ horizontal}+R_{\ vertical}}{2}\ f. \tag{5.11}$$

Finally, we determine the resistance of the sample using the relationship:

$$R = R_s\frac{L}{W} \tag{5.12}$$

where L is the length of the sample and W is the width of the sample and R is the resistance of the sample where typical sample dimensions, sheet resistances, and resistivities are shown in Table D.1. Once the resistance of the sample is determined, the total photocurrent current is found from the measured photovoltage (Keithley 2182a) and the calculated resistance. Noting, the photovoltage is the potential difference in the plane of the VO_2 generated by the UV light incident upon the surface

5.3.3 Figures of Merit

Figures of merit are key parameters in demonstrating the performance, quality, and viability of a photodetector.[101] The figures of merit examined in this study are responsivity, external quantum efficiency (EQE), detectivity, and dark current density. Each film was evaluated with the 405 nm and 254 nm sources using the micro-probing system in a two probe arrangement to determine the figures of merit giving the representative performance of a low light UV detector as shown in Fig 5.12.

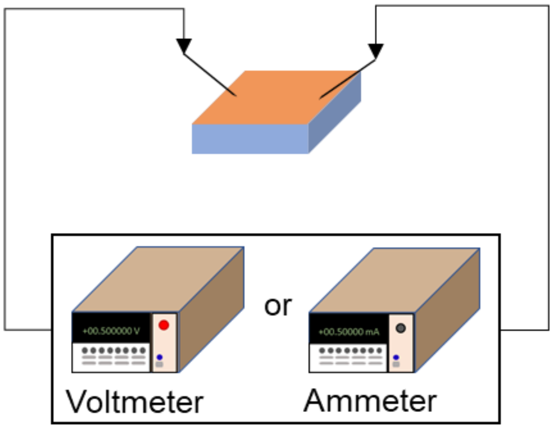

Figure 5.12: Example geometry for the photocurrent measurements using either a voltmeter or ammeter in the two-point arrangement.

To determine the figures of merit, the dark current (the residual current in a photodetector in the absence of light) is recorded and subtracted from the total illuminated current of each sample giving the actual photocurrent ΔI as shown in Fig 5.13.

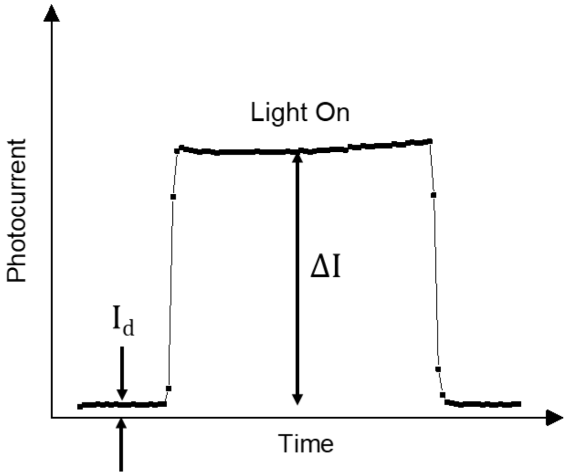

Figure 5.13: A sample photocurrent switching measurement with the actual photocurrent (ΔI) and the dark current (I_d) labeled.

Following the determination of ΔI, the EQE and responsivity (R_λ), for a given light power, is calculated using:[101–106]

$$EQE = \frac{hcR_\lambda}{e\lambda} \tag{5.13}$$

and

$$R_\lambda = \frac{\Delta I}{P} \tag{5.14}$$

where P is the total detected light power measured with a UV calibrated power meter (Thorlabs S120VC), λ is the excitation wavelength, h is Planck's constant, e is the electron charge and c is the speed of light in vacuum. The EQE and responsivity are supplemented with detectivity. This parameter provides a more complete picture of how engineering the detector affects its performance taking into account both the responsivity (R_λ) and the detector dark current (I_d):[101,103]

$$D^* = {A^{1/2} R_\lambda}\Big/{(2eI_d)^{1/2}} \tag{5.15}$$

where A is the total area of the film exposed to light. For this study, A is either the entire sample area for the Xe lamp or the area of the beam at the sample (~2 mm^2) for the diode laser due to the difference in illuminated area for the 254 nm Xe lamp versus the 405 nm diode laser. Finally, in low-power light detection, the dark current is a significant concern because it provides an effective minimum signal and noise level for the detector. [2,5,71,107,108] Thus, reducing the dark current density of a sample is desired in low-power light detection. The dark current density (J) is calculated using the measured dark current (I_d) and applying the following equation:

$$J = \frac{I_d}{A} \tag{5.16}$$

here A is the total light exposed area of the film.

CHAPTER 6

Structural and Photoelectric Properties of Epitaxially Grown Vanadium Dioxide Thin Films on c-Plane Sapphire and Titanium Dioxide

6.1 Introduction

As discussed in Section 4.1, vanadium dioxide is one of the most extensively studied strongly correlated materials that undergo a reversible first order transition from insulator ($T<T_c$) to metal ($T>T_c$) with an associated structural transition from the insulating monoclinic phase to the metallic rutile phase, where T_c is ~68°C in bulk.[41,46] An interesting property of VO_2 is its ability to undergo photoelectric conversion as discussed in Section 4.3.[80] Therefore, we sought to understand the photoelectric response by investigating the correlations between surface microstructure and photoelectric conversion in thin films deposited on different substrates to explore the potential parameter space.

The substrates used were c-plane sapphire (c-Al_2O_3) and TiO_2(001). The c-Al_2O_3 was chosen to optimize the VO_2 growth due its lattice similarity to bulk rutile VO_2(010) (shown in Fig. 6.1a) and its cost effectiveness. The TiO_2(001) was chosen for the reasons discussed in Sections 4.2 and 4.3, with the (001) plane of TiO_2 offering lattice parameters similar to bulk rutile VO_2(001) (shown in Fig 6.1b).

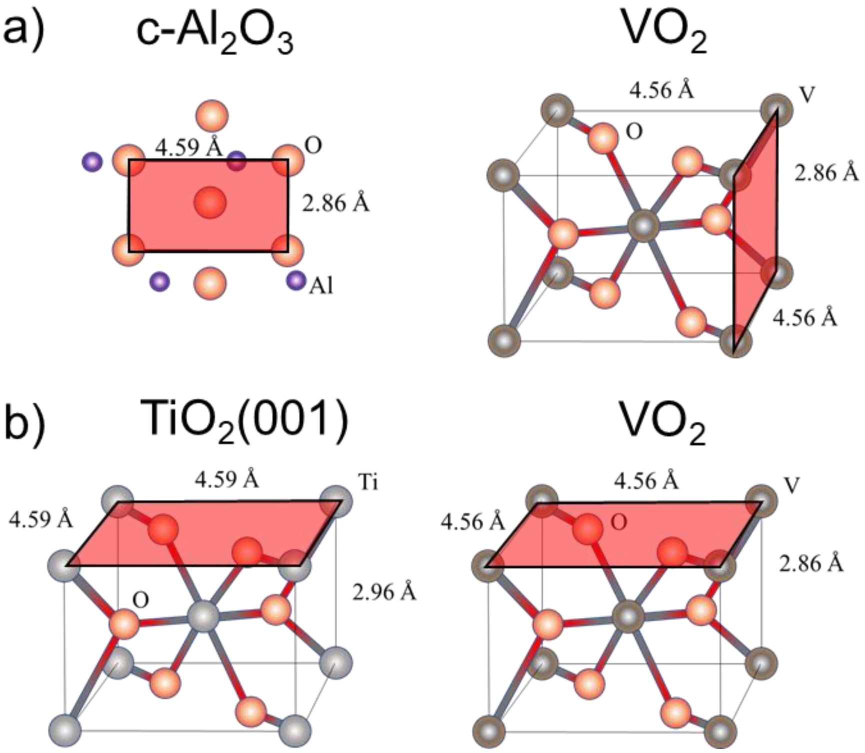

Figure 6.1: The substrate growth faces (left) for a) c-Al_2O_3 and b) TiO_2 with the corresponding VO_2 growth orientation highlighted (right)

The work presented in this chapter is published in reference [20].

6.2 Experimental Methods

6.2.1 Sample Growth

Epitaxial VO_2 films were sputtered-deposited on one side polished (1-sp) c-Al_2O_3(0001) and 1-sp TiO_2(001) substrates in an ultra high vacuum (UHV) deposition system with a base pressure ~$3.0\text{x}10^{-7}$ Torr range. The films were deposited via reactive D.C. pulsed magnetron sputtering (described in Section 5.1) with a vanadium target of 99.95% purity in a 93% Ar and 7% O_2 environment at 550^{o}C. Prior to deposition the substrates were annealed *in-situ* for 30 minutes at 600^{o}C to de-gas and recrystallize the top-most surface layers on each substrate. The target was then pre-sputtered for 20 min at 550^{o}C to clean the vanadium target and ensure stable deposition of VO_2, a shutter covers the substrate in this process to prevent deposition on the substrate. No bias was applied to the substrate at any point during the growth. Thin films exhibit ease in fabrication for integration into various complex integrated structures and hence offer good compatibility with current solid state device fabrication compared to alternative platforms such as quantum dots and nanowires.[103]

6.2.2 Structural and Photoelectric Characterization

The surface morphology of the samples was characterized via Nanotec Cervantes AFM instrument as described in Section 5.2.1. All images were flattened in the WSxM program and the images were processed via the root mean squared (RMS) analysis tool in the program. The RMS roughness gives an average estimate of the surface roughness of the film, and this quantitative description can be paired to the qualitative description obtained from RHEED.

The microstructure of the films was determined via XRD described in Section 5.2.2. XRR, described in Section 5.2.3, was used to calibrate the VO_2 growth rate. The VO_2 growth rate was found to be $\sim$5Å/min.

RHEED was used to determine the crystallographic structure of the film surface described in Section 5.2.4. This method allowed comparisons of various experimental diffraction patterns to simulated models of the VO_2 phases via RHEEDsim, described in Section 5.2.5, and allowed mapping the crystallographic changes through the thermally induced IMT.

The electrical and quantum efficiency information was determined with an MMR Technology Microprobe System (VTMP) described in Section 5.3.

6.3 Results

6.3.1 Crystal Analysis and Determination

All films are 30 nm thick and epitaxially grown via reactive DC magnetron sputtering on c-Al_2O_3 and TiO_2 as discussed in the experimental section. We assessed the initial microstructure of the films by carrying out X-Ray Diffraction (XRD) symmetric scans as shown in Fig. 1a). Upon examination of the 2θ scans, the peak location was consistent with the bulk location for the VO_2 grown on c-Al_2O_3, with a slight degree of strain toward the substrate peak as expected. Noting, the main peak location for the VO_2 grown on TiO_2 is consistent with previous reports for growth on this substrate.[61] Based on previous reports for VO_2 on TiO_2(001), the VO_2 peak location is strained toward the substrate peak by $\sim .5^o$, suggesting that the film contains a strained monoclinic phase.[61]

The mosaicity (the degree of crystallite misorientation) was determined for each sample finding a nominal degree of mosaicity $\sim 0.08^o$ for the sample grown on c-Al_2O_3 and $\sim .047^o$ for the sample grown on TiO_2.

6.3.2 RHEED Structural Analysis

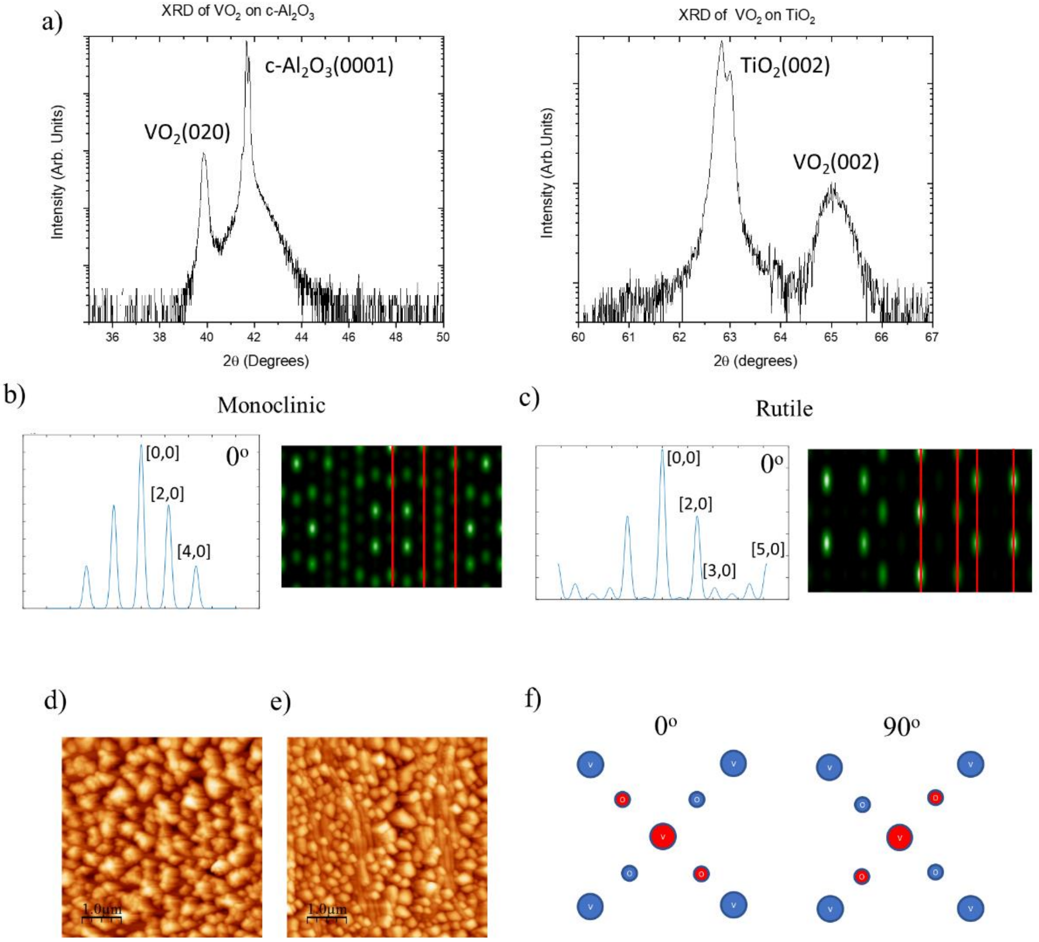

Figure 6.2: The experimental XRD, AFM, and simulated RHEED patterns of VO_2 on c-Al_2O_3 and TiO_2. a) The XRD 2θ scan for VO_2 on c-Al_2O_3(0001) and TiO_2(001) where the intensity scale in arbitrary units is log scaled. b) The simulated RHEED pattern of the 0° rotation for the monoclinic phase of VO_2 where the streak intensity patterns are recorded(left) and the simulated diagrams (right) with the in plane lattice planes are recorded for each. c) The simulated RHEED patterns of the 0° rotation for the rutile phase of VO_2 where the placement of the plots is the same as the previous monoclinic phase. d)The AFM image of the surface microstructure of VO_2 on c-Al_2O_3(0001) where the scale is 5.0μm x 5.0μm. e) The AFM image of the of the surface microstructure of VO_2 on TiO_2(001) where the scale is 5.0μm x 5.0μm. f) The orientations of the vanadium and oxygen atoms through the 0° and 90° rotations of one unit cell where the first two surface layers of atoms are shown in the c-direction where the red layer is displaced ~1.44 nm below the blue layer.

Table 6.1: Atomic Positions of VO$_2$(R)

Atom	X(Å)	Y(Å)	Z(Å)
Vanadium	0	0	0
	2.275	2.275	1.44
	1.38775	1.38775	0
	-1.38775	-1.38775	0
Oxygen	0.88725	3.66275	1.44
	3.66275	0.88725	1.44
	1.38775	1.38775	2.88
	-1.38775	-1.38775	2.88

Table 6.2: Atomic Positions of VO$_2$(M)

Atom	X(Å)	Y(Å)	Z(Å)
Vanadium	1.3915	5.2845	0.1345
	-1.3915	7.9945	2.5555
	-1.3915	-5.2845	-0.1345
	1.3915	-2.5745	2.8245
Oxygen 1	0.575	1.1382	1.076
	-0.575	3.8482	1.614
	-0.575	-1.1382	-1.076
	0.575	1.5718	3.766
Oxygen 2	2.2425	3.7398	1.5602
	-2.2425	6.4498	1.1298
	-2.2425	-3.7398	-1.5602
	2.2425	-1.0298	4.2502

Figure 6.2b-c shows the simulated Reflection High Energy Electron Diffraction (RHEED) patterns and streak diagrams expected for the bulk-like phases of VO$_2$ through the IMT.[98,109] As evidenced by Fig. 6.2b-c,f and Fig A1a-c, upon in-plane rotation of the sample with respect to the electron-beam, the diffraction pattern of the sample changes greatly due to the atomic positions of the vanadium and oxygen atoms on the lattice. The oxygen atoms play a distinct role in these diffraction patterns, as they appear to be the main contributors to streak intensity. Each in-plane rotation shows a large degree of variation in diffraction pattern, with a significant change expected for the monoclinic structure due to the canted angles of the oxygen atoms.[56]

The positions of the vanadium and oxygen atoms have been extensively studied both theoretically and experimentally for both phases across the IMT where space groups for the two phases of VO_2 across the IMT are $P4_2/mmm$(space group 136) for rutile and $P2_1/c$ (space group 14) for monoclinic and for our simulation atom positions were determined from these space groups as shown in Tables 6.1 and 6.2.[56] The rutile structure possesses greater in-plane symmetry than the monoclinic does. Thus, through each 90^o in-plane azimuthal rotation a repetition of patterns will occur with a clear differentiation in diffraction patterns expected along the 45^o rotation directions, and with differing patterns between 45^o and 135^o, depending upon whether the oxygen atoms are in-line with the main axis or rotated 90^o off axis. This in-plane azimuthal dependency illustrated in Fig. 6.2f and Fig. A1c shows first two layers of atoms account for the majority of the diffracted e^--beam intensity in the patterns.

The spotty nature of the simulated RHEED pattern (Fig. 6.2b,c and Fig A1a,b) is due to the fact that all surface atoms in the VO_2 structure not being in the same plane. The inherent surface roughness, shown in the AFM images (Fig. 6.2d,e) compounds the spottiness of the RHEED diffraction pattern.

When comparing the AFM images for both samples, the surface of VO_2 on c-Al_2O_3 has the largest average roughness, ~30nm, due to the larger spacing between terraces leading to a roughness on the order of the film thickness. In contrast, VO_2 on $TiO_2(001)$ exhibits smaller terrace spacing with each terrace sitting directly adjacent to its neighbor shown in Fig. 6.2e. This lack of separation between terraces yields a roughness ~13nm and an overall smoother film in comparison to VO_2 on c-$Al_2O_3(0001)$.

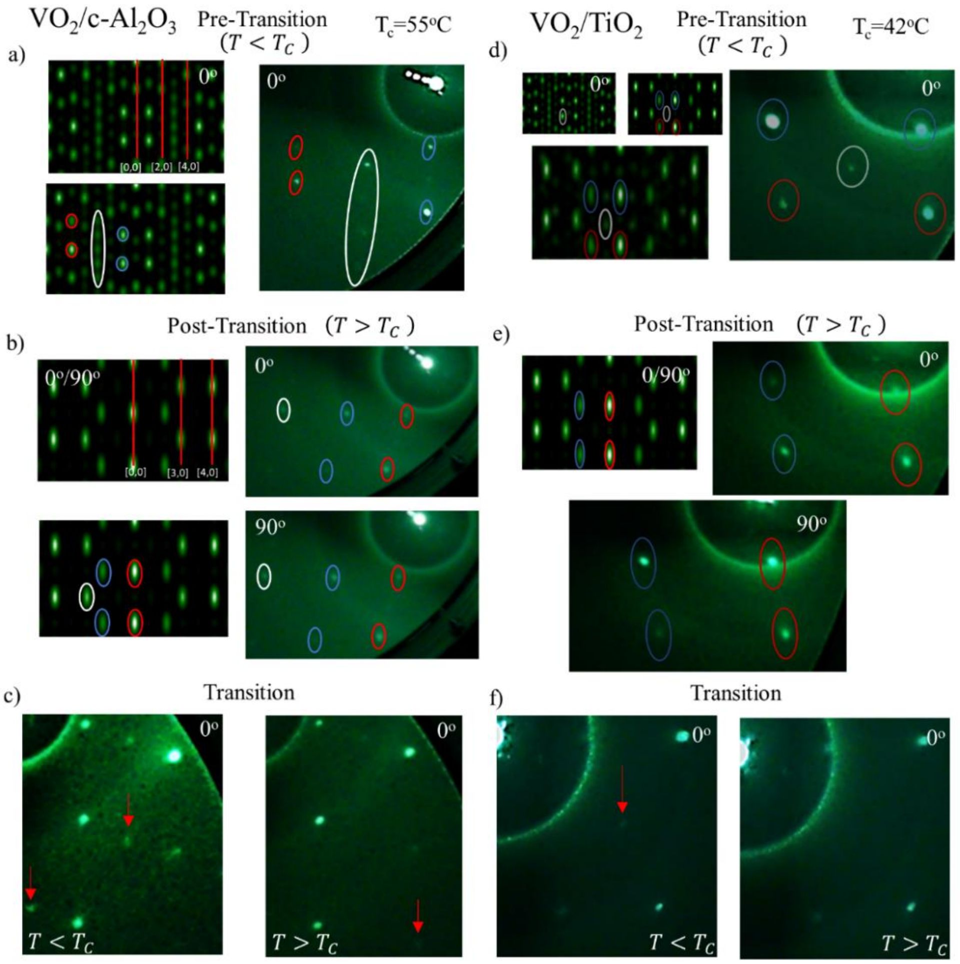

Figure 6.3: The simulated and experimentally determined RHEED patterns for VO_2 on c-$Al_2O_3(0001)$ and VO_2 on $TiO_2(001)$. *For VO_2 on c-$Al_2O_3(0001)$:* Simulated and experimental RHEED patterns of VO_2 azimuthal rotations and for the two phases. a) The left two images are simulations of the 0° rotation for the monoclinic phase of VO_2; the top image denotes the 2-D lattice planes for the streak patterns while the bottom image has streaks highlighted. The right image is the experimentally determined RHEED pattern the highlighted streaks correspond to the simulated image. This plot orientation is maintained for b) as well where the

simulated images are shown at left and experimental images at right. b) The $0^o/90^o$ rotation for the rutile phase of VO_2. c) The experimentally determined RHEED patterns for the 0^o degree rotation through the thermal IMT where the image on the left is prior to transition and the image on the right is post transition. *For VO_2 on $TiO_2(001)$:* d) The top leftmost two images are simulations of the 0^o rotation for the monoclinic phase (left) and rutile phase (right) of VO_2. The bottom left image is a superimposed image of both simulated images. The right image is the experimentally determined RHEED pattern for VO_2 on $TiO_2(001)$ where the highlighted streaks correspond to the simulated images. e) The left top image is the simulation and right top and bottom images experimental patterns for VO_2 grown on $TiO_2(001)$; the 0^o rotation is right and 90^o is bottom. f) The experimentally determined RHEED patterns for the 0^o degree rotation through the thermal IMT where the image on the left is prior to transition and the image on the right is post transition. (Note: All images have been rotated 45 degrees and the contrast has been increased for ease of streak identification)

Using the bulk VO_2 RHEED patterns predicted via simulation and the experimental RHEED patterns recorded from VO_2 grown on c-Al_2O_3, we observe numerous cases of pattern matching as well as streak spacing between the experimental and simulated RHEED patterns (shown in Fig. 6.3a and Fig. A2a) suggesting the simulations and the observed diffraction patterns for the monoclinic VO_2 phase are in good agreement. The samples were then brought to the rutile phase by thermally ramping to 100^oC, allowing for the VO_2 to undergo the full IMT which for this sample occurred at $\sim 55^oC$. The shift in transition temperature from bulk is likely due to the thin film character of sample, where factors like substrate and film lattice parameter mismatch are previously reported to play a key role for TiO_2.[61,110] The RHEED patterns for the transitioned sample , shown in Fig. 6.3b (right) and Fig. A2b (right), were compared to the simulations shown in Fig. 6.3b (left) and Fig. A2b (left). The rutile phase VO_2 streak patterns exhibit the same configurations as those predicted by the simulation. The AFM and XRD data combined with the RHEED experimental and simulation alignment asserts that the RHEED patterns observed in both the simulation and experiment are quite close to bulk-like crystalline VO_2 in both the monoclinic and rutile states.

Following the alignment of the experimental and simulated patterns, we examined the RHEED patterns through the transition to investigate the sample evolution in real time. The sample was thermally ramped in $5^{o}C$ increments from $25^{o}C$ to $100^{o}C$ recording the diffraction pattern after each increment. Upon reaching the critical temperature, we observe a marked change in the RHEED patterns. The critical temperature coincides with the disappearance of several peripheral streaks as well as a strengthening of the intensity of the main streaks creating a repeating "rectangular" pattern as designated in Fig. 6.3c. This change in diffraction pattern is likely due to the change in the atomic positions of the oxygen atoms when transitioning from the monoclinic to the rutile phase.

Finally, we compared the VO_2 simulations to a VO_2 sample grown on $TiO_2(001)$. Upon examination of the experimental VO_2 film prior transition Fig. 6.3d(right), we propose a plausible superposition of the simulated monoclinic and rutile phases with a greater emphasis on the streak locations of the rutile phase. Especially in the case of Fig. 6.3d (right), the non-transitioned locations have a distinctly rutile like pattern that suggests structural strain toward the rutile phase. Thus for Fig. 6.3d and Fig A2c, the monoclinic and the rutile simulations are interlaid, to make the microstructure more apparent, enabling fruitful comparison with experiment. The sample was then heated to 100^{o}C to allow for full transition, for this sample is ~42^{o}C, noting film substrate strain effects are known to play a key role in lowering the transition temperature.[61,110].

Once the sample was heated, we compared the simulations with the experimentally determined RHEED patterns. The patterns for the 0^o and the 90^o azimuth positions, shown in Fig. 6.3e(right/bottom), have several streaks well matched to the simulations. In comparison to the monoclinic phase, the center streak is missing but the four streaks that make up the “rectangular” shape pattern still persist with a slightly larger streak spacing than that of VO_2 on c-Al_2O_3. A slight slant in lattice location is visible in the 0^o and the 90^o azimuth directions likely due to the structural strain causing slight oxygen displacements in the VO_2 lattice.

We then examined the RHEED pattern through the transition to determine the structural changes from to the IMT. In order to do this, the sample was thermally ramped in 5^{o}C increments from 25^{o}C to 100^{o}C recording the diffraction pattern at each increment in agreement with the previous VO_2 on c-Al_2O_3 sample. Upon ramping through the temperature increments, there is a marked change at the critical temperature, observing the abrupt disappearance of the center streak in the rutile state that was apparent in the non-transitioned phase as shown by Fig. 6.3f. Due to the strong dependence of the streak patterns to the oxygen location and the larger degree of structural strain on the sample, this large pattern adjustment agrees with the expected strained monoclinic structure as previously discussed.

The structural characterization across the transition for these samples provides a suitable framework for subsequent characterization of the photoresponsivity of the samples described below.

6.3.3 Photocurrent Analysis

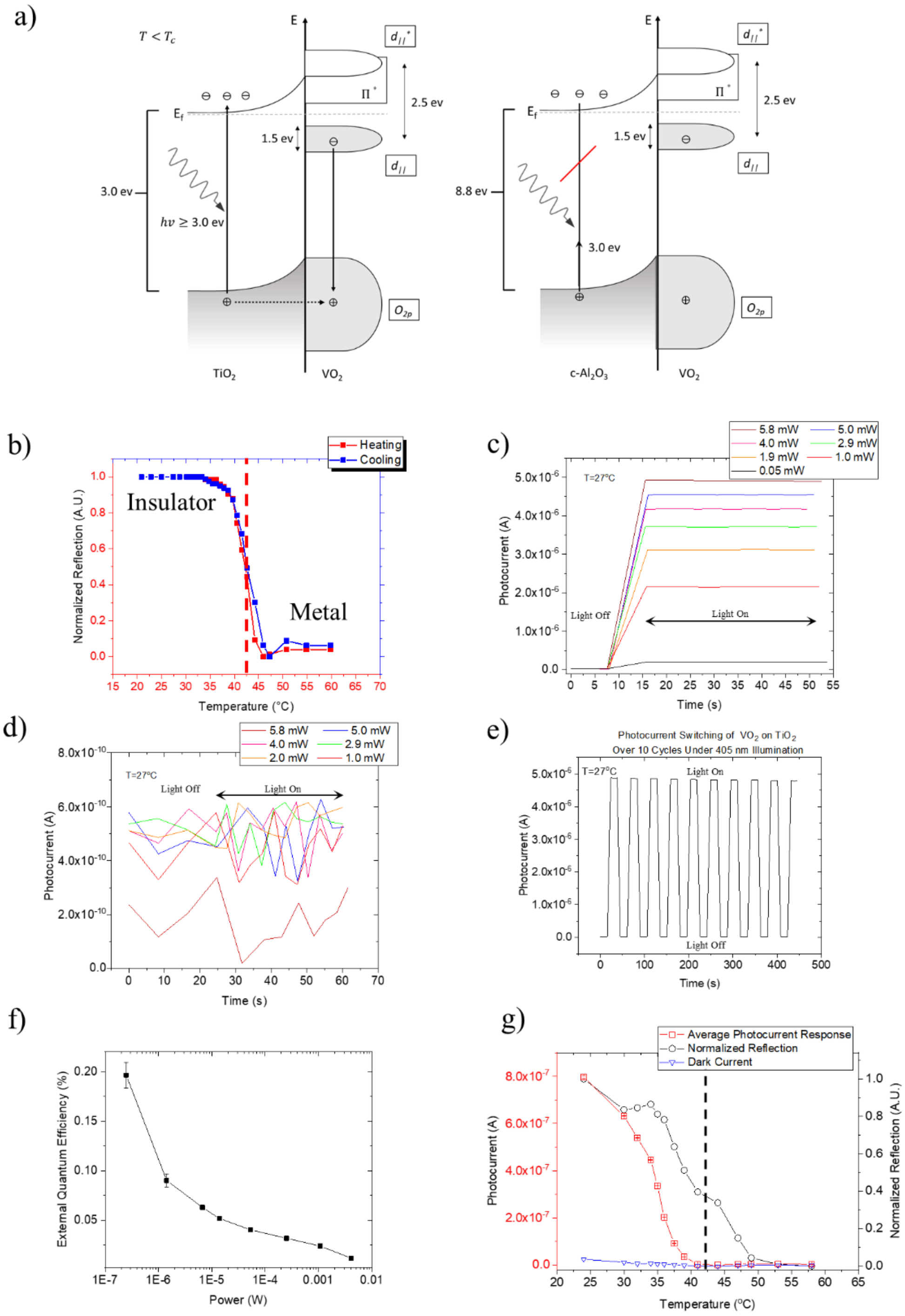

Figure 6.4: The electronic structure of VO_2 on TiO_2 and c-Al_2O_3 as well as studies of the photoelectric properties of VO_2 on TiO_2. a) Schematic band diagram of the hole transfer mechanism for VO_2 on TiO_2 and c-Al_2O_3 where the photon energy is shown for the VO_2 on TiO_2 as being sufficient to excite carriers in the TiO_2 layer and insufficient in the case of VO_2 on c-Al_2O_3. Where the hole transfer is designated

by the segmented line and the carrier movement is designated by the solid lines.[69,80] b) Reflectivity measurements with a 405 nm diode laser illuminating VO_2 deposited on TiO_2(001) as the sample underwent a thermally induced IMT via heating and subsequent cooling where the dashed line indicated transition temperature. c) The photocurrent switching of VO_2 on TiO_2(001) upon solely 405 nm illumination as the laser power was varied. The light was held on for 40 seconds post switching. (Note, the switch timing is from the delayed response time between software and equipment and not a property of the samples.) d) The same photocurrent switching measurement of VO_2 on c-Al_2O_3(0001) where the 405 nm laser power was varied. The light was held on for 40 seconds post switching. e) The photocurrent switching cycle for VO_2 on TiO_2(001) upon 405 nm illumination switching over 10 cycles. f) External quantum efficiency measurement for VO_2 on TiO_2 as varied with laser power g) The average photocurrent and optical response of VO_2 on TiO_2(001) as the sample was thermally ramped through the optical transition where the 405 nm laser power was 1 mW through the thermal ramping and the dashed line indicates transition the temperature.

The VO_2/TiO_2 band structure, shown in Fig. 6.4a, illustrates that the film/substrate heterostructure is a promising candidate for an efficient near-UV to deep UV photo-sensor as noted in Chapters 1 and 4. Thus, the VO_2 on TiO_2 sample is expected to display photohole injection upon illumination as described in Section 4.3.

We began by probing the optical response of VO_2 on TiO_2 through the thermal IMT as shown in Fig. 6.4b. In this optical transition, a decrease in reflection corresponds to a decrease in resistivity. We then investigated the photocurrent for each sample to determine if solely the 405 nm illumination could excite carriers in the TiO_2 substrate and undergo photohole injection, as shown in Fig. 6.4a. The 405 nm laser does produce a clear photocurrent, shown in Fig. 6.4c, with its magnitude correlated with the laser power. A reliable photocurrent switch is additionally observed through multiple on/off cycles, shown in Fig. 6.4e, demonstrating the photocurrent switch survivability. Additionally, the quantum efficiency of the TiO_2 samples examined for various laser powers is shown in Fig. 6.4f. The external quantum efficiency was calculated via Eq. 5.13 as discussed in section 5.3.3:

$$EQE = \frac{hc\Delta I}{e\lambda P} \tag{5.13}$$

Using Eq. 5.13, we found that as the laser power decreased the VO_2 quantum efficiency exhibited a 2000% increase between the highest and lowest light powers, shown in Fig. 6.4f. Additionally, the photocurrent of VO_2 on c-Al_2O_3(0001) was measured under 405 nm illumination. However, the insufficient photon energy of the 405 nm light could not excite carriers across the ~8.8 eV[111] band gap in c-Al_2O_3(0001),, resulting in no photocurrent in the VO_2 film shown in Fig. 6.4d.

Finally, we examine the photocurrent production with heating and correlate the transition with the photocurrent. As shown in Fig. 6.4g, we observe that as the sample heats, a marked reduction in the photocurrent occurs by continuously approaching zero until eventually reaching zero. This reduction in photocurrent coincides with the IMT where the collapse of the VO_2 band gap results in the metallic phase restricting the movement of carriers to the photoinjected holes. Here our reflected optical signal tracks the phase change optically through the transition, where a reduction in optical response is correlated with the phase change from monoclinic to rutile. However, we note that the photocurrent reduces to zero before the optical transition is complete. One possible explanation follows from earlier descriptions of the nucleation of the metallic phase upon heating where localized puddles of metallic phase VO_2 become so prevalent such that the photocurrent is reduced to zero before the film fully transitions to the metallic phase.[41,48,112]

Thus, local “puddle” formation reduces the effective carrier movement before the sample has fully transitioned such that a global surface current is no longer possible reducing the photocurrent to zero although the surface of the sample is not fully phase transitioned. This “puddling” across the thermally induced IMT in VO_2 has been extensively studied and reported.[41,48,112]

6.4 Conclusion

We have shown that epitaxially grown VO_2 on both c-Al_2O_3 and $TiO_2(001)$ by pulsed DC sputtering exhibit good crystal character and a low degree of mosaicity. They also exhibit a characteristic surface morphology with terracing plateaus due to strain. We have been able to accurately compare simulations of VO_2 RHEED patterns consistent with our experimental data on the films that we have studied. We have also presented a first of its kind RHEED temperature transition analysis for VO_2 in which we were able to analyze and conceptualize the structural phase transition of VO_2 on both c-Al_2O_3 and TiO_2(001), evidencing the dynamical changes that VO_2 undergoes through its critical transition temperature.

We also determined the photocurrent switching of VO_2 on TiO_2(001) and c-Al_2O_3(0001) at 405 nm and saw a stark reduction in photocurrent for VO_2 grown on c-Al_2O_3(0001) as compared to VO_2 on TiO_2(001). This reduction in photocurrent is likely a product of the high resistivity and large substrate band gap as well as VO_2 films with much rougher surface, where roughness also contributes to scattering effects resulting in lower carrier efficiency thus reducing the photocurrent. We show a marked increase in the quantum efficiency of the VO_2 on TiO_2 with decreasing laser power seeing as large as a 2000% difference in quantum efficiency from 4.6 mW to 250nW laser power. Finally, we show how the IMT influences the produced photocurrent under illumination determining that as the VO_2 transitions through the IMT to the metallic state there is a significant reduction of produced photocurrent.

CHAPTER 7

Intrinsic Anomalous Scaling of Epitaxial Vanadium Dioxide Thin Films on Titanium Dioxide

7.1 Introduction

We present our studies on growth and evolution of the surface morphology and microstructure of VO_2 thin films grown on TiO_2(002) substrates. VO_2 is one of the most extensively studied materials in the correlated electron family with an IMT as discussed in Section 4.1. The IMT can be induced thermally[37,39–41,50], electrically[62,112], optically[42–45,110,113–116], etc. making VO_2 a material of significant interest for many applications by using its controllable variable resistivity, optical properties, remarkable switching capabilities, and UV photocurrent response. [20,80]

The dynamic surface evolution and resulting changes to microstructure and surface morphology during thin film growth is critical for understanding and tailoring properties of technological relevance, e.g. increasing and optimizing electrical, optical, and photocurrent responses.[117,118] Thus, we examined the fractal like growth symmetries of a film and the resulting growth front scale invariance through scaling relationships, such as Family Vicsek scaling, to understand the technologically relevant properties of a film.[117,119–121]

7.1.1 Fractals and Surface Scaling

In 1975, B. Mandelbrot defined a fractal as “a rough or fragmented geometric shape that can be split into parts, each of which is a reduced size copy of the whole.” This definition opened discussion for two fractal types: self-similar and self-affine. Self-similarity is an object which is exactly or approximately similar to parts of itself. This is the case for fractals such as the Koch snowflake shown in Fig 7.1.[122,123] A way to visualize this self-similarity is if one takes a self-similar fractal and magnifies to a section, there will exist a smaller piece of the fractal that is exactly or approximately similar to the larger piece. This invariant phenomenon is called scale invariance. Alternatively, self-affinity is an object where feature scaling differs in the x, y, and z directions. Thus, a transformation is applied for a section to be exactly similar to the original larger object. This process is evident in fractals like the Barnsley Fern, shown in Fig 7.1. Here, a transformation must be applied to get one boxed piece of the fern to match the other.[123,124] In naturally occurring fractals, self-affinity is more common than self-similarity.[123,124]

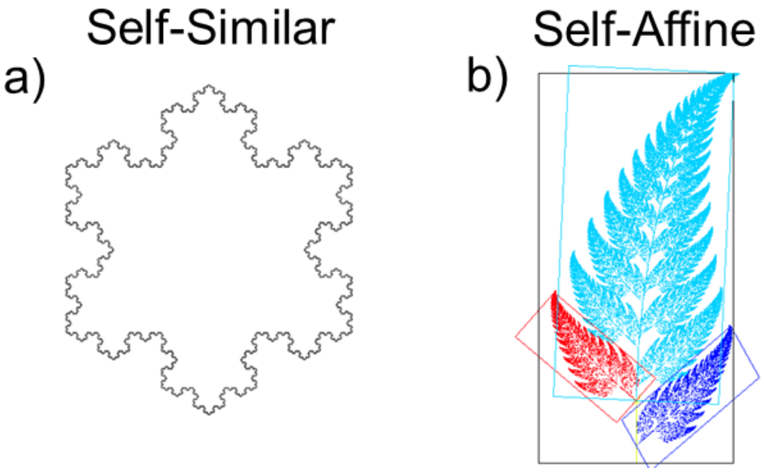

Figure 7.1: a) The self-similar Koch snowflake. b) The self-affine Barnsley fern where fern pieces are boxed to demonstrate the separate scaling relationships. (Images adapted from Wikipedia)

Self-affinity is common in many thin films. This persistence of self-affinity in thin films led Family and Vicsek to propose a scaling ansatz (Eq 7.3) presupposing a surface arising from a non-equilibrium process is scale invariant due to the stochastic processes that drive surface evolution. This ansatz gives an initial method to evaluate if self-affinity is present throughout film growth.

7.1.2 Family-Vicsek Scaling

As described in Chapter 2, several mechanisms drive surface evolution during thin film growth: (i) direct addition of atoms on the growing surface, (ii) removal of atoms, and (iii) diffusive mass transport of atoms. Most behavior in surface evolution can be analyzed with the Kardar-Parsi-Zhang (KPZ) equation:[125]

$$\frac{\partial h(\vec{r},t)}{\partial t} = v\nabla^2 h(\vec{r},t) + \frac{\lambda}{2}|h(\vec{r},t)|^2 + \eta \tag{7.1}$$

where $h(\vec{r},t)$ is the temporal change in surface height at place $\vec{r}$ and t is deposition time (or in the case of this study sample thickness), v accounts for the surface tension, λ is an "excess velocity" in the growth, and η is the white Gaussian noise.[126] Thus, from the stochastic approach to film growth, we begin the evaluation of the surface by examining the global interfacial width $w(L,t)$, defined as:

$$w(L,t) = \langle \overline{\left[h(\vec{r},t) - \overline{h(\vec{r},t)}\right]^2} \rangle^{1/2} \tag{7.2}$$

where h is the surface height (as in the KPZ equation), t is deposition time (in our case directly proportional to film thickness), $\langle \ldots \rangle$ is the average over multiple realizations, and the over bar denotes an average over all $\vec{r}$ in a system of size L. For our study, $w(L,t)$ is the root-mean-square (RMS) surface roughness averaged over the entire Atomic Force Microscopy (AFM) scan length. Applying the Family-Vicsek ansatz:[126–129]

$$w(L,t) = t^{\beta} f\left(\frac{L}{t^{\beta/\alpha}}\right), \tag{7.3}$$

the function $f(u)$ behaves as:

$$f(u) \sim \begin{cases} u^{\alpha} & \text{if } u \ll 1 \\ const & \text{if } u \gg 1 \end{cases} \tag{7.4}$$

where L is the system of size, α is global roughness exponent, β is the growth exponent, and the $z = \alpha/\beta$ is the dynamic scaling exponent. From these relationships, it is determined that for small (short) L $\left(\text{i.e.}\, L \ll t^{\beta/\alpha}\right)$, $w(L,t)$ is independent of deposition time thus scaling as L^{α}, and for large (long) L $\left(\text{i.e.}\, L \gg t^{\beta/\alpha}\right)$, $w(L,t)$ is found to scale as t^{β}.[130–132] These scaling relationships allow us to individually determine: the global roughness exponent (α), the growth exponent (β), and the dynamic scaling exponent $(z = \alpha/\beta)$.[127,129] Additionally, we define the limit of the crossover region $\left(\text{i.e.}\, L \cong t^{\beta/\alpha}\right)$ as the correlation length (ξ), scaling as $\xi \sim t^{\beta/\alpha}$.[129,130,133]

For many surfaces, Family Vicsek scaling is insufficient to adequately determine the surface scaling behavior. [128–132,134] In such cases, one set of scaling exponents is not enough to describe the scaling behavior, necessitating an additional set. This additional set of scaling exponents follows from the anomalous scaling ansatz[129,130,132]:

$$w(r,t) = r^{\alpha} f_A\left(\frac{r}{t^{\beta/\alpha}}\right) \tag{7.5}$$

where:

$$f_A(u) \sim \begin{cases} u^{\alpha_{loc}-\alpha} & \text{if } u \ll 1 \\ u^{-\alpha} & \text{if } u \gg 1 \end{cases} \tag{7.6}$$

resulting in:

$$w(r,t) \sim \begin{cases} t^{\beta^*} r^{\alpha_{loc}}, & if\ r \ll t^{\beta/\alpha} \ll L \\ t^{\beta}, & if\ \ r \gg t^{\beta/\alpha} \end{cases} \tag{7.7}$$

where α_{loc} is the local roughness exponent and β^* is the anomalous growth exponent. With these additional scaling exponents, we retrieve the following relationship $\beta - \beta_{loc} = (\alpha - \alpha_{loc})/z$ employing $\beta^* = \beta - \beta_{loc}$.[129,130]

Finally, one additional independent scaling exponent, the spectral roughness exponent (α_s), is required to finalize the classification of surface.[129–132] Using the power spectral density (PSD) of each scan and making the assumption that the PSD of the surface defines the structure factor:

$$S(k,t) = \langle \hat{h}(k,t)\hat{h}(-k,t) \rangle \tag{7.8}$$

where $\hat{h}$ is the Fourier transform of the surface height function, *k* is the spatial frequency, and *t* is deposition time (in our case film thickness) it follows that S(k,t) takes the form[129,130]:

$$S(k,t) \sim \begin{cases} t^{(2\alpha+2)/z}, & if\ k \ll k_c \\ k^{-(2\alpha_s+2)} t^{2(\alpha-\alpha_s)/z}, & if\ k \gg k_c \end{cases} \tag{7.9}$$

and $k_c \sim 1/\xi$. Therefore in the region $k \gg k_c$, we determine the spectral roughness exponent (α_s) from the PSD.[129,130,132]

Using the full series of scaling exponents, we classify the known modes of surface scaling into one of the following scaling classes:[129,130,133]

Table 7.1: Scaling Classes

Family Vicsek	*Intrinsic*	*Super Rough*	*New Class*
$\alpha_s = \alpha$	$\alpha_s \neq \alpha$	$\alpha_s = \alpha$	$\alpha_s \neq \alpha$
$[\alpha_{loc} = \alpha_s]$		$[\alpha_{loc} = 1]$	
$[\alpha_s < 1]$		$[\alpha_s > 1]$	

**The bracketed items are shared conditions

These scaling classes denote the sets of scaling parameters that remain consistent for all models within a class, thus the scaling behavior can be determined for any scale (i.e. any growth time/thickness). Here, intrinsic, super rough, and new scaling classes are anomalous forms of scaling.[129,130,133] The difference between the intrinsic and new class is that for the intrinsic class the local roughness exponent (α_{loc}) and spectral roughness exponent (α_s) scale equivalently; however, in the new class, the local roughness exponent and the spectral roughness exponent scale separately with the spectral roughness exponent scaling independently of the other exponents. Thus, the new class of scaling is detected by the scaling of the spectral roughness exponent.[130]

The information presented in this study is published in Ref. [135].

7.2 Methods

7.2.1 Sample Growth

The VO_2 was grown on $TiO_2(001)$ as described by Section 6.2.1.

7.2.2 Structural Characterization

The structure of the films was evaluated with AFM, XRD, RHEED, and XRR as described in 6.2.2.

7.3 Results

7.3.1 VO$_2$ on TiO$_2$ Surface Morphology

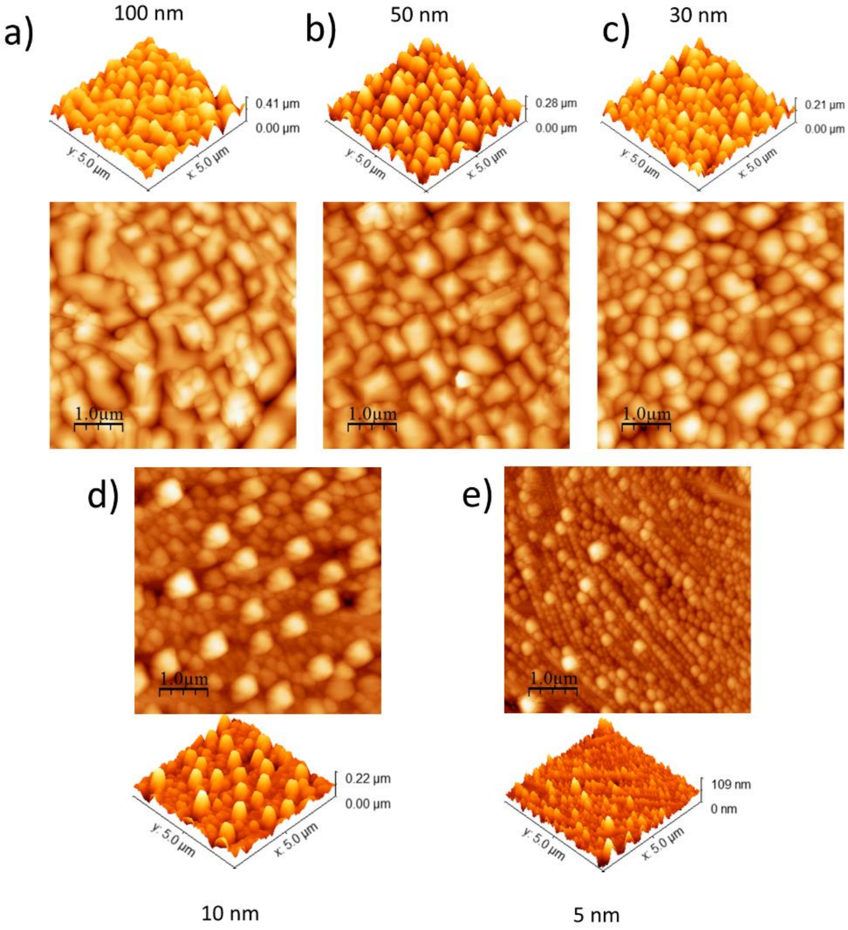

Figure 7.2: Shown: 5µm x 5µm AFM images of VO$_2$ on TiO$_2$(002). In the top row we see the 3D representation (top) of the surface and the 2D representation of the surface (bottom) for the a) 100nm, b) 50nm, c) 30nm thick samples. In the bottom row, we see the 2D representation (top) and the 3D representation (bottom) for the d) 10nm, and e) 5nm thick samples.

Figure 7.2 shows the typical surface morphology of various VO_2 films grown on $TiO_2(002)$. These samples reveal the surface evolution of single crystalline VO_2 films as the deposition time increased and therefore the film thickness, with an average growth rate of 0.5nm/min. By increasing film thickness, the characteristic “island” structures at the surface exhibit coarsening and eventually coalescence. This coarsening is evident in Fig 7.2a-c, we can see the surface structures become enlarged and eventually begin to coalesce as shown in fig 7.2a. However, in the thinner samples, there are several pronounced nucleation zones with smaller and smoother surface features between other nucleation zones. This is especially apparent in Fig 7.2d where 3D nucleation zones dominate the surface while smoother surfaces with smaller features make up the remaining space. Thus, we describe the film evolution with the following structure: for the thinnest samples Fig 7.2d,e there is a thin surface dominated by large nucleation zones. As the film thickness increases these 3D nucleation zones begin to fully dominate the surface in Fig 7.2c, these zones continue to evolve Fig 7.2c-a and finally form the larger more continuous features in Fig 7.2a. After documenting the evolution of the film surface with AFM, we used these images to determine the scaling exponents and establish the scaling class of the films.

7.3.2. Scaling Exponents Determination

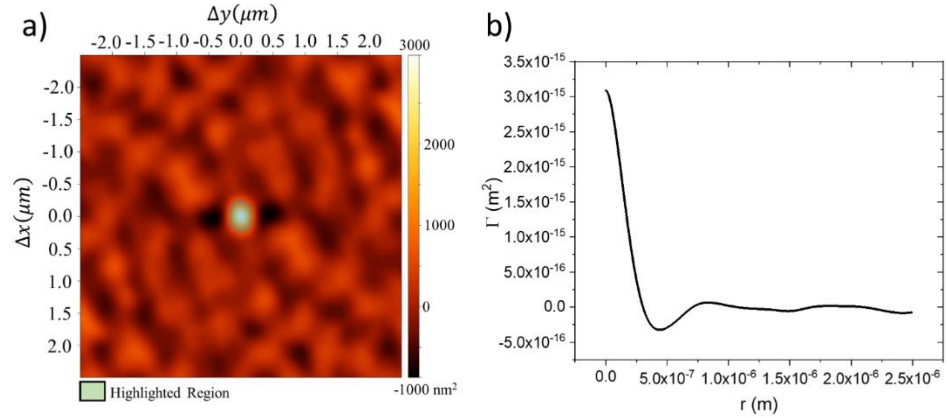

Figure 7.3: a) The 2-dimensional radial autocorrelation of the 100 nm thick sample. The highlighted region is the 2D autocorrelation within the correlation length of the sample. b) The angularly averaged 2-D autocorrelation function (radial autocorrelation function) of the 100 nm sample where Γ(r) is the radial autocorrelation function and r is the radial distance from the center of the surface image.

The dynamic exponent z was approximated using the autocorrelation function:

$$\Gamma(\Delta x, \Delta y) = \lim_{S \to \infty} \frac{1}{S} \iint_S \zeta(x_1, y_1)\zeta(x_1 - \Delta x, y_1 - \Delta y) dx_1 dy_1 \tag{7.10}$$

where $\zeta(x, y)$ is a random function corresponding to points (x_1, y_1) and (x_2, y_2) noting $\Delta x = x_2 - x_1$ and $\Delta y = y_2 - y_1$.[136] An example of this 2-dimensional autocorrelation surface is shown in Fig 7.3a. For each sample, the radial autocorrelation function (i.e. the angularly averaged two-dimensional autocorrelation function) was used:

$$\Gamma(r) = \int_0^{2\pi} W\big(r\,cos(\varphi), r\,sin(\varphi)\big) d\varphi \tag{7.11}$$

where $W(\ldots)$ is the radial 2-dimensional probability density shown in Fig. 7.3b.[136] Noting, that for the autocorrelation function, all values below zero are radial distances that have no physical correlation and the small oscillations about zero in figure 7.3b do not contribute to the correlation length. Typical autocorrelation is often assumed to have a Gaussian shape, thus we used the following Gaussian relation: $\sigma^2 \exp\left(-\frac{r^2}{\xi^2}\right)$ where $\sigma^2$is the RMS deviation of heights, and ξ is the correlation length.[136] We used this fit to find ξ and from the relationship $\xi{\sim}t^{1/z}$ determined the dynamic scaling exponent to be

$1/z = 0.19 \pm 0.05$ as shown in Fig 7.4a).

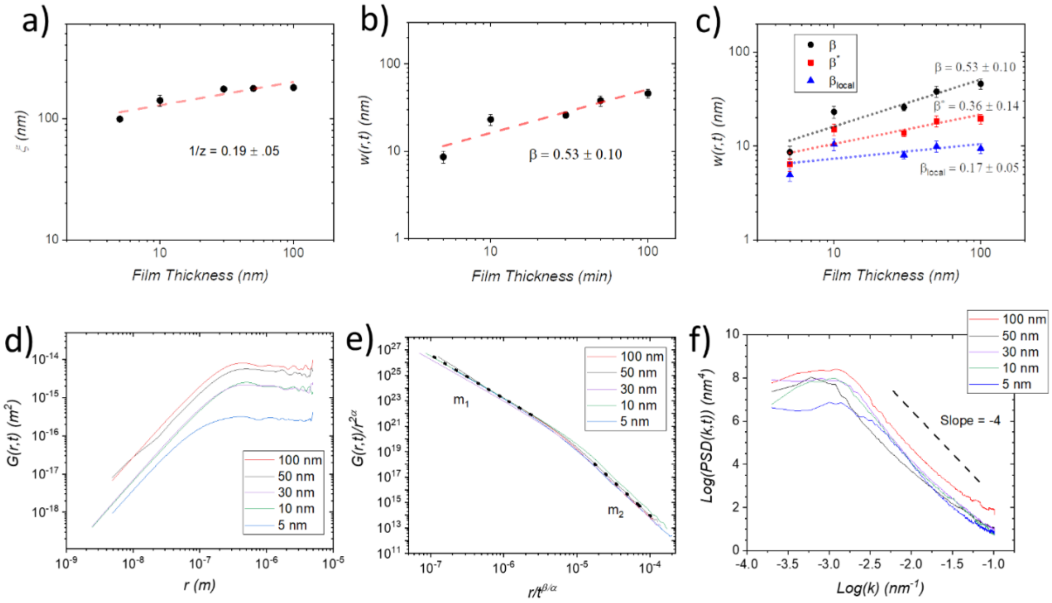

Figure 7.4: a) The plot of the correlation length (ξ) and b) interfacial width (w(r,t)) where dashed lines correspond to the slope values notated in the graph. c) The plot of the interfacial width (w(r,t)) for β, β^*, and β_{loc} and dashed lines correspond to the values of the slopes noted in the graph. d) The plot of the height-height correlation function G(r,t) for the various film thicknesses. e) The plot of $G(r,t)/r^{2\alpha}$ versus $r/t^{\beta/\alpha}$ for the various thicknesses illustrating the collapse of the height-height correlation function. The slopes m_1 and m_2 shown with dotted lines. f) The plot of the logarithm of the power spectral density (PSD) versus the logarithm of the wave number (k). The dotted line for large values of *k* is a guide to the eye.

The global interfacial width was determined from the RMS roughness of the surface for a lateral length L (the lateral scan size for each sample), and the three lateral lengths used were 5000nm, 2500nm, and 1000nm. The relation $w(L,t)\sim t^{\beta}$ for $L \gg \xi$ was used for plotting the interfacial length vs film thickness as shown in fig 7.4b) and we find that $\beta = 0.53 \pm 0.10$ which is within the random deposition limit of stochastic roughening ($\beta = 0.5$).[131] Once both β and z were found the global roughness exponent (α) was determined to be $\alpha = 2.76 \pm 0.19$ with the following relation $\alpha = \beta z$.

We used a height-height correlation function $G(r,t)$ defined as $G(r,t) = \langle\overline{[h(\vec{r}_2,t) - h(\vec{r}_1,t)]^2}\rangle$ to determine the remaining scaling exponents noting correlations over a distance l are represented by $G(r,t) = \langle\overline{[h(\vec{r}+l,t) - h(\vec{r},t)]^2}\rangle$. [129–131,134] This height-height correlation function was applied to each thickness for scan lengths of 5000nm, 2500nm, and 1000nm respectively. For each film presented in fig 7.4d), $G(r,t)$ obeys a power law dependence on r for short length scales and saturates for large length scales. Additionally, there is a general trend upward for the curves as thickness increases. This phenomenon has been observed in other cases following anomalous scaling. [131,134] We note that this generalized thickness dependence is contrary to the typical scaling described by the Family Vicsek model where $G(r,t) \sim r^{2\alpha}$ for $r \ll \xi$ and approximates a constant value as $r \gg \xi$. Thus the curves in fig 7.4d) suggest an anomalous scaling model following the relationship $G(r,t) \sim [w(r,t)]^2$, finding the scaling relationship in terms of the anomalous scaling model[129–131]:

$$G(r,t) \sim \begin{cases} t^{2\beta^*} r^{2\alpha_{loc}}, & if\ r \ll \xi \\ t^{2\beta}, & if\ r \gg \xi \end{cases} \tag{7.12}$$

Thus, using the height-height correlation functions we find the values of α_{loc} and β^* fitting the region $r \ll \xi$ with a least squares linear fit for each scan length, yielding an average local roughness exponent $\alpha_{loc} = 0.88 \pm .05$ and then employing the relationship $\beta - \beta_{loc} = (\alpha - \alpha_{loc})/z$ to find $\beta_{loc} = 0.17 \pm 0.05$. Finally, by employing $\beta^* = \beta - \beta_{loc}$ the anomalous scaling parameter (β^*) was found to be $\beta^* = 0.36 \pm 0.15$ demonstrating that both the local interfacial width and the local roughness exponent increase less rapidly than their global counterparts.[137] This relationship is shown in fig 7.4c) noting the continually decreasing slope from β to β_{loc}.

To verify the consistency of these scaling exponents, we collapsed the height-height correlation using eq. 7.12) and plotted $G(r,t)/r^{2\alpha}$ versus $r/t^{\beta/\alpha}$ (Fig 7.4e).[129–131,134] As designated in fig 7.4e) the slopes for each section of the curve should follow the following relationships: $m_1 = -2(\alpha - \alpha_{loc})$ and $m_2 = -2\alpha$. [129–131,134] The average slopes found for all scan lengths is $m_1 = -3.59$ and $m_2 = -5.39$ and we note that $m_1 \neq 0$ reaffirms our previous finding of $\alpha \neq \alpha_{loc}$. With the application of the conditions of m_1 and m_2, we further find that $\alpha = 2.69 \pm .02$ and $\alpha_{loc} = 0.90 \pm .04$ consistent with our previous determination of $\alpha = 2.76$ and $\alpha_{loc} = 0.88$ from the slope of $G(r,t)$ vs r curves in $r \ll \xi$.

Finally, we evaluated the log-log plot of the power spectral density (PSD) (as designated in eq 7.9) by linearly fitting the PSD in the large-*k* regime observed in fig 7.4f). The average spectral exponent was found to be $\alpha_s = 0.92 \pm 0.07$ matching the local roughening exponent $\alpha_{loc} = 0.90 \pm 0.04$, however it does not match the global roughening exponent $\alpha = 2.69 \pm .02$. Thus, we determine the relationship $\alpha_s = \alpha_{loc} \neq \alpha$.

With all the scaling parameters for the surface known, it is now possible to establish the scaling class of the thin film growth. Thus from $\alpha = 2.69 \pm 0.02$, $\alpha_{loc} = 0.90 \pm 0.04$, $\alpha_s = 0.92 \pm 0.07$, $\beta = 0.53 \pm 0.10$, $\beta_{loc} = 0.17 \pm 0.05$, and $1/z = 0.19 \pm 0.07$ as shown in Table 7.2 and upon comparison to Table 7.1, we find these scaling exponents occupy the intrinsic anomalous scaling class as $\alpha_s < 1$, $\alpha_s = \alpha_{loc}$, and $\alpha_s \neq \alpha$.[129,130,138]

Table 7.2: Scaling Exponents

α	α_{loc}	α_s	β	β_{loc}	$1/z$
2.69 ± 0.02	0.90 ± 0.04	0.92 ± 0.07	0.53 ± 0.10	0.17 ± 0.05	0.19 ± 0.07

7.3.3. Intrinsic Anomalous Scaling and Nonlocal Growth Effects

It is necessary to note that intrinsic anomalous scaling in thin films has been reported to be restricted in local growth modes by symmetries and local conservation laws. [139,140] This restriction requires disordered and/or nonlocal effects to exist for such scaling to occur.[139,140] For our study, we will focus on nonlocal growth effects arising from i) reactive sputter deposition and ii) substrate-film interfacial strain effects. [134,140–142] In case i), it has been previously reported that surfaces grown via reactive sputter deposition exhibit nonlocal growth effects.[134] Thus it is expected that reactive sputter deposition of VO_2 as done in this study would potentially introduce nonlocal effects during growth as well. In case ii), adjustments of the adatom mobility and the reduction of carrier mobility from substrate-film interfacial strain and associated grain boundaries have been previously found to result in nonlocal effects causing intrinsic anomalous scaling.[140–142] In this study, the lattice mismatch between the VO_2 film and the TiO_2 substrate results in substrate-film strain leading to crystal mosaicity and grain boundary formation in the film with an average mosaicity of 0.43^o and grain size of 16 nm found for the films from XRD scans. Therefore, it is reasonable to assume that strain at grain boundaries would act as diffusion barriers inhibiting adatom movement across the boundaries. Thus we conclude that nonlocal effects are likely present during the growth of the samples, in this study, resulting in the intrinsic anomalous scaling observed.[129,134,139]

7.4. Conclusion

We have investigated the evolution of the VO_2 thin film epitaxial growth on $TiO_2(002)$ substrates by examining the dynamic scaling relationships at several film thicknesses. We show that as the VO_2 film thickens it displays large nucleation zones that coarsen and coalesce with further growth. By extracting a series of growth exponents to evaluate the surface structure, roughening, and morphology of the films, we determined the following scaling exponents: $\alpha = 2.69 \pm 0.02$, $\alpha_{loc} = 0.90 \pm 0.04$, $\alpha_s = 0.92 \pm 0.07$, $\beta = 0.53 \pm 0.10$, $\beta_{loc} = 0.17 \pm 0.05$, and $1/z = 0.19 \pm 0.05$. These exponents correspond to the intrinsic anomalous scaling class, suggesting that nonlocal effects play a significant role during the evolution of the film. Thus, the intrinsically anomalous scaling observed likely arises from a combination of reactive sputter deposition and interfacial strain effects between the film and substrate. Our studies can aid in the determination of optimal film thickness for specific applications of epitaxial VO_2 thin films on TiO_2(002).

CHAPTER 8

Growth and Characterization of Vanadium Dioxide / Niobium Doped Titanium Dioxide Heterostructures for Ultraviolet Detection.

8.1 Introduction

As discussed in Chapter 1, ultraviolet (UV) photodetectors are of interest in aerospace, automotive manufacturing, biology, environmental science, and military applications. However, the current technology (photomultiplier tubes) cannot meet the demand due to application constraints in weight, robustness, and power consumption. Here, we consider the properties of the vanadium dioxide on niobium doped titanium dioxide heterostructure (VO_2/TiO_2:Nb) engineered for UV detection.

The information in this study is published in Ref [21].

8.2 Experimental Methods

8.2.1 Sample Growth

The VO_2 was grown on TiO_2:Nb(001) as described by Section 6.2.1.

8.2.2 Structural and Electronic Characterization

The structure of the films was evaluated with AFM, XRD, RHEED, and XRR as described in 6.2.2.

The electrical and quantum efficiency information was determined with an MMR Technology Microprobe System (VTMP) described in Section 5.3. The photovoltage was measured with a Keithley 2182a nano-voltmeter. All measurements were completed at room temperature (~22^{o}C).

8.3 Results

8.3.1 Quantum Efficiency and Detectivity

We determine the photoconductive properties of our detectors using a four-point probe measurement system as described in section Section 5.3 under 0V bias. By subtracting the dark current from total photocurrent, shown in Fig. 8.1a, we calculated the EQE and responsivity R_λ as described in Section 5.3.3:[101–105]

$$EQE = \frac{hcR_\lambda}{e\lambda} \tag{5.13}$$

and

$$R_\lambda = \frac{\Delta I}{P} \tag{5.14}$$

We systematically evaluated the quantum efficiency of VO_2/TiO_2:Nb samples for different thicknesses of VO_2. The EQE for 10 nm, 15 nm and 22 nm VO_2 films on bulk TiO_2:Nb substrates under illumination by a 405 nm diode laser is shown in Fig. 8.1b. All three samples exhibit EQE exceeding 100% at lower light powers. The lower EQE at higher powers is attributable to two effects: the large number of photons that quench the system decreasing the overall photon-to-hole production ratio as well as saturation of the electron-hole photocurrent mechanism. The saturation of the photocurrent mechanism could occur in two ways: the depletion of free electrons in the VO_2 $d_{||}$ band or the depletion of holes from the space charge region in the TiO_2:Nb resulting in the oxygen species at the surface of the heterojunction quenching the delayed recombination effect and reducing efficiency. [80,102,143,144] There is also a clear dependence on the film thickness: the optimal performance was observed in the 22 nm thick VO_2 film with the highest EQE of 4800% and responsivity of 15.7 A/W. A 30 nm thick VO_2 film on undoped TiO_2 substrate is shown in Fig. 8.1b for comparison, to demonstrate that under NUV all doped samples outperform the undoped sample in EQE, responsivity, and low power sensitivity. This increase in EQE suggests that cation doping distinctly affects the photoconducting properties of the VO_2/TiO_2:Nb heterostructure. To compare the proposed detector performance with the performance of a traditional material, and to confirm the accuracy of our EQE measurements as well, we tested a commercially available silicon photodiode (Thorlabs FDS1010) under 0V bias. We found the VO_2/TiO_2:Nb outperforms the silicon photodetector and the measured silicon photodetector performance matches the published responsivity.[145–147]

For evaluation of performance in the deeper UV spectrum, we utilized a 254nm lamp to track EQE in the samples under varied UV-C light powers. The UV-C EQE shown in Fig. 8.1c, shows optimal EQE in the 10 nm thick sample with EQE of 17000% and responsivity of 35.7 A/W, demonstrating a substantial increase in overall performance comparing the 254 nm and 405 nm light. In contrast, we see that the 22 nm thick sample decreases in performance for both EQE and responsivity under the same comparison. We also studied the EQE and responsivity for the 15 nm sample and observed an overall increase in EQE when comparing 254 nm to 405nm illumination consistent with the 10 nm sample. This change in behavior is likely due to the stronger absorption of the 254nm light by the VO_2 layer prior to reaching the heterojunction leading to an increase (decrease) of efficiency in the thinner (thicker) films.[66,148] This suggests that the thickness of the VO_2 film can be engineered depending on the intended wavelength, with thinner samples yielding higher EQE and responsivity at shorter wavelengths of light.[40,66,148]

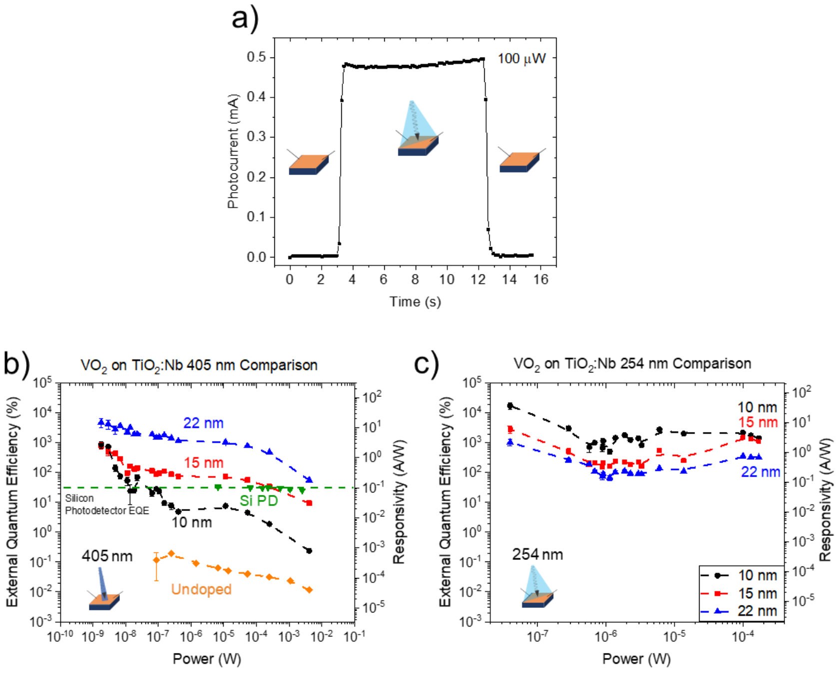

Figure 8.1: a) The 254 nm photocurrent switching of the 15 nm VO_2 sample. (Small inset figures shows the difference in the incident light on the sample: we used a collimated laser beam for 405nm radiation, and a large uncollimated output of a discharge lamp for 254nm.) b) External quantum efficiency (EQE) under 405 nm light for VO_2 films on TiO_2 (undoped) and TiO_2:Nb (10 nm, 15 nm, 22 nm) as well as a silicon photodetector (Si PD). c) External quantum efficiency for VO_2 films on TiO_2:Nb under 254 nm light. The inset figures represent the geometry for the incident light and probe placement on the sample.

We also demonstrate the high detectivity for both the NUV and UV-C spectral regions for all the samples studied following Section 5.3.3:

$$D^* = {A^{1/2}\,R_\lambda}\Big/{(2eI_d)^{1/2}} \tag{5.15}$$

Fig. 8.2 shows the calculated detectivity for the three samples considered under NUV and UV-C illumination. We notice that the general shape of the detectivity curves is similar to the EQE curves, shown in Fig. 8.1. We again observe significant increases in detectivity for all samples under lower light power. In the NUV, the 22 nm thick sample has the highest detectivity, and the 10 nm - the lowest one, though all samples approach a similar detectivity at the lowest NUV light powers. In general, all VO_2 samples outperform the Si photodetector in the NUV. Compared to the NUV case, the order of the detectivity curves for the UV-C radiation is reversed, with the 10 nm film exhibiting the overall highest detectivity, and the 22 nm sample showing the lowest. We additionally see that all samples perform similarly well in the UV-C for all light powers, as opposed to the more pronounced power dependence in the NUV. The relative placements of these curves are determined by the variation in absorption of light at the two wavelengths for different VO_2 film thickness. We also note that for the 10 nm thick VO_2 the dark current density is higher than for the other two (see inset in Fig. 8.3b), which must be taken into account for detector design. This increased dark current is at least partly due to surface discontinuities in the 10 nm sample compared to the thicker films, further asserting the critical importance of the optimization of film thickness. Roughness induced effects from the growth likely influences the EQE, responsivity, and detectivity through effects such as: light scattering at the surface reducing the number of photons reaching the heterojunction or reduced electron mobility barriers from discontinuities due to the lack of uniformity in the heterojunction.

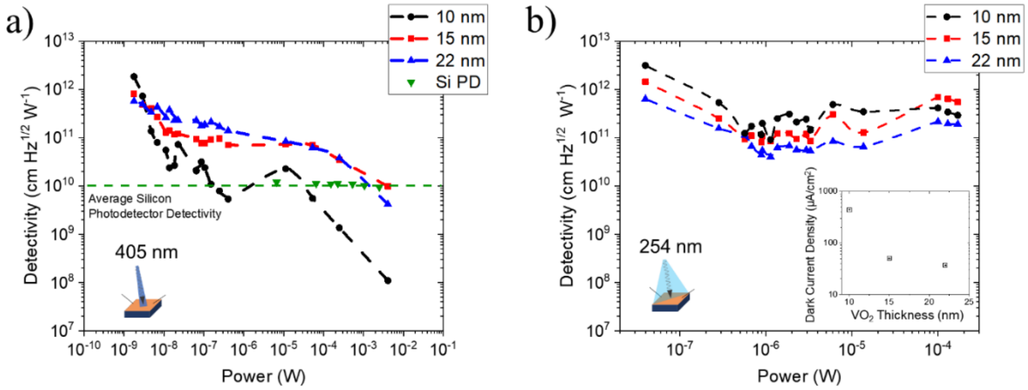

Figure 8.2: a) The detectivity of VO_2 films on TiO_2:Nb under 405 nm light. b) The detectivity for VO_2 films on TiO_2:Nb under 254 nm light where the inset graph is the dark current density for the samples. The inset figures represent the geometric configurations of the incident light on the sample.

8.3.2 Schottky Mott Rule for Heterojunctions

The enhanced photodetection from the VO_2 on TiO_2:Nb heterostructure occurs in two ways: 1) band bending in the heterojunction between VO_2 and TiO_2:Nb and 2) generating a space charge region in the VO_2/TiO_2:Nb heterojunction.[21,70,85] The first process – band bending in the heterojunction – stems from Fermi level matching between VO_2 and TiO_2:Nb driving the bands to accommodate for the change in Fermi level, in our case, increasing band bending to form a potential barrier between the VO_2 and TiO_2:Nb. A simple model to approach the band bending is with the Schottky-Mott rule:

$$\Phi_{BH}{}^{(n)} = \Phi_m - \chi_{SC} \tag{8.1}$$

where $\Phi_{BH}{}^{(n)}$ is the band bending height at the interface of the n type Schottky Mott interface, Φ_m is the work function of the metal, and χ_{sc} is the electron affinity of the semiconductor.[149,150] In our case, we are dealing with an n-type semiconductor to a metal Schottky Mott interface with TiO_2:Nb the semiconductor and VO_2 the metal. The basic n-type Schottky Mott interface is shown in Fig 8.3.

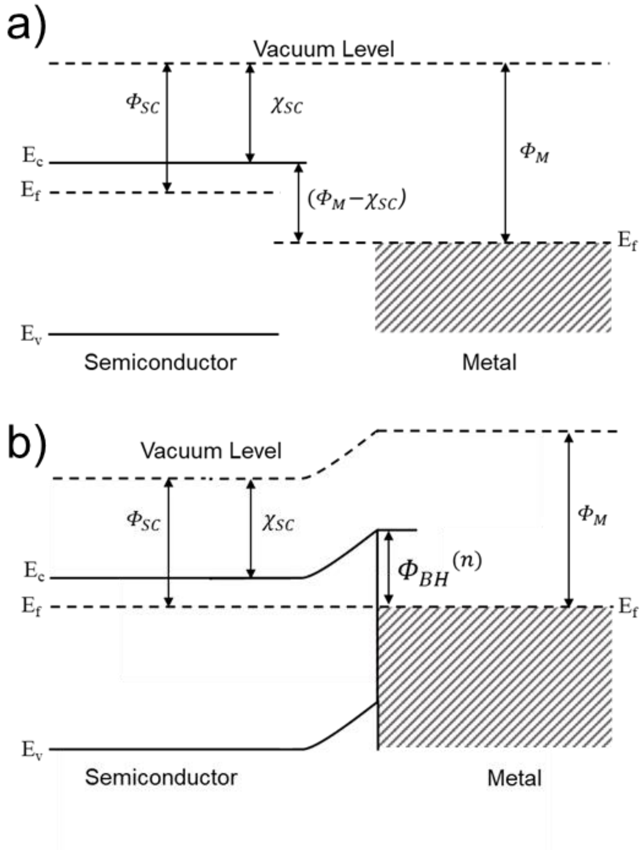

Figure 8.3: a) The band structure for a metal and semiconducting interface prior to contact. b) The metal and semiconducting interface in contact where the region now experiences band bending corresponding to then type Schottky Mott rule. (Here $\Phi_{BH}{}^{(n)}$ is the band bending height at the interface of the n type Schottky Mott interface, $\Phi_{M/SC}$ is the work function of the metal and semiconductor respectively, and χ_{SC} is the electron affinity of the semiconductor.

Using the band bending from the Schottky Mott approximation, $\Phi_{BH}{}^{(n)}$ for the VO$_2$/TiO$_2$ heterojunction is found to be $\Phi_{BH\,VO_2-TiO_2}{}^{(n)} = 1.15\ eV$, with $\Phi_{VO_2} = 5.15\ eV$ and $\chi_{TiO_2} = 4.0\ eV$ noting that doping of TiO$_2$ would likely further increase the band bending.[151–155] This band bending contributes to the formation of a space charge region in the TiO$_2$:Nb creating an in-built electric field that efficiently separates electron-hole pairs in the heterojunction and increases the probability of hole tunneling from the TiO_2:Nb into the VO_2.[71,80] Additionally, this space charge region helps delay the electron-hole pair recombination after photon absorption, thus amplifying the light conversion efficiency. [71,80] A secondary recombination delay is caused by the VO_2 oxygen species trapping holes at the interface.[70,71,102,143,144]. These effects can be engineered in the system by doping the TiO_2 substrates with cations like Nb. [70,71,80]

8.3.3 Alter-valent Cation Doping of TiO_2

Doping TiO_2 with alter-valent cations (Nb^{5+}) adjusts the electronic structure of the TiO_2 in various ways, such as position of the Fermi level or formation of donor energy levels generated by the interaction of interstitial dopants with the lattice.[71] These effects are produced by doping with cations of valency greater than the parent Ti^{4+} cation resulting in an increase of free electrons in the conduction band illustrated by the following reaction:[70,71]

$$Nb_2O_5 \rightarrow 2Nb^{5+}{}_{Ti} + {}^{1}\!/_{2}\,O_2 + 2e^{-}{}_{CB} \tag{8.2}$$

where $Nb^{5+}{}_{Ti}$ denote Nb ions on TiO_2lattice positions, $e^{-}{}_{CB}$is conduction band electrons. We additionally note the following induced lattice defects for Ti (shown in Fig 8.4a): [70]

$$2e^{-}{}_{CB} + 2Ti^{4+} \rightarrow 2Ti^{3+} \tag{8.3}$$

and for O_2 (shown in Fig 8.4b): [70]

$$2e^{-}{}_{CB} + {}^{1}/_{2}\,O_2 \rightarrow {}^{1}/_{2}\,O_2^{-2} \qquad (8.4)$$

These reactions introduce Schottky-type defects throughout the entire TiO_2.[70] As evident in Eqs. 8.2-8.4, the added Nb affects the ratio of defects in TiO_2 by influencing the ratio of Ti^{4+}/Ti^{3+} and the amount of O_2^{-2} present.[70] Three notable effects due to the TiO_2:Nb arise from the introduced defects: (i) decreased separation of the conduction band and Fermi level in TiO_2 , (ii) increased efficiency of photo-generated electron hole pair separation, and (iii) increased band bending. For the first effect, Ti^{3+} ions are formed compensating for the addition of Nb^{5+} dopants in the lattice, described in Eqs. 8.2-8.3. When these Nb^{5+}-Ti^{3+} ion pairs form, a bound state is created acting as a donor level below the TiO_2 conduction band. This donor level adjusts the Fermi level so the flat band potential of the conduction band now exists closer to the Fermi level reducing the overall flat band potential of the TiO_2:Nb.[70,71] The second process, due to the O_2^{-2} defects as described in Eq. 8.4, increases the potential height of the doped TiO_2 surface barrier, facilitating separation of photo-generated electron-hole pairs in the depletion zone.[70,71] Finally, the presence of Nb^{5+} in the lattice steepens the band bending profile at the surface and facilitates photocarrier injection via tunneling by reducing the distance that holes need to travel.[70,71,80] All these processes ultimately result in an optimized electronic structure to pair with VO_2.

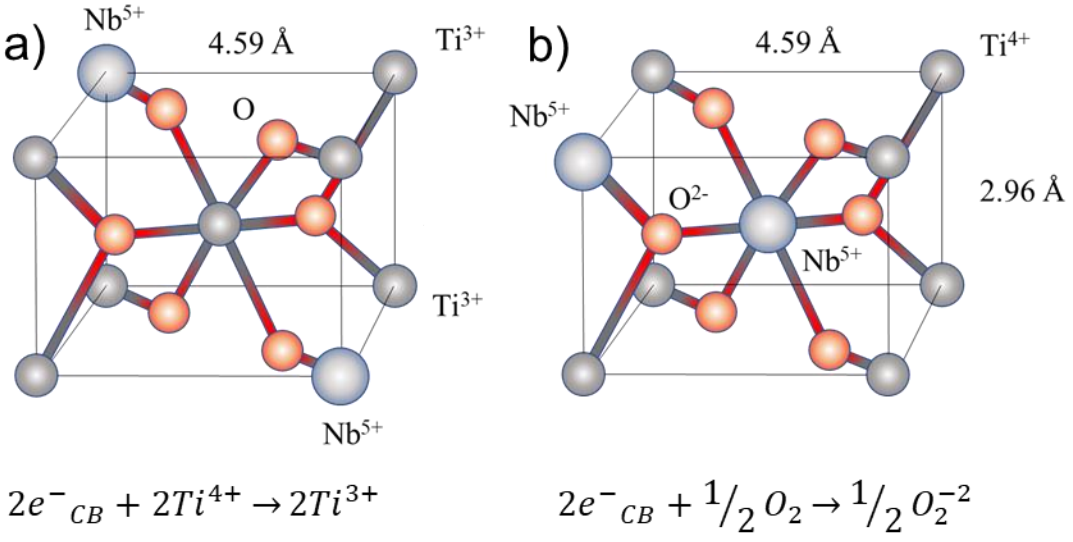

Figure 8.4: a) The TiO_2 unit cell with the Nb^{5+} defects in the lattice corresponding to a) Eq. 8.3 and b) Eq 8.4.

The introduction of a VO_2 film epitaxially on the TiO_2:Nb surface affects the heterojunction in two ways: Fermi level matching between the two materials and generation of a space charge region Δ/Δ^* shown in Fig 8.5a.[70,85] This space charge region is imbued with a built-in electric field,[71] that assists in both efficiently separating electron-hole pairs in the heterojunction as well as favoring hole tunneling from the TiO_2:Nb into the VO_2. [70,71,80,85] The electron-hole pair separation amplifies the light conversion efficiency at the expense of the recombination of these pairs with the additional effect of oxygen species trapping holes at the interface inhibiting recombination in the VO_2.[70,71,102,143,144] Additionally, the cation doping defects and Fermi level matching condition contribute to further enhancing the electric field in the heterojunction.[70,71,85]

The full effect is significant band bending of the TiO_2:Nb conduction band to the $d_{||}^*$ band in VO_2 when compared to the undoped case as shown in Fig. 8.5a,[71,80] where the increased band bending results in a space-charge region endowed with a large electric field affecting particles traversing the heterojunction.[70,71] A diagram of the electron-hole pair movement in the photohole injection, described in Section 4.3, is shown with Fig. 8.5b. Additional effects from the doping induced electric field in the heterojunction would further increase the EQE leading to the greater than 100% EQE. One potential effect from the increased electric field is free holes in the space charge region preferentially tunneling with the photogenerated holes through the space charge region to the VO_2.[149,150] A second effect caused by hole trapping in the TiO_2:Nb bulk and heterojunction, due the oxygen defects, would further amplify the electric field increasing the favorability of free holes to tunnel to the VO_2. [80,102,143,144] One note is that though all light penetration into the TiO_2:Nb causes electron-hole separation, penetration beyond the heterojunction causes electron-hole separation in a field free region. These pairs will quickly recombine in the TiO_2:Nb bulk and thus do not contribute to the detectable photocurrent.[71,80,156]

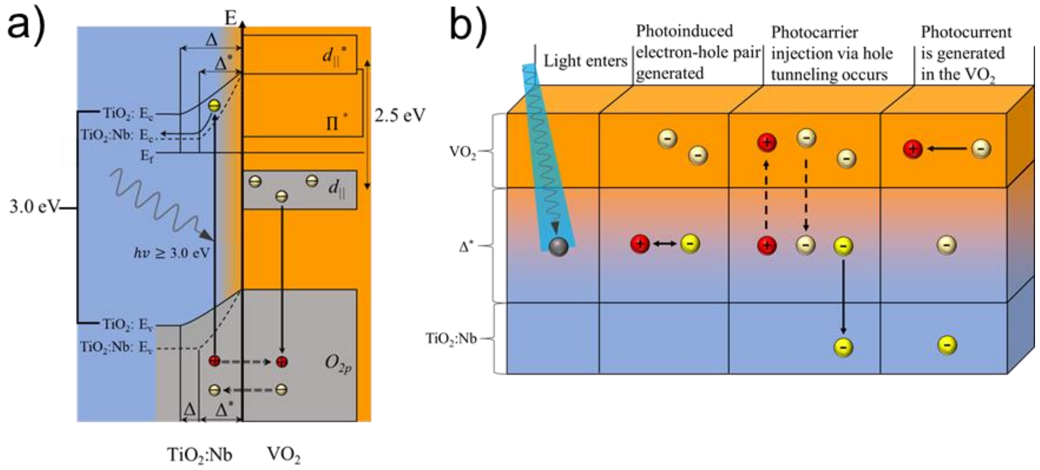

Figure 8.5: a) Band structure diagram comparison for VO_2 films grown on doped TiO_2:Nb and undoped TiO_2 substrate. Where Δ is a space charge region for the TiO_2 structure and Δ^* is the space charge region for the TiO_2:Nb structure. Note, the size of the depletion zone (Δ/Δ^*) is not a reflection of the actual size of the zone. b) Step-by-step diagram of the electron-hole pair movement into the VO_2 film and photocurrent generation. (note: the colors of the figures are matched to correspond to each zone of the heterojunction)

8.4 Conclusion

We demonstrated that a VO_2 on TiO_2:Nb heterostructures exhibit high EQE, responsivity, and detectivity when exposed to either NUV (405 nm) or UV-C (254 nm) light, indicating that such combination of materials is viable for photomultiplier-free UV detection. We consistently observed EQE exceeding 100% in both the NUV and the UV-C spectral ranges. Optimization of the VO_2 film thickness allowed us to reach 4800% EQE for the 22-nm VO_2 film illuminated by 405nm light, and 17,000% EQE for the 10-nm VO_2 film illuminated with 254nm light. However, considering the difference in the dark noise and detectivity, we identified the 15 nm thick VO_2 film as exhibiting best overall performance due to continuous surface coverage, while being thin enough to maximize light transmission to the heterojunction region. We can explain the observed high quantum efficiency by modifications to the band structure in the VO_2 on TiO_2:Nb heterostructure which introduces a space-charge region in the heterojunction. This region produces an electric field that prevents photocarrier recombination by driving photogenerated electrons further into the bulk of the TiO_2:Nb substrate,[70,71] and ultimately yielding favorable conditions for hole tunneling through the depletion zone into the $VO_{2,}$ where recombination takes place producing a photocurrent.[71,80] This effect paired with doping-induced effects on the heterojunction band structure ultimately result in the observed high quantum efficiency.[57,70,71,85] Therefore, engineering VO_2/TiO_2:Nb materials for photodetection yields a promising alternative technology for a UV detector with great potential for scalable device production.

CHAPTER 9

Enhanced Performance of a UV Photodetector Based on Vanadium Dioxide Heterostructures by Application of Gold Contacts

9.1 Introduction

Following the studies discussed in Chapter 8, we sought to enhance the detecting capabilities of the VO_2/TiO_2:Nb heterostructure by introducing Au films to yield beneficial effects on the electronic structure of the heterostructure. [20,21,80] The main effects of noble metal (Au) films on the heterostructure is to enhance the free carrier density in the VO_2/TiO_2:Nb heterojunction and to introduce a space charge region between the Au and both the VO_2 and TiO_2:Nb heterojunctions. This allows for delayed recombination of the photogenerated electron-hole pairs, formed due to UV absorption in the substrate at the interface, amplifying the injection of holes from the TiO_2:Nb substrate into the VO_2 film and increasing the light-photocurrent conversion efficiency. [70,71,80] In addition, Au adjusts the VO_2 carrier emission by increasing the density of free carriers in the Au/VO_2 heterojunction, altering the electronic and optical properties across both insulating and metallic phases, resulting in increased current density through the insulator to metal transition amplifying the relevant switching properties of VO_2.

9.2 Experimental Methods

9.2.1 Sample Growth Method

The VO_2 was grown on TiO_2:Nb(001) as described by Section 6.2.1.

9.2.2 Structural and Electronic Characterization Methods

The structure of the films was evaluated with AFM, XRD, RHEED, and XRR as described in 6.2.2.

The electrical and quantum efficiency information was determined with an MMR Technology Microprobe System (VTMP) described in Section 5.3. The photovoltage was measured with a Keithley 2182a nano-voltmeter corroborated with directly measured photocurrent via a Keithley 2400 Sourcemeter shown in Table C.1. We illuminated the samples with a 532 nm Nd:YAG laser, 254 nm Xe lamp and a 405 nm diode laser. We applied a voltage bias while simultaneously measuring the photocurrent with the Keithley 2400 sourcemeter. All measurement, unless noted otherwise, were completed at room temperature ($\sim 22^{o}$C).

9.3 Results

9.3.1 Au and VO_2 Thin Film Growth

Using sputtering shadow masks, Au thin films are deposited in contact with the VO_2 thin film surface. The growth process has two configurations shown in Fig 9.1a: i) the Au grown first and the VO_2 after (Au/VO_2) ii) the VO_2 grown first and the Au after (VO_2/Au). Annealing steps have been shown necessary during each growth cycle to improve film characteristics, resulting in differing growth conditions for each sequence. The final structure is a set of gold contacts applied to the edges of the TiO_2:Nb with the VO_2 film positioned between. In addition, one sample was grown without Au applied to the surface to directly compare the effects of introducing the Au contacts.

X-ray diffraction (XRD) and atomic force microscopy (AFM), were applied to assess the surface morphology and crystalline quality of the films. All Au and VO_2 films were grown to ~15 nm thick. The XRD pattern, shown in Fig 9.1b), displays the 2ϑ peak location for $VO_2(002)$ grown on TiO_2:Nb. [61] We note that the XRD pattern shown is for the Au/VO_2 sample, but this peak location is consistent for every sample. The single VO_2 film peak location also suggests we have a highly oriented film in the (002) direction.

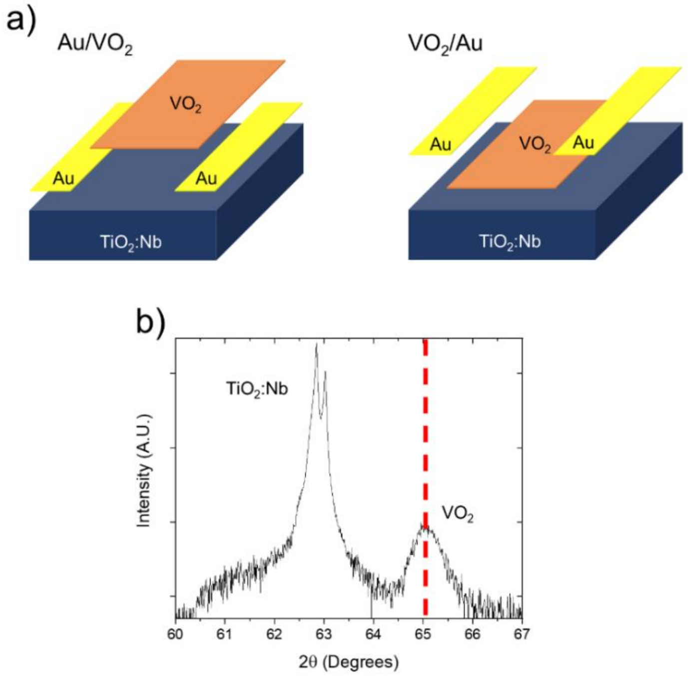

Figure 9.1: a) Schematic representation of the application of the gold and VO_2 to the TiO_2:Nb substrate. (notated Au/VO_2 for the sample with gold applied first and VO_2/Au for the sample with VO_2 applied first.) b) The XRD scan for the VO_2/TiO_2:Nb heterostructure with the VO_2 peak designated with the dashed red line.

9.3.2. Effects of Au contacts on Photohole Injection

As discussed in Chapter 4 and 8, the VO_2/TiO_2:Nb heterostructure takes advantage of the injection of holes from the TiO_2:Nb substrate into the VO_2 film to achieve high detector sensitivity, efficiency, and detectivity under UV illumination. The introduction of niobium cations (Nb^{5+}) into the TiO_2 results in the introduction of beneficial defects into the TiO_2 lattice that: (i) decrease separation of the conduction band and Fermi level in TiO_2, (ii) increase the efficiency of photo-generated electron hole pair separation, and (iii) increase band bending as noted in

Chapter 8. One notable effect from this cation doping is the band bending will allow for access to lower energy (<3.0eV) light originally forbidden in the TiO_2 (3.0eV band gap) seen in Fig 9.2a,b.

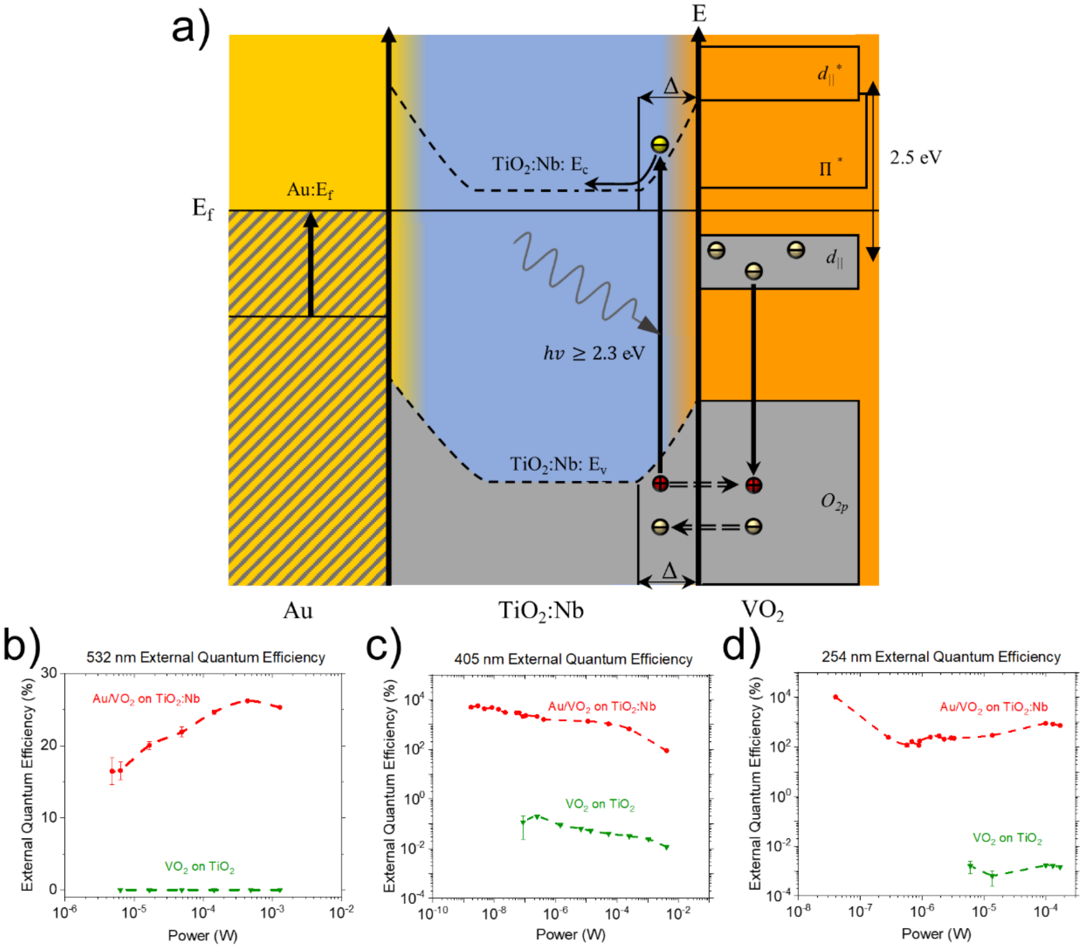

Figure 9.2: a) Band structure diagram and photo hole injection for the Au and VO_2 films grown on doped TiO_2:Nb. Here, Δ is the space charge region for the VO_2/TiO_2:Nb heterostructure (the size of the depletion zone in the diagram does not corresponds to its actual size). The Fermi level (E_f) is represented by the solid line. The adjustment to the Fermi level of the Au (Au:E_f) and the resulting band bending in the TiO_2:Nb (dashed lines) are also shown. b-d) The external quantum efficiency for b) 532 nm c) 405 nm and d) 254 nm light, showing the improvements between Au/VO_2 on TiO_2:Nb and VO_2 on TiO_2 samples.

Following the discussion in 8.3.2, Au is added to enhance the VO_2 and TiO_2:Nb light conversion efficiency, by increasing the free carrier density and forming a secondary space charge region that penetrates deep into the lower carrier density semiconducting material. [71,157] This transfers charges from the VO_2 and TiO_2:Nb to the Au film such that both heterojunctions, i.e. Au/VO2 and Au/TiO2:Nb, exhibit band bending, also shown in Fig. 9.2a.[71,157] We approximate the band-bending height using the Schottky-Mott rule[149,150]:

$$\Phi_{BH}{}^{(n)} = \Phi_m - \chi_{SC} \tag{8.1}$$

We find $\Phi_{BH,Au-VO_2}{}^{(n)} = 1.76\ eV$ and $\Phi_{BH,Au-TiO_2}{}^{(n)} = 1.31\ eV$, respectively for each heterojunction, where $\Phi_{Au} = 5.31\ eV$, $\chi_{VO_2} = 3.55\ eV$, and $\chi_{TiO_2} = 4.0\ eV$. [66–68,151–155] Additionally, the enhanced space-charge region results in deeper free holes in VO_2 and TiO_2:Nb when Au is added compared to the depletion zone of just VO_2/TiO_2:Nb.[71,149,150,157] The increased hole density and depth of the depletion zone causes photoinjected carriers to combine with more free holes in the bulk,[71] preventing recombination of the photoexcited carriers resulting in enhanced light conversion efficiency and EQE as seen in Fig 9.2b-d. [71,149,150,157]

9.3.3. Figures of Merit for an Au/VO_2-based Photodetector

To experimentally demonstrate the advantages of adding Au contacts on the photoconducting properties of the VO_2/TiO_2:Nb, we proceeded to test the vis-UV detection enhancement of the detectors with and without contacts by examining relevant figures of merit: external quantum efficiency (EQE), responsivity, detectivity, and dark current density. We determine the photoconductive properties of our detectors using a four-point probe measurement system as described in Section 5.3 under 0V bias. We calculated the EQE and responsivity R_λ as described in Section 5.3.3: [101–106]

$$EQE = \frac{hcR_\lambda}{e\lambda} \tag{5.13}$$

and

$$R_\lambda = \frac{\Delta I}{P} \tag{5.14}$$

For each wavelength, the responsivity and external quantum efficiency obeys the same relationship as shown in Fig 9.3a-b. The introduction of Au demonstrates the greatest and most substantial improvements for 405 nm light and only slight improvements for 254 nm. The highest EQE and responsivity, detected for the Au/VO_2 samples, is 5000% and 18 A/W for 405 nm, and 10000% and 21 A/W for 254 nm light respectively. To verify the proper calibration of our detection method, we also tested the EQE and responsivity of the samples with a commercially available detector (Thorlabs FDS1010) for 405 nm matching the published values for the detector. [145–147] Thus the EQE and responsivity shown in Fig 9.3a-b demonstrates that the application of gold contacts induces substantial improvements in photosensitivity and efficiency.

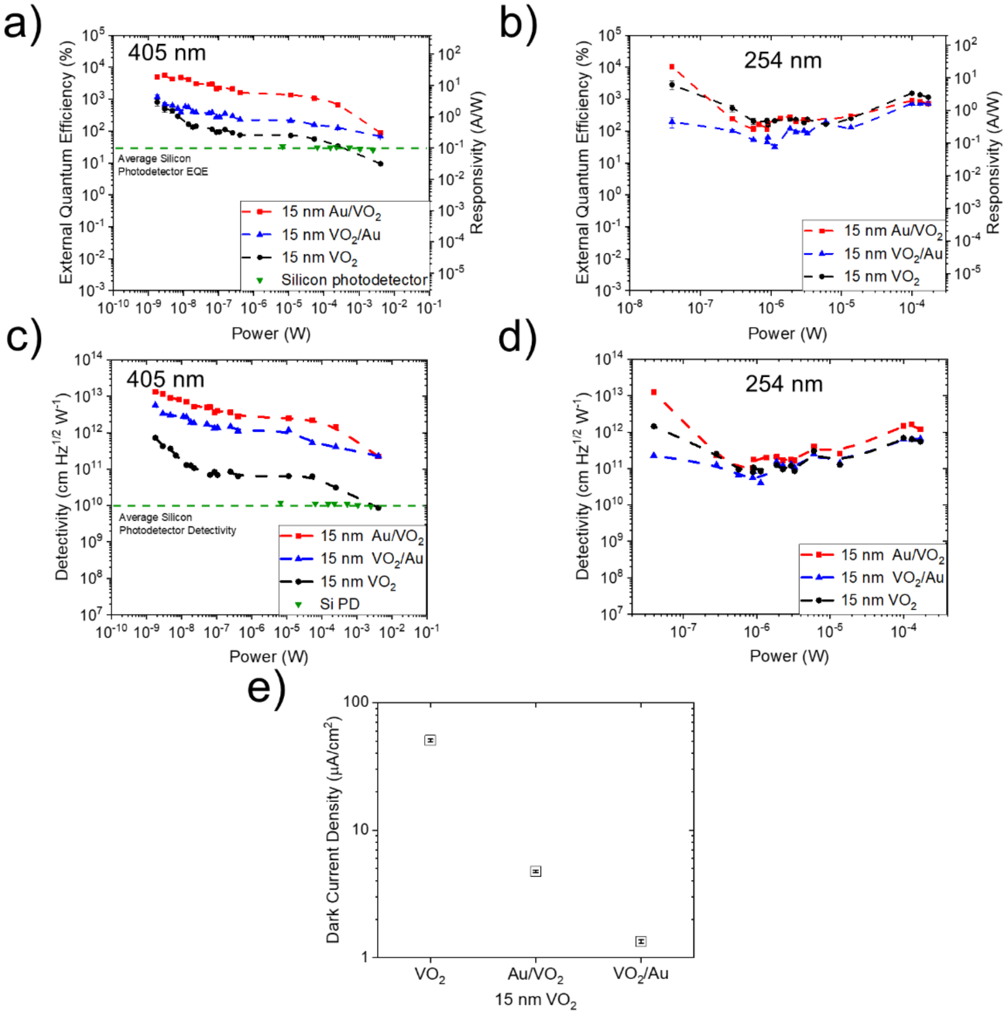

Figure 9.3: External quantum efficiency (EQE) and responsivity for a) 405 nm and b) 254 nm illumination and the detectivity for c) 405 nm and d) 254 nm for the VO_2, Au/VO_2, and VO_2/Au sample. e) The dark current density for each the VO_2, Au/VO_2, and VO_2/Au sample.

We also demonstrate the high detectivity for both the NUV and UV-C spectral regions for all the samples studied following Section 5.3.3:

$$D^* = {A^{1/2}\, R_\lambda}\Big/{(2eI_d)^{1/2}} \qquad (5.15)$$

We found that once more the Au/VO_2 sample is the highest performing sample for both NUV and UV-C radiation, reaching detectivity values for NUV: ~1.5 x 10^{13} $\frac{cm\,\sqrt{Hz}}{W}$ and UV-C: ~ 2 x 10^{13} $\frac{cm\,\sqrt{Hz}}{W}$ as seen in Fig 9.3c-d.

Finally, the presence of noble metal contacts such as Au is expected to reduce the dark current in detectors, a particularly critical figure of merit for low light detection.[2,5,71,107,108] Indeed, Fig. 6.3e) shows an order of magnitude reduction of the dark current in the sample with gold contacts compared to pure VO_2. This reduction in dark current in addition to the previously established improvements to other figures of merit is shown in Table 9.1.

Table 9.1: Figures of Merit for VO_2 Heterostructures

Figures of Merit	VO_2/TiO_2 *30 nm film*	VO_2/TiO_2:Nb *15 nm film*	$Au/VO_2/TiO_2$:Nb *15 nm film*
Maximum EQE : (%)			
at 254nm:	10^{-3} at 10^{-6} W	$3 \cdot 10^{3}$ at 10^{-8} W	10^{4} % 10^{-8} W
at 405nm:	0.2% at 10^{-7} W	$8 \cdot 10^{2}$ at 10^{-9} W	$5 \cdot 10^{3}$ % 10^{-9} W
Maximum Responsivity : $\left(\frac{\mathrm{A}}{\mathrm{W}}\right)$			
at 254nm:	$3 \cdot 10^{-6}$ at 10^{-6} W	6 at 10^{-8} W	21 at 10^{-8} W
at 405nm:	$6 \cdot 10^{-4}$ at 10^{-7} W	3 at 10^{-9} W	18 at 10^{-9} W
Maximum Detectivity : $\left(\frac{\mathrm{cm}\sqrt{\mathrm{Hz}}}{\mathrm{W}}\right)$			
at 254nm:	$9 \cdot 10^{7}$ at 10^{-6} W	10^{12} at 10^{-8} W	10^{13} at 10^{-8} W
at 405nm:	$2 \cdot 10^{7}$ at 10^{-7} W	$7 \cdot 10^{11}$ at 10^{-9} W	$2 \cdot 10^{13}$ at 10^{-9} W

9.3.4. Gold Carrier Emission Enhancement

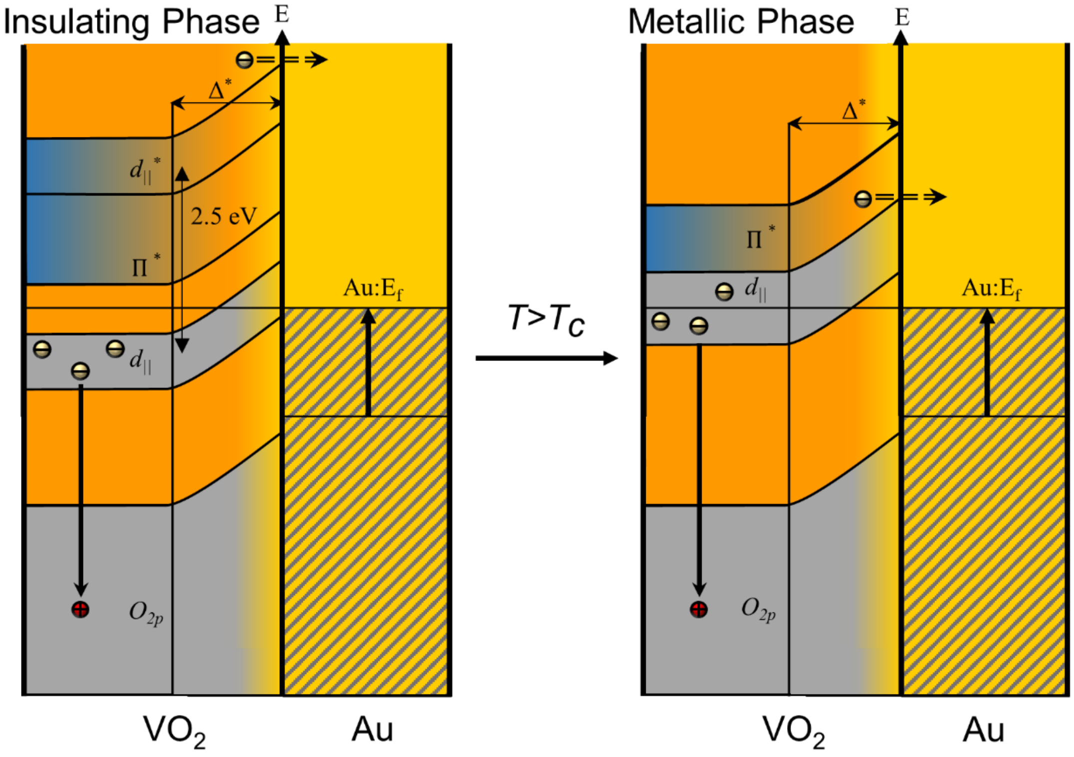

Figure 9.4: Band structure diagram comparison for Au/VO$_2$ films in the insulating and metallic phases of VO$_2$. Noting Δ^* is the space charge region for the Au on VO$_2$ and T$_c$ is the temperature that VO$_2$ transitions from the insulating phase to the metallic phase. We see the electron emission from the VO$_2$ into the Au above the Fermi energy and the photocurrent production via the hole injection from the TiO$_2$:Nb in the VO$_2$ below the Fermi energy.

The application of the Au films also affects VO$_2$ IMT characteristics. The increased free carrier density and the introduction of the space charge region with VO$_2$ results in a more efficient free carrier emission under bias, as shown in Fig 9.4, and a greater difference in current density between the insulating and metallic phases. Furthermore, the collapse of the d$_{||}$ bands during the insulator to metal transition lowers the potential barrier for free carrier emission,[32,57,80] resulting in increased carrier emission over the barrier[71,149,157] as well as increased carrier movement into the Au and higher detectable current.[157]

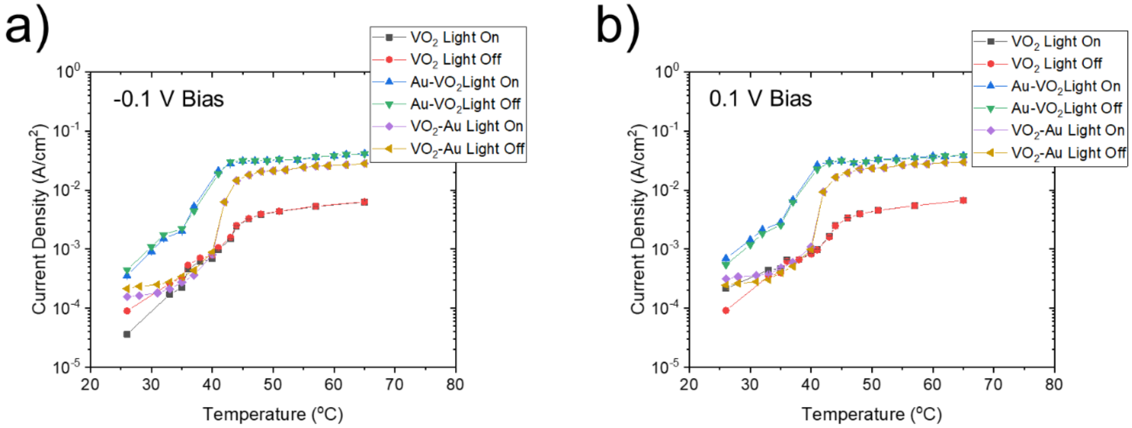

Figure 9.5: The current density of the samples with a) reverse bias of -0.1V and b) forward bias of 0.1V as the temperature was cycled from 22^{o}C and 68^{o}C and each sample was illuminated with 254 nm light. The positioning of the ON and OFF curves between the reverse and forward bias is due current direction changing depending on the bias while the photocurrent due to photohole injection only occurs in one direction. The critical temperature of IMT for these samples are ~38^{o}C for VO$_2$ and Au/VO$_2$ and ~42^{o}C for VO$_2$/Au.

To experimentally demonstrate the effects of the Au on the VO$_2$ insulator to metal transition, we applied a small bias (±0.1V) to induce electron emission and monitored the current density evolution during the thermally induced IMT with and without 254 nm illumination. The resulting measurements are shown in Fig. 9.5. With the applied bias, we observe a sharp increase in the detected current once VO$_2$ film undergoes the IMT. This finding is consistent with reported electron movement under bias, where the metallic state of VO$_2$ is conductive thus a lowered potential barrier for carrier emission from the VO$_2$ to the Au. [149,150] This results in increased movement of carriers from the VO_2 to the Au.[149,150] It is important to note that the samples display photocurrent production through the transition even though the VO_2 $d_{||}$ band collapses in its metallic state. This photocurrent runs contrary to what we observed with the VO_2 on TiO_2 in Section 6.3.3 where the photocurrent was reduced to zero upon transition. Therefore, the doping and the voltage bias allows the production of a photocurrent through the transition.

The samples with Au contacts exhibit higher overall current density, and a substantially larger current difference across the IMT. This observation can be attributed to increased carrier emission paired with the naturally higher free carrier density of Au, shown in Fig. 9.4, resulting in overall higher current values.

9.4. Conclusion

We have observed enhancements in the detective characteristics (external quantum efficiency, responsivity, detectivity, and dark current density) of VO_2/TiO_2:Nb heterostructure by applying Au contacts. We found that applying Au contacts substantially amplifies responsivity, EQE, and detectivity at 405 nm with more modest improvements at 254 nm. These findings demonstrate the great potential of a Au-on-VO_2 detector for various vis-UV detection applications. We also observed that the application of the Au films alters the VO_2 insulator to metal transition resulting in an order of magnitude increase in current density through the transition compared to the bare VO_2 film. Such enhancement can be used, for example, in thermal switching applications.[158,159] Application of noble metals such as Au yield definitive improvements to the already sensitive and detective characteristics of a VO_2/TiO_2:Nb photo-detectors.

CHAPTER 10

Conclusion and Outlook

10.1. Conclusions

In this thesis, I discussed the growth and characterization of VO_2 films on various substrates to demonstrate the UV detection capabilities of the VO_2 on TiO_2:Nb heterostructure. This heterostructure is a novel and promising approach to photomultiplier-free UV detection, displaying high-efficiency detection in both NUV (405 nm) and UV-C (254 nm) spectral regions with zero bias at room temperature, addressing the detection needs of many in-demand fields.

I began by presenting the in-plane crystal structure of the high quality epitaxial VO_2 films on c-Al_2O_3 and TiO_2 using RHEED. This approach allowed me to present a first of its kind RHEED temperature transition analysis for VO_2, in which, we analyzed the structural phase transition of VO_2 on both c-Al_2O_3 and

TiO_2(001), evidencing the dynamical changes to VO_2 through its critical transition temperature. This structural examination was supplemented with the photoconducting properties of the VO_2 on both substrates, demonstrating a photocurrent with up to a 2000% difference in quantum efficiency from 4.6 mW to 250 nW laser power with VO_2 on TiO_2 and no photocurrent for c-Al_2O_3.

Following the examination of the VO_2 structure with RHEED, I present the growth evolution for VO_2 thin films on TiO_2(002) substrates by examining the dynamic scaling relationships at several film thicknesses in Chapter 7. We extracted a series of growth exponents corresponding to the intrinsic anomalous scaling class, suggesting that nonlocal effects play a significant role during the evolution of the film. We conclude, the intrinsically anomalous scaling observed likely arises from a combination of reactive sputter deposition and interfacial strain effects between the film and substrate.

I then demonstrated that VO_2 on TiO_2:Nb heterostructures exhibit high EQE, responsivity, and detectivity when exposed to either NUV (405 nm) or UV-C (254 nm) light. We consistently observed EQE exceeding 100% in both the NUV and the UV-C spectral ranges. Optimization of the VO_2 film thickness allowed us to reach 4800% EQE for the 22 nm VO_2 film illuminated by 405nm light, and 17,000% EQE for a 10 nm VO_2 film illuminated with 254nm light. We identified the 15 nm thick VO_2 film as exhibiting best overall performance, due to the continuous surface coverage but also being thin enough to maximize light transmission to the heterojunction region. Finally, we explained the observed high quantum efficiency by modifications to the band structure in the VO_2 on TiO_2:Nb heterostructure, yielding favorable conditions for hole tunneling producing a photocurrent in the VO_2. This effect paired with doping-induced effects on the heterojunction band structure result in the observed high quantum efficiency.

Finally, I presented enhancements to the detective characteristics of VO_2/TiO_2:Nb heterostructure by applying Au contacts to the heterostructure. The Au contacts substantially amplified responsivity, EQE, and detectivity at 405 nm with more modest improvements at 254 nm. We observed that the application of the Au films alters the VO_2 insulator to metal transition, resulting in an order of magnitude increase in current density through the transition compared to the bare VO_2 film.

These findings culminate to a highly efficient and sensitive UV detector using the VO_2 thin film on TiO_2:Nb substrate heterostructure as a novel and efficient approach to photomultiplier-free UV detection. With the benefit of magnetron sputter deposition, the VO_2/TiO_2:Nb detector is a cost efficient, scalable UV detector scheme suitable for practical device development and production, with direct application to the neutron detection scheme shown in Figure 1.3.

10.2. Outlook

Photomultiplier-free UV detection remain a subject of great interest due to the demand in several application areas. The materials needed to address these needs have proven non-trivial to manufacture and multiple avenues have been used to approach the problem. While detection materials such as silicon and wide band gap semiconductors have been investigated, the application and production constraints make practical implementation of these devices difficult.

The presented VO_2/TiO_2:Nb heterostructure addresses many of the difficulties encountered with the other materials used for UV detection. However, further investigation is needed into additional figures of merit, implementation into a detector design, and determining the true scalability of the VO_2 growth via magnetron sputtering. Regardless of the ultimate solution to photomultiplier free UV detection, the information presented here demonstrates the VO_2/TiO_2:Nb heterostructure as a novel approach to high efficiency and sensitivity, broadband UV detection using traditionally scalable production techniques, potentially spurring new avenues of high efficiency and sensitivity light detection for other spectra as well.

Appendix A

Supplementary Information for the Structural and Photoelectric Properties of Epitaxially Grown Vanadium Dioxide Thin Films on c-Plane Sapphire and Titanium Dioxide

A.1. Vanadium Dioxide Growth Calibration

We sought to grow high quality VO_2 films to yield quality diffraction patterns in reflection high energy electron diffraction (RHEED). Therefore, we used the pulsed reactive magnetron sputter deposition growth method, as discussed in Chapter 5, to grow and optimize 30 nm thick (60 min growth time) vanadium dioxide thin films. We began by determining the ideal O_2 partial pressure percentage for a set of VO_2 films on c-Al_2O_3(0001) substrates as described in Table A.1

Table A.1: Vanadium Dioxide Partial Pressure Growth Series

O_2 Pressure (%)	Power (W)	VO_2 Film (%)	b-Lattice Parameter (Å)	Grain Size (nm)	Mosaicity ($^\circ$)
11	40	9.06	4.52	33.70	0.094
10	40	26.39	4.52	33.59	0.097
9	40	63.03	4.52	32.83	0.080
8	40	95.75	4.51	44.65	0.075
7	40	95.84	4.50	45.91	0.063

We supplemented the O_2 partial pressure series with a bias power calibration series to determine the optimal growth power as shown in Table A.2.

Table A.2: Vanadium Dioxide Bias Power Growth Series

O_2 Pressure (%)	Power (W)	VO_2 Film (%)	b-Lattice Parameter (Å)	Grain Size (nm)	Mosaicity ($^\circ$)
10	120	39.30	4.63	12.16	0.060
10	80	95.87	4.52	53.01	0.099
10	60	77.22	4.52	45.99	0.109
10	40	82.70	4.52	55.38	0.128

From these series, we optimized the VO_2 growth to the bias pulse reversal rate of the sputtering system. We proceeded by maintaining ~8% O_2 partial pressure at 40 W of bias power in the sputtering system. Using these parameters, we optimized the growth to the pulsed power as described in Table A.3.

Table A.3: Vanadium Dioxide Pulsed Power Growth Series

Pulse Reversal (µs)	Pulse Frequency (kHz)	VO_2 Film (%)	b-Lattice Parameter (Å)	Grain Size (nm)	Mosaicity ($^\circ$)
4	100	100	4.52	56.24	0.109
3	100	98.21	4.52	64.33	0.096
2	100	50.95	4.52	40.39	0.120
1	100	60.56	4.52	36.99	0.134

The pulsed power series demonstrated that the most optimal pulse reversal time was between 4-3µs at 100 kHz pulse frequency. We transferred this set of growth parameters to the VO_2 on TiO_2(001) growth as shown in Table A.4.

Table A.4: Vanadium Dioxide on TiO_2(001) Growth Series

O_2 Pressure (%)	Power (W)	Pulse Reversal (µs)	Pulse Frequency (kHz)	VO_2 Film (%)	c-Lattice Parameter (Å)	Grain Size (nm)	Mosaicity ($^\circ$)
8	40	4	100	100	2.86	27.01	0.044
8	40	3	100	100	2.86	19.59	0.048

A.2. Supplementary RHEED Patterns

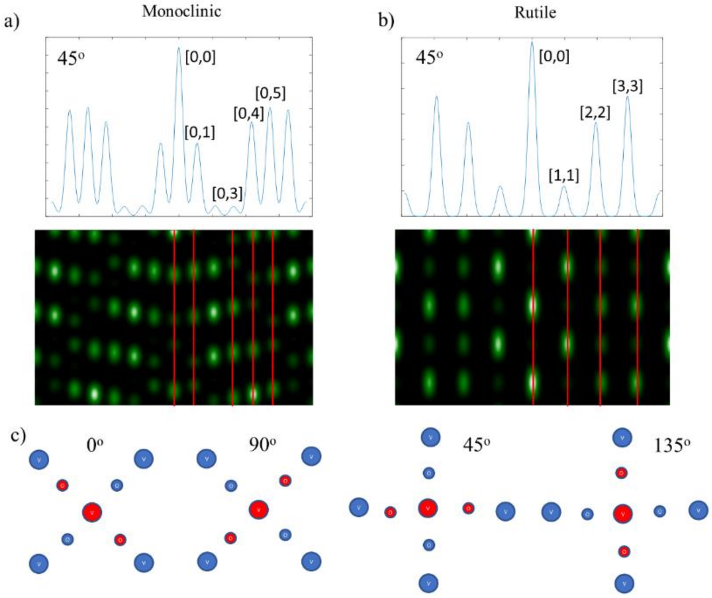

Figure A1: The experimental XRD, AFM, and simulated RHEED patterns of VO_2 on c-Al_2O_3 and TiO_2. a) The simulated RHEED patterns of the 45^{o} rotation for the monoclinic phase of VO_2 where the streak intensity patterns are recorded on top and the simulated diagrams are reported on bottom with the in plane lattice planes are recorded for each. b) The simulated RHEED patterns of the 45^{o} rotation for the rutile phase of VO_2 where the placement of the plots is the same as the previous monoclinic phase. c) The orientations of the vanadium and oxygen atoms through the rotations of one unit cell where the first two surface layers of atoms are shown in the c-direction with the red layer is displaced ~1.44 nm below the blue layers.

We demonstrate the 45^{o} azimuthal rotation RHEED simulation for VO_2 in both the monoclinic and rutile phases shown in Fig. A1a-b. Additionally, in Figure A1c we show the lattice positions of the vanadium and oxygen atoms through various azimuthal rotations. We also demonstrate the azimuthal rotations in the experimental RHEED patterns for VO_2 through the transition as shown in Fig. A2a-d that were not shown in the primary manuscript.

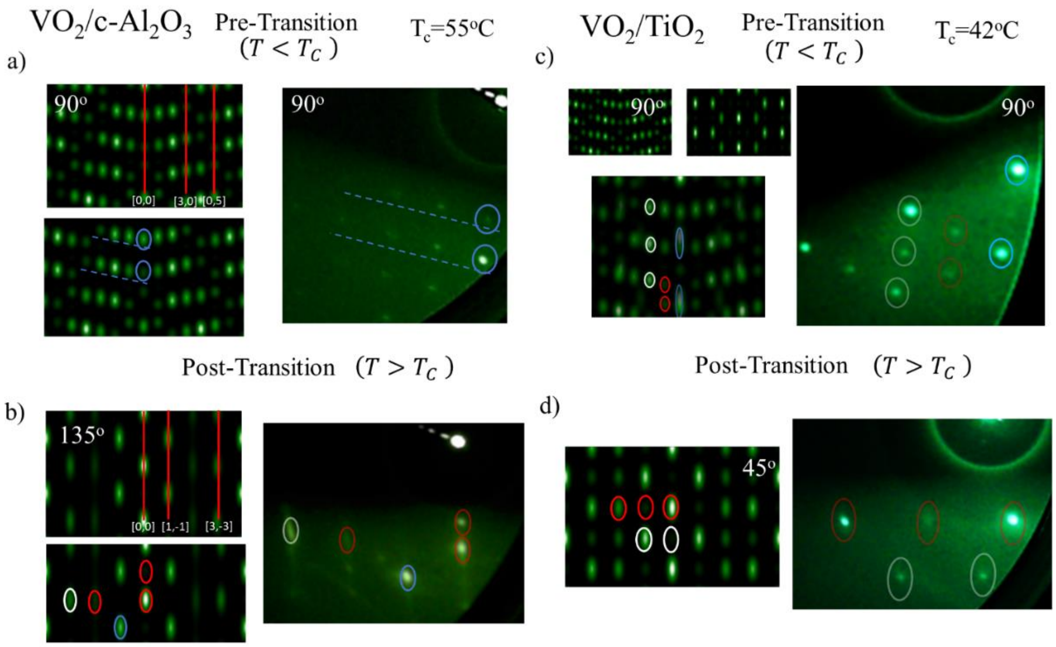

Figure A2: The simulated and experimentally determined RHEED patterns for VO_2 on c-Al_2O_3(0001) and VO_2 on TiO_2(001). For VO_2 on c-Al_2O_3(0001): Simulated and experimental RHEED patterns of VO_2 azimuthal rotations and for the two phases. a) The left two images are simulations of the 90° rotation for the monoclinic phase of VO_2; the top image denotes the 2-D lattice planes for the streak patterns while the bottom image has streaks highlighted. The right image is the experimentally determined RHEED pattern the highlighted streaks correspond to the simulated image. b) The plot orientation is maintained for where the simulated images are shown at left and experimental images at right for the 135° rotation for the rutile phase of VO_2. For VO_2 on TiO_2(001): c) The 90° rotation for the VO_2 on TiO_2 pre-transition where the top leftmost two images are simulations of the 90° rotation for the monoclinic phase (left) and rutile phase (right) of VO_2. The bottom left image is a superimposed image of both simulated images. The right image is the experimentally determined RHEED pattern for VO_2 on TiO_2(001) where the highlighted streaks correspond to the simulated images. d) The left image is the simulated 45° rotation for rutile phase VO_2 and the right image is the experimental pattern for the rutile phase VO_2 grown on TiO_2(001). (Note: All images have been rotated 45 degrees and the contrast has been increased for ease of streak identification)

Appendix B

Supplementary Information for Materials Engineering in Vanadium Dioxide / Niobium Doped Titanium Dioxide Heterostructures for Ultraviolet Detection.

B.1. Hysteretic Response

Transition metal oxides (TMOs) are of significant interest especially materials exhibiting insulator to metal transitions (IMT) arising from conduction band splitting.[31,46,57,80] Vanadium Dioxide (VO_2) is a TMO that exhibits an insulator to metal transition with an accompanying structural transition, from monoclinic (insulating) to tetragonal (metallic).[37,39–41,50] This insulator to metal transition has been found to occur in bulk at T_c=68°C.[37,39–41,50] The sharpness of the transition and the hysteretic width upon thermal treatments is generally considered a good indicator of a stoichiometric ratio close to that of pure VO_2.[160] Therefore, we monitored the insulator to metal transition of the various samples with a 405 nm laser shown in Fig B.1.

We do note that with thin films the sharpness of the transition and the hysteretic width are strongly affected by growth parameters such as strain and defect presence.[61] Thus, deviations in the sharpness and hysteretic width may be also affected by strain. We additionally note for the undoped (TiO_2) version of this thin film heterostructure a change in transition temperature of up to 40°C lower than the bulk transition temperature has been found and is largely based on the strain dynamics in the film.[61]

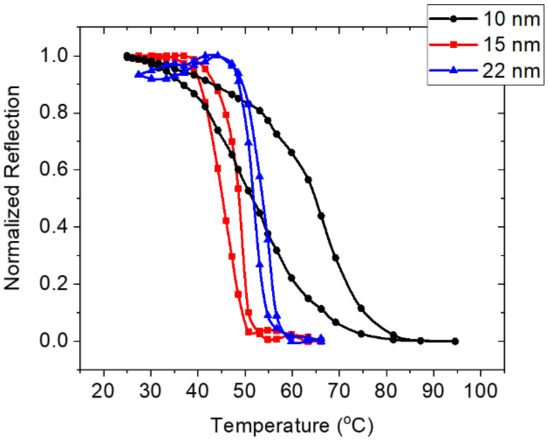

Figure B.1): The thermally induced insulator to metal transition monitored with 405 nm light for the 10 nm, 15 nm, and 22 nm thick VO_2 grown on TiO_2:Nb.

B.2. Structural Determination

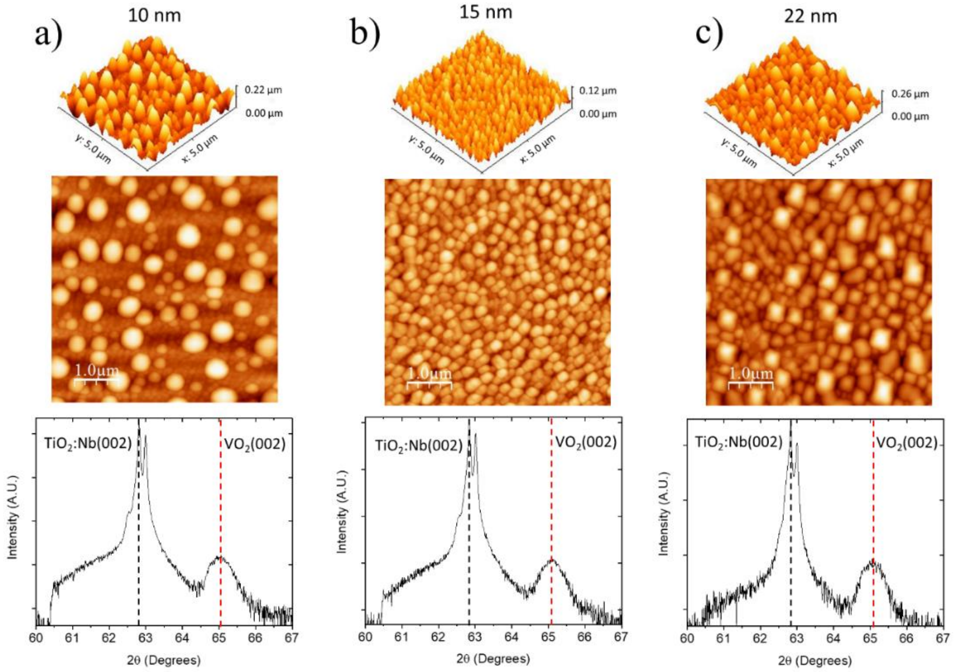

Figure B.2: The 3 dimensional representation of the surface profile (top), the 2 dimensional surface profile (center), and the XRD peak location for the TiO_2:Nb and the VO_2 peak locations (bottom) for a) 10 nm b) 15 nm c) 22 nm thick VO_2 samples.

The microstructure characterization of the films was carried out using X-Ray Diffraction (XRD) symmetric scans with a four-circle diffractometer utilizing a monochromatic $\text{CuK}_{\text{alpha}}$ (λ=1.5406Å) beam. Upon examination of the 2ϑ scans we determined that the peak location for VO_2 grown on TiO_2:Nb(002) (shown in Fig. B.2) was consistent with previous reports for thin film growth on TiO_2 substrates.[61] The location of a singular peak aside for the substrate peak indicates growth of singularly VO_2 and no other vanadium oxide combinations. We expect slight deviations of the peak location in comparison to the TiO_2 peak locations due to the added Nb dopant to the TiO_2 lattice. We also note that the Titanium Dioxide's lattice structure is tetragonal (space group: $P4_2/mmm(136)$) and similar to that of the tetragonal structure (space group: $P4_2/mmm(136)$) of VO_2 though the lattice parameters of TiO_2 are larger than that of VO_2, as demonstrated by Table B.1, thus inducing lattice strain when VO_2 is in the rutile phase.[56,61,72] In the insulating VO_2 phase, the lattice mismatch is larger (space group: $P2_1/c$ (14)) thus leading to a larger degree of lattice strain This in turn results in formation of grains in the film where the monoclinic structure is strained toward the tetragonal phase.[56,72] We additionally used the XRD to characterize the mosaicity (degree of crystallite order), grain size of the crystallites, and lattice parameter as shown in Table B.2.

Table B.1: Lattice Constants VO_2 and TiO_2

	VO_2(Monoclinic)	VO_2(Rutile)	TiO_2(Rutile)
a (Å)	5.75	4.55	4.59
b (Å)	5.42	4.55	4.59
c (Å)	5.38	2.88	2.96

The surface characterization was determined via Atomic Force Microscopy (AFM) in non-contact mode with an AppNano ACTA AFM tip of nominal tip diameter ~10 nm.[92,136] Through this characterization, we find the RMS roughness of the films displayed in Table B.2. We note the stark difference in surface structure when comparing the thicknesses, we can see for the 10 nm samples we have large nucleation zones of VO_2 material with very little film between while the 15 and 22nm samples display full surface coverage and a relatively uniform surface as demonstrated in Fig. B.2.

Table B.2: RMS Roughness, c-Direction Lattice Parameter, Mosaicity, and Grain Size of VO_2 grown on TiO_2:Nb

VO_2 Thickness (nm)	10	15	22
RMS Roughness (nm)	28.4	12.0	25.4
Lattice Parameter c-direction (Å)	2.86	2.86	2.87
Mosaicity (^{o})	0.45	0.41	0.42
Grain Size (nm)	21.2	23.2	22.4

Appendix C

Supplementary Materials for Enhanced Performance of a UV Photodetector Based on Vanadium Dioxide Heterostructures by Application of Gold Contacts

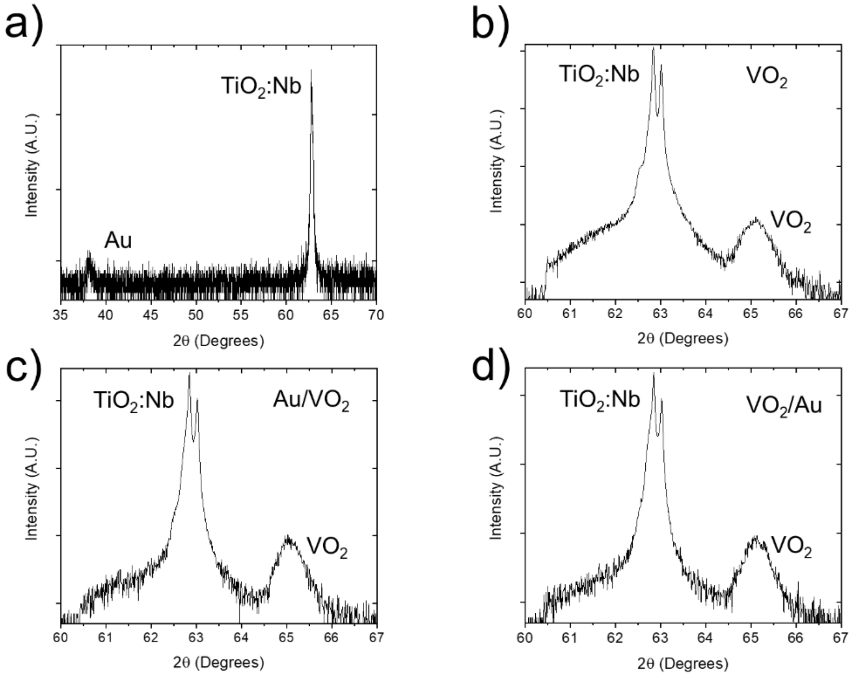

Figure C.1: The XRD scan for a) the Au (111) peak location on the TiO_2:Nb substrate prior to VO_2 deposition. The XRD for VO_2 on TiO_2:Nb heterostructure for b) the Au contact free VO_2 sample, c) Au/VO_2 sample, and d) VO_2/Au sample.

We grew a set of 15 nm VO_2 (002) samples with Au (111) contacts and a single sample without Au to compare the effects of the Au to the VO_2 (002) /TiO_2:Nb (002) heterostructure. Utilizing X-ray diffraction (XRD) and atomic force microscopy (AFM), we assessed the morphology, crystalline quality, and surface characteristics of the films. The XRD patterns, shown in Fig C.1a-d), displays the 2θ peak location for a) Au(111) on the TiO_2:Nb prior to VO_2 deposition and the VO_2 peak location for the b) VO_2 c) Au/VO_2 and d) VO_2/Au. Au/VO_2 is the sample with Au is grown first and VO_2/Au is the sample with VO_2 grown first .

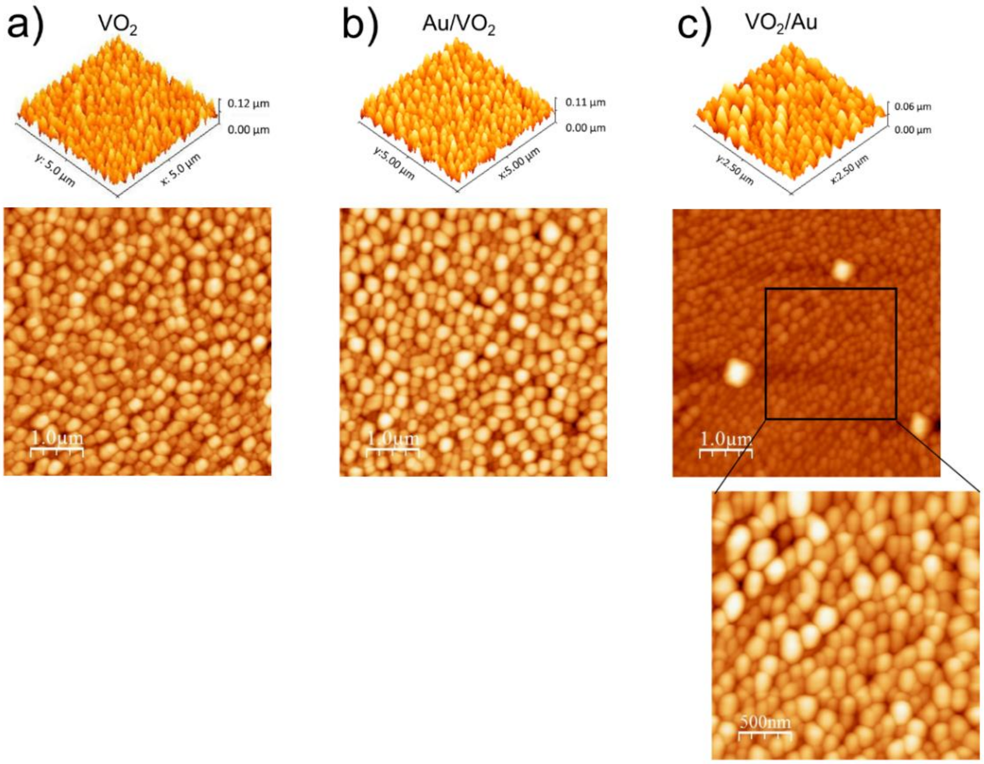

Figure C.2: The 5μm x 5μm AFM scans for the a) VO_2, b) Au/VO_2, and c) VO_2/Au. The top images are the 3-D representations of the surfaces the middle images are the 2D representations of the surfaces and the projection for c) is the 2.5μm x 2.5μm scan for the VO_2/Au surface.

The surfaces of the films were determined with AFM scans shown in Figure C.2 a-c), these scans display similar surface morphology, this is apparent between the VO_2 and the Au/VO_2 samples. However, the VO_2 / Au sample has large nucleation zones on the surface with a smoother structure between these peaks. Examining this region between the nucleation zones, we find the surface structure is like the other samples suggesting that the annealing of the VO_2 post growth results in the large nucleation zones from surface rearrangement. Additionally, the roughness of the 5μm x 5μm scan of the VO_2 and Au / VO_2 samples display similar RMS roughness at ~15 nm roughness while the 5μm x 5μm VO_2 / Au sample displays a lower RMS roughness of ~12 nm and scanning between the large nucleation regions we find that the RMS roughness of a 2.5μm x 2.5μm is ~7nm nm, again suggesting the annealing of the VO_2 during the Au growth has some degree of surface rearrangement resulting in large nucleation zones and a smoother surface between the zones. We determine that the method where VO_2 is grown first manifests large nucleation zones due to annealing during the Au growth whereas the opposite method does not manifest such zones and is consistent with the sample without Au.

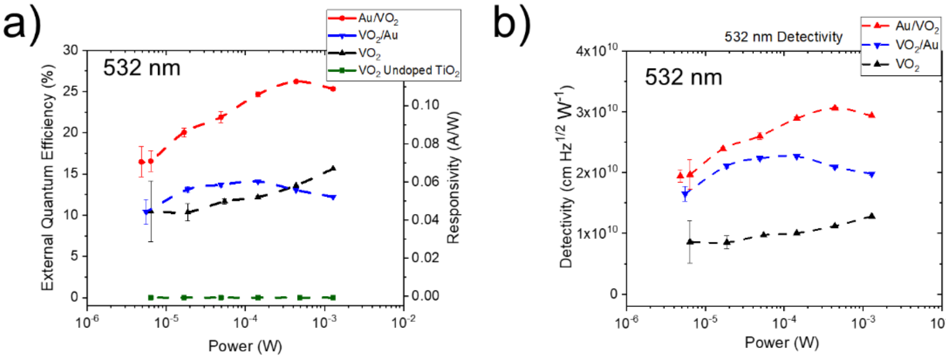

Figure C.3: The 532 nm figures of merit for Au/VO$_2$, VO$_2$/Au, and VO$_2$ a) is the external quantum efficiency (EQE) and responsivity with b) is the detectivity.

We examined the figures of merit: external quantum efficiency (EQE), responsivity, and detectivity under 532 nm illumination, photocurrent production is only accessible with cation doping of the TiO$_2$:Nb. We observe the highest figures of merit in the Au/VO$_2$ finding the EQE to be 27%, responsivity of 0.11 A/W, and detectivity of ~3 x 10^{10} $\frac{cm\sqrt{Hz}}{W}$ as demonstrated in Fig. C.3a-b). For comparison, we examined a VO$_2$ film grown on an undoped TiO$_2$ substrate which exhibits no photocurrent production and an EQE of effectively 0% which demonstrates the 3.0 eV band gap prevents carriers from exciting to the conduction band at 532 nm.

Finally, I present the measurement comparison between the photocurrent and photovoltage measurement methods for the 15 nm VO$_2$ samples at 1.4μW under 254 nm illumination in Table C.1.

Table C.1: Photocurrent and Photovoltage Measurement Method Comparison

	Photocurrent (A)	Responsivity (A/W)	EQE (%)
VO_2			
Photovoltage:	$6.0 \cdot 10^{-7}$	0.44	220
Photocurrent:	$5.8 \cdot 10^{-7}$	0.42	210
Au/VO_2			
Photovoltage:	$6.5 \cdot 10^{-7}$	0.48	240
Photocurrent:	$6.2 \cdot 10^{-7}$	0.45	220
VO_2/Au			
Photovoltage:	$2.8 \cdot 10^{-7}$	0.20	100
Photocurrent:	$3.2 \cdot 10^{-7}$	0.23	110

Appendix D

Resistive Properties of VO_2 Samples

We sought to determine the resistive properties of the VO_2 thin films as discussed in Section 5.3.2. In table D.1, the typical resistive properties via the van der Pauw method are shown for the 30 nm thick VO_2 samples grown on each substrate characterized in this study.

Table D.1: Vanadium Dioxide Resistive Properties

Substrate	c-Al_2O_3(0001)	TiO_2(001)	TiO_2:Nb(001)
Typical Film Dimensions	5mm x 3mm	5mm x 3mm	5mm x 3mm
Sheet Resistance (Ω/□)	10^7	10^6	10^4
Resistivity (Ω·m)	10^{-1}	10^{-2}	10^{-4}

BIBLIOGRAPHY

1. United States Government Accountability Office, *Neutron Detectors Alternatives to Using Helium-3 Report to Congressional Requesters* (2011).
2. S. J. Young, L. W. Ji, R. W. Chuang, S. J. Chang, and X. L. Du, "Characterization of ZnO metal–semiconductor–metal ultraviolet photodiodes with palladium contact electrodes," Semicond. Sci. Technol. 21(10), 1507–1511 (2006).
3. E. Monroy, F. Omnès, and F. Calle, "Wide-bandgap semiconductor ultraviolet photodetectors," Semicond. Sci. Technol 18, 33–51 (2003).
4. E. Monroy, F. Calle, J. L. Pau, E. Mu, F. Omn, B. Beaumont, and P. Gibart, "AlGaN-based UV photodetectors," J. Cryst. Growth 230, 537–543 (2001).
5. A. A. Ahmed, M. Devarajan, and N. Afzal, "Fabrication and characterization of high performance MSM UV photodetector based on NiO film," Sensors Actuators A Phys. 262, 78–86 (2017).
6. M. Razeghi and A. Rogalski, "Semiconductor ultraviolet detectors," J. Appl. Phys. 79(10), 7433–7473 (1996).
7. G. Parish, S. Keller, P. Kozodoy, J. P. Ibbetson, H. Marchand, P. T. Fini, S. B. Fleischer, S. P. Denbaars, U. K. Mishra, and E. J. Tarsa, "High-performance (Al,Ga)N-based solar-blind ultraviolet p-i-n detectors on laterally epitaxially overgrown GaN," Appl. Phys. Lett 75, 247 (1999).
8. D. Walker, V. Kumar, K. Mi, P. Sandvik, P. Kung, X. H. Zhang, and M. Razeghi, "Solar-blind AlGaN photodiodes with very low cutoff wavelength," Appl. Phys. Lett. 76(4), 403–405 (2000).
9. M. Razeghi, "Short-wavelength solar-blind detectors-status, prospects, and markets," Proc. IEEE 90(6), 1006–1014 (2002).
10. X. C. Guo, N. H. Hao, D. Y. Guo, Z. P. Wu, Y. H. An, X. L. Chu, L. H. Li, P. G. Li, M. Lei, and W. H. Tang, "β-Ga_2O_3/p-Si heterojunction solar-blind ultraviolet photodetector with enhanced photoelectric responsivity," J. Alloys Compd. 660, 136–140 (2016).
11. T. Oshima, T. Okuno, N. Arai, al -, X. Zi-Li, Z. Rong, and X. Chang-Tai, "Vertical Solar-Blind Deep-Ultraviolet Schottky Photodetectors Based on β-

Ga_2O_3 Substrates," Appl. Phys. Express 1, 011202 (2008).

12. M. A. Khan, J. N. Kuznia, D. T. Olson, J. M. Van Hove, M. Blasingame, and L. F. Reitz, "High-responsivity photoconductive ultraviolet sensors based on insulating single-crystal GaN epilayers," Appl. Phys. Lett. 60(23), 2917–2919 (1992).

13. J. Xing, E.-J. Guo, W. Huiyun, and F. Yang, "Highly sensitive fast-response UV photodetectors based on epitaxial TiO_2 films," J. Phys. D Appl. Phys. To 44, 375104 (2011).

14. X. Zhou, Q. Zhang, L. Gan, X. Li, H. Li, Y. Zhang, D. Golberg, and T. Zhai, "High-Performance Solar-Blind Deep Ultraviolet Photodetector Based on Individual Single-Crystalline Zn $_2$ GeO $_4$ Nanowire," Adv. Funct. Mater. 26(5), 704–712 (2016).

15. W. Yang, R. D. Vispute, S. Choopun, R. P. Sharma, T. Venkatesan, and H. Shen, "Ultraviolet photoconductive detector based on epitaxial $Mg_{0.34}Zn_{0.66}O$ thin films," Appl. Phys. Lett. 78(18), 2787–2789 (2001).

16. X. Du, Z. Mei, Z. Liu, Y. Guo, T. Zhang, Y. Hou, Z. Zhang, Q. Xue, and A. Y. Kuznetsov, "Controlled Growth of High-Quality ZnO-Based Films and Fabrication of Visible-Blind and Solar-Blind Ultra-Violet Detectors," Adv. Mater. 21(45), 4625–4630 (2009).

17. S. Alkis, B. Tekcan, A. Nayfeh, and A. K. Okyay, "UV/vis range photodetectors based on thin film ALD grown ZnO/Si heterojunction diodes," J. Opt. 15(10), 105002 (2013).

18. L. Sang, M. Liao, M. Sumiya, L. Sang, M. Liao, and M. Sumiya, "A Comprehensive Review of Semiconductor Ultraviolet Photodetectors: From Thin Film to One-Dimensional Nanostructures," Sensors 13(8), 10482–10518 (2013).

19. W. Yang, F. Zhang, Z. Liu, and Z. Wu, "Effects of annealing on the performance of 4H-SiC metal–semiconductor–metal ultraviolet photodetectors," Mater. Sci. Semicond. Process. 11(2), 59–62 (2008).

20. J. A. Creeden, S. E. Madaras, D. B. Beringer, M. R. Beebe, I. Novikova, and R. A. Lukaszew, "Structural and Photoelectric Properties of Epitaxially Grown Vanadium Dioxide Thin Films on c-Plane Sapphire and Titanium Dioxide," Sci. Rep. 9(1), 9362 (2019).

21. J. A. Creeden, S. E. Madaras, D. B. Beringer, I. Novikova, and R. A. Lukaszew, "Growth and Characterization of Vanadium Dioxide / Niobium Doped Titanium Dioxide Heterostructures for Ultraviolet Detection," Adv.

Opt. Mater. 1901142 (2019).

22. D. M. Mattox, *Handbook of Physical Vapor Deposition (PVD) Processing* (William Andrew, 2010).

23. M. Ohring, *Materials Science of Thin Films : Deposition and Structure* (Academic Press, 2002).

24. D. L. (Donald L. Smith, *Thin-Film Deposition : Principles and Practice*, 1st ed. (McGraw-Hill, 1995).

25. A. Anders, "A structure zone diagram including plasma-based deposition and ion etching," Thin Solid Films 518(15), 4087–4090 (2010).

26. N. W. Ashcroft and N. D. Mermin, *Solid State Physics* (Holt, Rinehart and Winston, 1976).

27. F. Bloch, "Bemerkung zur Elektronentheorie des Ferromagnetismus und der elektrischen Leitfahigkeit," Zeitschrift fur Phys. 57(7–8), 545–555 (1929).

28. C. Kittel, *Introduction to Solid State Physics* (Wiley, 2005).

29. A. H. Wilson, "The Theory of Electronic Semi-Conductors," Proc. R. Soc. Lond. A 133, (1931).

30. G. Busch, "Early history of the physics and chemistry of semiconductors-from doubts to fact in a hundred years," Eur. J. Phys. 10(4), 254–264 (1989).

31. G. Kotliar and D. Vollhardt, "Strongly Correlated Materials: Insights From Dynamical Mean-Field Theory," Phys. Today 57(3), 53–59 (2004).

32. M. Imada, A. Fujimori, and Y. Tokura, "Metal-insulator transitions," Rev. Mod. Phys. 70(4), 1039 (1998).

33. N. Mott, *Metal-Insulator Transitions* (CRC Press, 1990).

34. N. F. Mott and R. Peierls, "Discussion of the Paper by de Boer and Verwey," Proc. Phys. Soc 49(72), (1937).

35. N. F. Mott, "The Basis of the Electron Theory of Metals, with Special Reference to the Transition Metals," Proc. Phys. Soc. Sect. A 62(7), 416–422 (1949).

36. J. H. de Boer and E. J. W. Verwey, "Semi-conductors with partially and with completely filled 3d -lattice bands," Proc. Phys. Soc. 49(4S), 59–71 (1937).

37. N. F. Mott and L. Friedman, "Metal-insulator transitions in VO_2 , Ti_2O_3

and Ti $_{2-x}$V$_x$O$_3$," Philos. Mag. 30(2), 389–402 (1974).

38. M. M. Qazilbash, K. S. Burch, D. Whisler, D. Shrekenhamer, B. G. Chae, H. T. Kim, and D. N. Basov, "Correlated metallic state of vanadium dioxide," Phys. Rev. B 74, 205118 (2006).

39. M. Taha, S. Walia, T. Ahmed, D. Headland, W. Withayachumnankul, S. Sriram, and M. Bhaskaran, "Insulator-metal transition in substrate-independent VO_2 thin film for phase-change devices.," Sci. Rep. 7(1), 17899 (2017).

40. E. E. Chain, "Optical properties of vanadium dioxide and vanadium pentoxide thin films," Appl. Opt. 30(19), 2782 (1991).

41. L. Wang, I. Novikova, J. M. Klopf, S. Madaras, G. P. Williams, E. Madaras, J. Lu, S. A. Wolf, and R. A. Lukaszew, "Distinct Length Scales in the VO_2 Metal-Insulator Transition Revealed by Bi-chromatic Optical Probing," Adv. Opt. Mater. 2(1), 30–33 (2014).

42. D. J. Hilton, R. P. Prasankumar, S. Fourmaux, A. Cavalleri, D. Brassard, M. A. El Khakani, J. C. Kieffer, A. J. Taylor, and R. D. Averitt, "Enhanced Photosusceptibility near T_c for the Light-Induced Insulator-to-Metal Phase Transition in Vanadium Dioxide," Phys. Rev. Lett. 99(22), 226401 (2007).

43. S. Wall, D. Wegkamp, L. Foglia, K. Appavoo, J. Nag, R. F. Haglund, J. Stähler, and M. Wolf, "Ultrafast changes in lattice symmetry probed by coherent phonons," Nat. Commun. 3(1), 721 (2012).

44. H.-T. Kim, Y. W. Lee, B.-J. Kim, B.-G. Chae, S. J. Yun, K.-Y. Kang, K.-J. Han, K.-J. Yee, and Y.-S. Lim, "Monoclinic and Correlated Metal Phase in VO_2 as Evidence of the Mott Transition: Coherent Phonon Analysis," Phys. Rev. Lett. 97(26), 266401 (2006).

45. T. L. Cocker, L. V. Titova, S. Fourmaux, G. Holloway, H.-C. Bandulet, D. Brassard, J.-C. Kieffer, M. A. El Khakani, and F. A. Hegmann, "Phase diagram of the ultrafast photoinduced insulator-metal transition in vanadium dioxide," Phys. Rev. B 85(15), 155120 (2012).

46. F. J. Morin, "Oxides which show a metal-to-insulator transition at the neel temperature," Phys. Rev. Lett. 3(1), 34–36 (1959).

47. V. Eyert, "The metal-insulator transitions of VO2 : A band theoretical approach," Ann. Phys. 9(11), 1–61 (2002).

48. M. M. Qazilbash, M. Brehm, B.-G. Chae, P.-C. Ho, G. O. Andreev, B.-J.

Kim, S. J. Yun, A. V. Balatsky, M. B. Maple, F. Keilmann, H.-T. Kim, and D. N. Basov, "Mott Transition in VO2 Revealed by Infrared Spectroscopy and Nano-Imaging," Science (80-.). 318(5857), 1750–1753 (2007).

49. J. B. Goodenough, "The two components of the crystallographic transition in VO2," J. Solid State Chem. 3(4), 490–500 (1971).

50. A. Zylbersztejn and N. F. Mott, "Metal-insulator transition in vanadium dioxide," Phys. Rev. B 11(11), 4383–4395 (1975).

51. T. M. Rice, H. Launois, and J. P. Pouget, "Comment on “VO2: Peierls or Mott-Hubbard? A View from Band Theory,”" Phys. Rev. Lett. 73(22), 3042–3042 (1994).

52. S. Shin, S. Suga, M. Taniguchi, M. Fujisawa, H. Kanzaki, A. Fujimori, H. Daimon, Y. Ueda, K. Kosuge, and S. Kachi, "Vacuum-ultraviolet reflectance and photoemission study of the metal-insulator phase transitions in VO_2, V_6O_{13}, and V_2O_3," Phys. Rev. B 41(8), 4993 (1990).

53. J. P. Pouget, H. Launois, J. P. D’Haenens, P. Merenda, and T. M. Rice, "Electron Localization Induced by Uniaxial Stress in Pure VO2," Phys. Rev. Lett. 35(13), 873–875 (1975).

54. M. Marezio, D. B. McWhan, J. P. Remeika, and P. D. Dernier, "Structural aspects of the metal-insulator transitions in Cr-doped VO2," Phys. Rev. B 5(7), 2541 (1972).

55. J. P. Pouget, H. Launois, T. M. Rice, P. Dernier, A. Gossard, G. Villeneuve, and P. Hagenmuller, "Dimerization of a linear Heisenberg chain in the insulating phases of V1-xCrxO2," Phys. Rev. B 10(5), 1801 (1974).

56. C. Leroux, G. Nihoul, and G. Van Tendeloo, "From VO_2(B) to VO_2(R): Theoretical structures of VO_2 polymorphs and in situ electron microscopy," Phys. Rev. B 57(9), 5111–5121 (1998).

57. E. Morosan, D. Natelson, A. Nevidomskyy, and Q. Si, "Strongly Correlated Materials," Adv. Mater. 24(36), 4896–4923 (2012).

58. R. M. Wentzcovitch, W. W. Schulz, and P. B. Allen, "VO_2: Peierls or Mott-Hubbard? A View from Band Theory," Phys. Rev. Lett. 72(21), 3389 (1994).

59. J. M. Longo and P. Kierkegaard, "A Refinement of the Structure of VO_2.," Acta Chem. Scand. 24, 420–426 (1970).

60. G. Andersson, "Studies on Vanadium Oxides. II. The Crystal Structure of Vanadium Dioxide.," Acta Chem. Scand. 10, 623–628 (1956).

61. Y. Muraoka and Z. Hiroi, "Metal–insulator transition of VO_2 thin films grown on TiO_2 (001) and (110) substrates," Appl. Phys. Lett. 80(4), 583–585 (2002).

62. B. G. Chae, H. T. Kim, D. H. Youn, and K. Y. Kang, "Abrupt metal-insulator transition observed in VO2 thin films induced by a switching voltage pulse," Phys. B Condens. Matter 369(14), 76–80 (2005).

63. Y. Y. Luo, L. Q. Zhu, Y. X. Zhang, S. S. Pan, S. C. Xu, M. Liu, and G. H. Li, "Optimization of microstructure and optical properties of VO $_2$ thin film prepared by reactive sputtering," J. Appl. Phys. 113(18), 183520 (2013).

64. E. Kusano, J. A. Theil, and J. A. Thornton, "Deposition of vanadium oxide films by direct-current magnetron reactive sputtering," J. Vac. Sci. Technol. A Vacuum, Surfaces, Film. 6(3), 1663–1667 (1988).

65. L. A. Ladd and W. Paul, "Optical and transport properties of high quality crystals of V2O4 near the metallic transition temperature," Solid State Commun. 7(4), 425–428 (1969).

66. H. W. Verleur, A. S. Barker, and C. N. Berglund, "Optical Properties of VO_2 between 0.25 and 5 eV," Phys. Rev. 172(3), 788–798 (1968).

67. M. M. Qazilbash, A. A. Schafgans, K. S. Burch, S. J. Yun, B. G. Chae, B. J. Kim, H. T. Kim, and D. N. Basov, "Electrodynamics of the vanadium oxides VO2 and V_2O_3," Phys. Rev. B - Condens. Matter Mater. Phys. 77(11), 115121 (2008).

68. K. Okazaki, H. Wadati, A. Fujimori, M. Onoda, Y. Muraoka, and Z. Hiroi, "Photoemission study of the metal-insulator transition in VO2/TiO2(001): Evidence for strong electron-electron and electron-phonon interaction," Phys. Rev. B - Condens. Matter Mater. Phys. 69(16), 165104 (2004).

69. S. Shin, S. Suga, M. Taniguchi, M. Fujisawa, H. Kanzaki, A. Fujimori, H. Daimon, Y. Ueda, K. Kosuge, and S. Kachi, "Vacuum-ultraviolet reflectance and photoemission study of the metal-insulator phase transitions in VO_2, V_6O_{13}, and V_2O_3," Phys. Rev. B 41(8), 4993–5009 (1990).

70. E. Pelizzetti and N. Serpone, *Homogeneous and Heterogeneous Photocatalysis*, 1st ed. (D. Reidel Publishing Company, 1986).

71. K. E. Karakitsou and X. E. Verykios, "Effects of Altervalent Cation Doping of TiO2 on Its Performance as a Photocatalyst for Water," J. Phys. Chem 97(6), 1184–1189 (1993).

72. E. P. Meagher and G. A. Lager, "Polyhedral Thermal Expansion in the TiO_2 Polymorphs: Refinement of the Crystal Structures of the Rutile and Brookite at High Temperature," Can. Mineral. 17, 77–85 (1979).

73. N. Yamada, T. Hitosugi, J. Kasai, N. L. H. Hoang, S. Nakao, Y. Hirose, T. Shimada, and T. Hasegawa, "Transparent conducting Nb-doped anatase TiO_2(TNO) thin films sputtered from various oxide targets," Thin Solid Films 518(11), 3101–3104 (2010).

74. T. Mitsuhashi and O. J. Kleppa, "Transformation Enthalpies of the TiO2 Polymorphs," J. Am. Ceram. Soc. 62(7–8), 356–357 (1979).

75. A. Navrotsky and O. J. Kleppa, "Enthalpy of the Anatase-Rutile Transformation," J. Am. Ceram. Soc. 50(11), 626 (1967).

76. D. A. H. Hanaor and C. C. Sorrell, "Review of the anatase to rutile phase transformation," J. Mater. Sci. 46(4), 855–874 (2011).

77. S. J. Smith, R. Stevens, S. Liu, G. Li, A. Navrotsky, J. Boerio-Goates, and B. F. Woodfield, "Heat capacities and thermodynamic functions of TiO2 anatase and rutile: Analysis of phase stability," Am. Mineral. 94(2–3), 236–243 (2009).

78. J. Muscat, V. Swamy, and N. M. Harrison, "First-principles calculations of the phase stability of TiO2," Phys. Rev. B - Condens. Matter Mater. Phys. 65(22), 224112 (2002).

79. H. Zhang and J. F. Banfield, "Thermodynamic analysis of phase stability of nanocrystalline titania," J. Mater. Chem. 8(9), 2073–2076 (1998).

80. Y. Muraoka, T. Yamauchi, Y. Ueda, and Z. Hiroi, "Efficient photocarrier injection in a transition metal oxide heterostructure," J. Phys. Condens. Matter 14(49), L757–L763 (2002).

81. N. Serpone, "Is the band gap of pristine TiO2 narrowed by anion- and cation-doping of titanium dioxide in second-generation photocatalysts?," J. Phys. Chem. B 110(48), 24287–24293 (2006).

82. Z. Zhang, C.-C. Wang, R. Zakaria, and J. Y. Ying, "Role of Particle Size in Nanocrystalline TiO2-Based Photocatalysts," J. Phys. Chem. B 102(52), 10871–10878 (1998).

83. B. Sun, A. V. Vorontsov, and P. G. Smirniotis, "Role of platinum deposited on TiO2 in phenol photocatalytic oxidation," Langmuir 19(8), 3151–3156 (2003).

84. K. Nagaveni, M. S. Hegde, N. Ravishankar, G. N. Subbanna, and G.

Madras, "Synthesis and structure of nanocrystalline TiO2 with lower band gap showing high photocatalytic activity," Langmuir 20(7), 2900–2907 (2004).

85. H. Y. Hwang, Y. Iwasa, M. Kawasaki, B. Keimer, N. Nagaosa, and Y. Tokura, "Emergent phenomena at oxide interfaces," Nat. Mater. 11, 103–113 (2012).

86. J. E. Mahan, "Physical Vapor Deposition of Thin Films," Phys. Vap. Depos. Thin Film. by John E. Mahan, pp. 336. ISBN 0-471-33001-9. Wiley-VCH , January 2000. (2000).

87. F. F. Chen, *Introduction to Plasma Physics and Controlled Fusion* (Springer International Publishing, 2016).

88. Y. B. Kang, "Critical evaluation and thermodynamic optimization of the VO-$VO_{2.5}$ system," J. Eur. Ceram. Soc. 32(12), 3187–3198 (2012).

89. Y. Yang, H. Mao, and M. Selleby, "Thermodynamic assessment of the V-O system," Calphad 51, 144–160 (2015).

90. G. Rampelberg, B. De Schutter, W. Devulder, K. Martens, I. Radu, and C. Detavernier, "In situ X-ray diffraction study of the controlled oxidation and reduction in the V-O system for the synthesis of VO 2 and V 2 O 3 thin films," J. Mater. Chem. C 3, 11357 (2015).

91. N. Jalili and K. Laxminarayana, "A review of atomic force microscopy imaging systems: Application to molecular metrology and biological sciences," Mechatronics 14(8), 907–945 (2004).

92. I. Horcas, R. Fernández, J. M. Gómez-Rodríguez, J. Colchero, J. Gómez-Herrero, and A. M. Baro, "WSXM: A software for scanning probe microscopy and a tool for nanotechnology," Rev. Sci. Instrum. 78(1), 013705 (2007).

93. M. Birkholz, *Thin Film Analysis by X-Ray Scattering* (2006).

94. B. D. Cullity and S. R. Stock, *Elements of X-Ray Diffraction, Third Edition*, 3rd ed. (Prentice-Hall, 2001).

95. J. I. Langford and A. J. C. Wilson, "Scherrer after sixty years: A survey and some new results in the determination of crystallite size," J. Appl. Crystallogr. 11(2), 102–113 (1978).

96. H. Kiessig, "Interferenz von Röntgenstrahlen an dünnen Schichten," Ann. Phys. (1931).

97. A. Ichimiya and P. I. Cohen, *Reflection High-Energy Electron Diffraction* (Cambridge University Press, 2004).

98. J. E. Mahan, K. M. Geib, G. Y. Robinson, and R. G. Long, "A review of the geometrical fundamentals of reflection high-energy electron diffraction with application to silicon surfaces," J. Vac. Sci. Technol. A Vacuum, Surfaces, Film. 8(5), 3692–3700 (1990).

99. K. Wang and A. R. Smith, "Efficient kinematical simulation of reflection high-energy electron diffraction streak patterns for crystal surfaces," Comput. Phys. Commun. 182(10), 2208–2212 (2011).

100. L. J. Van der Pauw, "A Method of Measuring the Resistivity and Hall Coefficient of Lamellae of Arbitrary Shape," Phillips Tech. Rev. 20, 220–224 (1958).

101. P. C. Datskos and N. V Lavrik, "Detectors-Figures of Merit," Encycl. Opt. Photonic Eng. 451–459 (2015).

102. J. M. Wu and W. E. Chang, "Ultrahigh Responsivity and External Quantum Efficiency of an Ultraviolet-Light Photodetector Based on a Single VO_2 Microwire," ACS Appl. Mater. Interfaces 6(16), 14286–14292 (2014).

103. J. D. Yao, Z. Q. Zheng, J. M. Shao, and G. W. Yang, "Stable, highly-responsive and broadband photodetection based on large-area multilayered WS 2 films grown by pulsed-laser deposition," Nanoscale 7(36), 14974–14981 (2015).

104. P. Hu, L. Wang, M. Yoon, J. Zhang, W. Feng, X. Wang, Z. Wen, J. C. Idrobo, Y. Miyamoto, D. B. Geohegan, and K. Xiao, "Highly Responsive Ultrathin GaS Nanosheet Photodetectors on Rigid and Flexible Substrates," Nano Lett. 13, 1649–1654 (2013).

105. P. Hu, Z. Wen, L. Wang, P. Tan, and K. Xiao, "Synthesis of Few-Layer GaSe Nanosheets for High Performance Photodetectors," ACS Nano 6(7), 5988–5994 (2012).

106. P. Merken and R. Vandersmissen, *Dark Current and Influence of Target Emissivity Low-Noise InGaAs Camera Cougar-640* (2016).

107. H. Huang, Y. Xie, W. Yang, F. Zhang, J. Cai, and Z. Wu, "Low-Dark-Current TiO_2 MSM UV Photodetectors With Pt Schottky Contacts," IEEE Electron Device Lett. 32(4), 530–532 (2011).

108. C.-Y. Tsay and W.-T. Hsu, "Comparative Studies on Ultraviolet-Light-

Derived Photoresponse Properties of ZnO, AZO, and GZO Transparent Semiconductor Thin Films.," Materials (Basel). 10(12), 1379 (2017).

109. R. Droopad, R. L. Williams, and S. D. Parker, "RHEED intensity oscillations observed during the MBE growth of InSb (100)," Semicond. Sci. Technol. 4(2), 111–113 (1989).

110. E. Radue, L. Wang, S. Kittiwatanakul, J. Lu, S. A. Wolf, E. Rossi, R. A. Lukaszew, and I. Novikova, "Substrate-induced microstructure effects on the dynamics of the photo-induced metal–insulator transition in VO $_2$ thin films," J. Opt. 17(2), 025503 (2015).

111. J. Robertson, "Band offsets of wide-band-gap oxides and implications for future electronic devices," J. Vac. Sci. Technol. B Microelectron. Nanom. Struct. 18(3), 1785 (2000).

112. M. M. Qazilbash, Z. Q. Li, V. Podzorov, M. Brehm, F. Keilmann, B. G. Chae, H. T. Kim, and D. N. Basov, "Electrostatic modification of infrared response in gated structures based on VO_2," Appl. Phys. Lett. 92(24), 241906 (2008).

113. L. Wang, E. Radue, S. Kittiwatanakul, C. Clavero, J. Lu, S. A. Wolf, I. Novikova, and R. A. Lukaszew, "Surface plasmon polaritons in VO_2 thin films for tunable low-loss plasmonic applications," Opt. Lett. 37(20), 4335 (2012).

114. S. Kittiwatanakul, J. Laverock, D. Newby, K. E. Smith, S. A. Wolf, and J. Lu, "Transport behavior and electronic structure of phase pure VO_2 thin films grown on *c* -plane sapphire under different O_2 partial pressure," J. Appl. Phys. 114(5), 053703 (2013).

115. A. Cavalleri, C. Tóth, C. W. Siders, J. A. Squier, F. Ráksi, P. Forget, and J. C. Kieffer, "Femtosecond Structural Dynamics in VO_2 during an Ultrafast Solid-Solid Phase Transition," Phys. Rev. Lett. 87(23), 237401 (2001).

116. W.-P. Hsieh, M. Trigo, D. A. Reis, G. Andrea Artioli, L. Malavasi, and W. L. Mao, "Evidence for photo-induced monoclinic metallic VO $_2$ under high pressure," Appl. Phys. Lett. 104(2), 021917 (2014).

117. U. Penner, H. Rücker, and I. N. Yassievich, "Theory of interface roughness scattering in quantum wells," Semicond. Sci. Technol. 13(7), 709–713 (1998).

118. M. Berginski, J. Hüpkes, M. Schulte, G. Schöpe, H. Stiebig, B. Rech, and M. Wuttig, "The effect of front ZnO:Al surface texture and optical

transparency on efficient light trapping in silicon thin-film solar cells," J. Appl. Phys. 101(7), 074903 (2007).

119. V. Kumar, N. Singh, R. M. Mehra, A. Kapoor, L. P. Purohit, and H. C. Swart, "Role of film thickness on the properties of ZnO thin films grown by sol-gel method," Thin Solid Films 539, 161–165 (2013).

120. G. Palasantzas, Y. Zhao, G. Wang, T. Lu, J. Barnas, and J. M. Th De Hosson, "Electrical conductivity and thin-film growth dynamics," Phys. Rev. B 61(16), (2000).

121. S. Ito, T. N. Murakami, P. Comte, P. Liska, C. Grätzel, M. K. Nazeeruddin, and M. Grätzel, "Fabrication of thin film dye sensitized solar cells with solar to electric power conversion efficiency over 10%," Thin Solid Films 516, 4613–4619 (2008).

122. H. Koch, "Sur une courbe continue sans tangente, obtenue par une construction géométrique élémentaire.," Arch. för Mat. Astron. och Fys. 1, 681–702 (1904).

123. B. B. Mandelbrot, *The Fractal Geometry of Nature: Updated and Augmented*, 2nd ed. (Freeman and Company, 1982).

124. M. F. Barnsley and H. Rising, *Fractals Everywhere* (Academic Press Professional, 1993).

125. M. Kardar, G. Parisi, and Y.-C. Zhang, "Dynamic Scaling of Growing Interfaces," Phys. Rev. Lett. 56(9), 889–892 (1986).

126. F. Family and T. Vicsek, *Dynamics of Fractal Surfaces* (WORLD SCIENTIFIC, 1991).

127. J. J. Ramasco, J. M. López, and M. A. Rodríguez, "Generic dynamic scaling in kinetic roughening," Phys. Rev. Lett. 84(10), 2199–2202 (2000).

128. F. Family and T. Vicsek, "Scaling of the active zone in the Eden process on percolation networks and the ballistic deposition model," J. Phys. A. Math. Gen. 18(2), L75–L85 (1985).

129. J. M. López, M. A. Rodríguez, and R. Cuerno, "Superroughening versus intrinsic anomalous scaling of surfaces," Phys. Rev. E - Stat. Nonlinear, Soft Matter Phys. 56(4), 3993–3998 (1997).

130. J. J. Ramasco, J. M. López, and M. A. Rodríguez, "Generic dynamic scaling in kinetic roughening," Phys. Rev. Lett. 84(10), 2199–2202 (2000).

131. I. Gupta and B. C. Mohanty, "Dynamics of surface evolution in

semiconductor thin films grown from a chemical bath," Sci. Rep. 6(1), 33136 (2016).

132. D. B. Beringer, W. M. Roach, C. Clavero, C. E. Reece, and R. A. Lukaszew, "Characterization of two different orientations of epitaxial niobium thin films grown on MgO(001) surfaces," J. Appl. Phys. 114(22), 223502 (2013).

133. A. L. Barabsi, H. E. Stanley, and Cambridge University Press., *Fractal Concepts in Surface Growth* (Cambridge University Press, 1995).

134. M. A. Auger, L. Vázquez, R. Cuerno, M. Castro, M. Jergel, and O. Sánchez, "Intrinsic anomalous surface roughening of TiN films deposited by reactive sputtering," Phys. Rev. B Condens. Matter 73, 045436 (2006).

135. J. A. Creeden, S. E. Madaras, D. B. Beringer, I. Novikova, and R. A. Lukaszew, "Intrinsic anomalous scaling of epitaxial vanadium dioxide thin films on titanium dioxide," AIP Adv. 9(9), 095045 (2019).

136. D. Nečas and P. Klapetek, "Gwyddion: an open-source software for SPM data analysis," Open Phys. 10(1), 181–188 (2012).

137. J. M. López, "Scaling Approach to Calculate Critical Exponents in Anomalous Surface Roughening," Phys. Rev. Lett. 83(22), 4594–4597 (1999).

138. A. L. Barabasi and H. E. Stanley, *Fractal Concepts in Surface Growth* (Cambridge University Press, 1995).

139. J. M. López, M. Castro, and R. Gallego, "Scaling of Local Slopes, Conservation Laws, and Anomalous Roughening in Surface Growth," Phys. Rev. Lett. 94(16), 166103 (2005).

140. A. S. Mata, S. C. Ferreira, I. R. B. Ribeiro, and S. O. Ferreira, "Anomalous scaling and super-roughness in the growth of CdTe polycrystalline films," Phys. Rev. B 78(11), 115305 (2008).

141. D. Kwon, Y. Shim, J. G. Amar, and A. D. Compaan, "Grain growth, anomalous scaling, and grain boundary grooving in polycrystalline CdTe thin films," Cit. J. Appl. Phys. 116, 64502 (2014).

142. A. E. Lita and J. E. Sanchez, "Effects of grain growth on dynamic surface scaling during the deposition of Al polycrystalline thin films," Phys. Rev. B 61(11), 7692–7699 (2000).

143. W. Park, G. Jo, W.-K. Hong, J. Yoon, M. Choe, S. Lee, Y. Ji, G. Kim, Y. H. Kahng, K. Lee, D. Wang, and T. Lee, "Enhancement in the

photodetection of ZnO nanowires by introducing surface-roughness-induced traps," Nanotechnology 22(20), 205204 (2011).

144. X. Liu, L. Gu, Q. Zhang, J. Wu, Y. Long, and Z. Fan, "All-printable band-edge modulated ZnO nanowire photodetectors with ultra-high detectivity," Nat. Commun. 5(1), 4007 (2014).

145. R. Korde and J. Geist, "Quantum efficiency stability of silicon photodiodes," Appl. Opt. 26(24), 5284 (1987).

146. C.-M. Chou, H.-T. Cho, V. K. S. Hsiao, K.-T. Yong, and W.-C. Law, "Quantum dot-doped porous silicon metal–semiconductor metal photodetector," Nanoscale Res. Lett. 7(1), 291 (2012).

147. L. Shi and S. Nihtianov, "Comparative Study of Silicon-Based Ultraviolet Photodetectors," IEEE Sens. J. 12(7), 2453–2459 (2012).

148. N. R. Mlyuka, G. A. Niklasson, and C. G. Granqvist, "Thermochromic multilayer films of VO_2 and TiO_2 with enhanced transmittance," Sol. Energy Mater. Sol. Cells 93, 1685–1687 (2009).

149. Raymond T. Tung, "The physics and chemistry of the Schottky barrier height," Appl. Phys. Rev. 1(011304), (2014).

150. E. H. Rhoderick, "Metal-semiconductor contacts," IEE Proc. I Solid State Electron Devices 129(1), 1 (1982).

151. C. Ko, Z. Yang, and S. Ramanathan, "Work Function of Vanadium Dioxide Thin Films Across the Metal-Insulator Transition and the Role of Surface Nonstoichiometry," ACS Appl. Mater. Interfaces 3, 3396–3401 (2011).

152. J. Hölzl and F. K. Schulte, "Work function of metals," in *Solid Surface Physics* (Springer Berlin Heidelberg, 1979), pp. 1–150.

153. H. B. Michaelson, "The work function of the elements and its periodicity," J. Appl. Phys. 48(11), 4729–4733 (1977).

154. G. A. Hope, A. J. Bard, and A. J. Bard', "Platinum/Titanium Dioxide (Rutile) Interface. Formation of Ohmic and Rectifying Junctions," J. Phys. Chem 87(11), 1979–1984 (1983).

155. M. E. A. Warwick and R. Binions, "Advances in thermochromic vanadium dioxide films," J. Mater. Chem. A 2(10), 3275–3292 (2014).

156. K. Ozawa, M. Emori, S. Yamamoto, R. Yukawa, S. Yamamoto, R. Hobara, K. Fujikawa, H. Sakama, and I. Matsuda, "Electron−Hole Recombination Time at TiO2 Single-Crystal Surfaces: Influence of Surface Band Bending,"

J. Phys. Chem. Lett. 5, 1953–1957 (2014).

157. K. C. Kao, *Dielectric Phenomena in Solids.* (Elsevier, 2004).

158. I. Olivares, L. Sánchez, J. Parra, R. Larrea, A. Griol, M. Menghini, P. Homm, L.-W. Jang, B. van Bilzen, J. W. Seo, J.-P. Locquet, and P. Sanchis, "Optical switching in hybrid VO $_2$ /Si waveguides thermally triggered by lateral microheaters," Opt. Express 26(10), 12387 (2018).

159. P. Markov, R. E. Marvel, H. J. Conley, K. J. Miller, R. F. Haglund, and S. M. Weiss, "Optically Monitored Electrical Switching in VO_2," ACS Photonics 2(8), 1175–1182 (2015).

160. A. L. Pergament, G. B. Stefanovich, and A. A. Velichko, "Oxide Electronics and Vanadium Dioxide Perspective: A Review," J. Sel. Top. Nano Electron. Comput. 1(1), 24–43 (2013).